ABSTRACT

Title of Dissertation: JOSEPHSON EFFECTS IN THE
IRON-BASED SUPERCONDUCTOR FETE$_{1-X}$SE$_X$

Samuel Deitemyer
Doctor of Philosophy, 2025

Dissertation Directed by: Professor Steve Rolston
Department of Physics

Professor Steven M. Anlage
Department of Physics

The iron-based superconductor FeTe$_{1-x}$Se$_x$ has emerged as a promising platform for combining superconductivity and topology in a single system, for the realization of topological quantum computing. Besides this, FeTe$_{1-x}$Se$_x$ hosts rich physical phenomena such as S$\pm$ superconductivity, Majorana bound states, and higher-order topological superconductivity, among others. Despite the interest in superconducting devices based on FeTe$_{1-x}$Se$_x$, there have been relatively few demonstrations of Josephson junctions in FeTe$_{1-x}$Se$_x$-based systems.

In this dissertation we measured Josephson effects in a FeTe$_{1-x}$Se$_x$-based device and found three signatures of unconventional Josephson junction behavior. This first signature was the existence of two distinct Josephson diffraction patterns under applied RF irradiation, which likely arises from flux flow and a phase slip line in FeTe$_{1-x}$Se$_x$. The second

signature was the emergence of sudden jumps in the DC current at which Shapiro steps arise, as a function of applied RF power. This was measured by mapping $\frac{dV}{dI}$ vs DC current and RF power. We provide two potential explanations for this phenomenon based on non-equilibrium superconductivity. The third signature is a minimum critical current at zero magnetic field when RF irradiation is present which resembles the π-Josephson junctions formed as a consequence of multiband superconductivity.

JOSEPHSON EFFECTS IN THE IRON-BASED SUPERCONDUCTOR FETE$_{1-X}$SE$_X$

by

Samuel Deitemyer

Dissertation submitted to the Faculty of the Graduate School of the
University of Maryland, College Park in partial fulfillment
of the requirements for the degree of
Doctor of Philosophy
2025

Advisory Committee:

Professor Steve Rolston, Chair
Professor Steven M. Anlage, Chair
Professor Alicia J. Kollár
Professor Kasra Sardashti
Professor Christopher Jarzynski, Dean's Representative

Dedication

To my wife Tienne, your love and support truly made this possible. I couldn't have done it without your constant encouragement and positivity.

Acknowledgements

I am deeply indebted to so many people who have helped me along the way out of the goodness of their hearts.

Firstly, I would like to thank Professor Rolston and Professor Anlage for their support and guidance throughout my graduation. I am sincerely grateful for all the effort and time they have spent helping me.

I would also like to thank Professor Anlage for sharing his expertise in superconductivity inside and outside the classroom. Your interest in the topics always came through and made learning fun.

I would like to thank Dr. Jimmy Williams for introducing me to research as an undergraduate student and for mentoring me as a graduate student. I learned so much from your mentorship, and for that, I am truly grateful.

I would like to extend my sincere thanks to Professor Kollár. You have been so generous with your time, and I truly can not express how appreciative I am of your support and kindness. On top of this, your coaching helped me land a job after graduation.

I would also like to thank Professor Cohen for his support and open-door policy. Unfortunately, I abused that policy, but it was incredibly valuable to me to have chats when I needed to.

I would like to thank Rodney Snyder for teaching me nearly everything I know about measurements. You have been an excellent mentor and friend to so many.

I would also like to thank Professor Gong for supporting me during my time in his group and for developing my written communication skills significantly.

There are so many others I want to thank, such as Doug Benson, John Abrahams, Tom Loughran, Mark Lecates, Jon Hummel, Karen Gaskell, and many others, for their technical support.

Additionally, I would like to thank all of my friends throughout my PhD who made the experience enjoyable.

Contents

List of Figures

xiv

Chapter 1

Introduction

1.1 Thesis Overview

In this thesis, I hope to give readers some familiarity with Josephson effects, highlight the development and state of research into the unconventional superconductor $\text{FeTe}_{1-x}\text{Se}_x$, and discuss some of the unusual results we found when performing cryogenic measurements of $\text{FeTe}_{1-x}\text{Se}_x$.

In Chapter 2, I will give a very brief overview of the basic phenomena of Superconductivity to prepare unfamiliar readers for discussions of $\text{FeTe}_{1-x}\text{Se}_x$ and Josephson junctions.

In Chapter 3, I will review the development and current state of research regarding the unconventional superconductor $\text{FeTe}_{1-x}\text{Se}_x$. This section may be of interest for those concerned with Majorana fermions in $\text{FeTe}_{1-x}\text{Se}_x$.

In Chapter 4, I will give a basic description of Josephson junctions and the related phenomena. Specifically, I will describe the Josephson equations, the AC Josephson effects, and the Fraunhofer pattern arising in the presence of a magnetic field.

In Chapter 5, I will discuss the main results of our study, the Josephson effects in a $\text{FeTe}_{1-x}\text{Se}_x$-Aluminum Josephson junction. I will discuss the presence of two Josephson

effects at different energy scales, discontinuous jumps in the AC Josephson diffraction pattern as RF power is increased, and the unusual magnetic diffraction pattern arising under RF irradiation.

In Chapter 6, I will conclude by summarizing our findings and discussing some of the future avenues for research on the unconventional superconductor $FeTe_{1-x}Se_x$.

The Appendix contains information I hope will be useful for readers interested in some specific details. This section covers the details of experimental methods, details of the deposition systems, various technical methods (tips and tricks), and finally, a data dump of the remaining data measured in the $FeTe_{1-x}Se_x$-Al Josephson junction, not already shown in Chapter 5.

Chapter 2

Superconductivity

2.1   Introduction to Superconducting Phenomena

In the following, I will give a brief introduction to the relevant physical phenomena of superconductors, which I learned from the excellent Introduction to Superconductivity by Michael Tinkham (Ref. [1]), as have many before me. This phenomenological description will serve as a basis for understanding superconducting phenomena in typical superconducting systems, as well as provide a basis for the unconventional superconductor $FeTe_{1-x}Se_x$, which we utilized in our study.

Superconductivity was first discovered by Kamerlingh Onnes in 1911 (Ref. [2]). This discovery was made possible by Onnes's successful liquefaction of helium in 1908, for which he would later receive the Nobel Prize. The successful liquification of helium opened the door for generations of low-temperature experiments. However, only 3 years later, in 1911, Onnes was researching the resistance of metals as a function of temperature, when he discovered that, in Mercury, below a temperature of $\sim$4.2 K, the electric resistance of Mercury became negligible. A schematic representation is shown in Fig. 2.1. This is a hallmark behavior of superconducting materials , and shortly thereafter led to demonstrations of persistent dissipationless current flow in a superconducting ring.
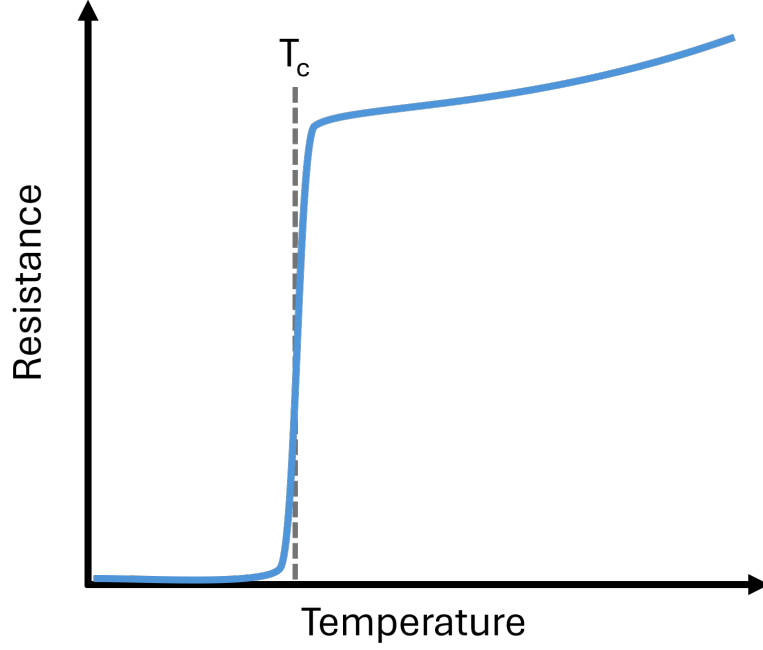
Figure 2.1: Resistance vs Temperature curve for a superconductor.

Another early phenomenon discovered in superconducting materials was the Meissner effect, discovered by Meissner and Ochsenfeld in 1933 (Ref. [3]). The Meissner effect is the demonstration of perfect diamagnetism by superconducting materials. Therefore, superconductors expel magnetic fields from their interior, as shown in Fig. 2.2. As noted by Tinkham (Ref. [1]), this would seem to be described by the perfect screening of the magnetic fields by dissipationless currents in the superconductor. However, according to Faraday's law, a perfect conductor would not require that the magnetic flux equal to zero, and would instead require that the time rate of change of the magnetic flux equal to zero, $\frac{dB}{dt} = 0$. This would trap the magnetic flux when the material entered the superconducting state. In 1935 the London brothers formulated two equations, $\frac{dJ}{dt} = \frac{ne^2}{m}E$ and $\nabla \times J = -\frac{ne^2}{m}B$ which result in the exponential screening and expulsion of magnetic fields over a length known as the London penetration depth $\lambda_L = \sqrt{\frac{m}{\mu_0 n_s e^2}}$.

An extension of this phenomenon, which flows naturally from the idea that super-conductors and magnetic fields are antagonistic to each other, is the idea of the critical field of a superconductor. This is a field large enough that the free energy cost to expel

4
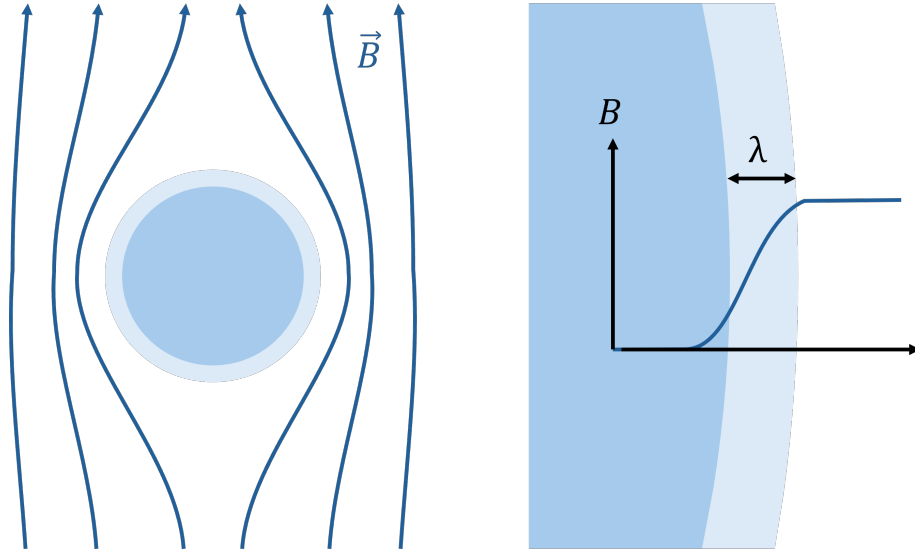
Figure 2.2: Diagram of the Meissner effect and the London penetration depth.

the field is greater than the free energy gained by forming the superconducting condensate, and therefore, superconductivity is destroyed. The critical field follows from a maximum value at zero temperature to zero field at the critical temperature of the superconductor, see Fig. 2.3. This relation is approximately described by $B_c = B_c(0)(1 - (T/Tc)^2)$.
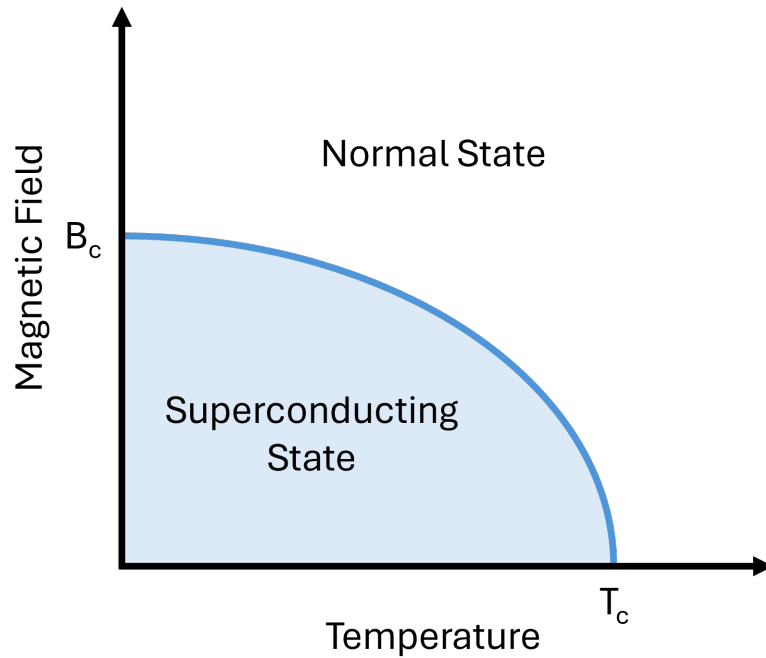
Figure 2.3: Diagram of relationship between critical temperature and critical field.

A related phenomenon in superconductors is the critical current density. This is the maximum current density that a superconductor can maintain before the superconductivity breaks down and transitions to the normal state, see Fig. 2.4. This breakdown of the superconductivity is a direct consequence of the critical field of the superconductor. As the current flows through a superconducting material, there will be a 'self-field' generated at the surface of the superconductor. If this surpasses the critical field of the superconductor, superconductivity is destroyed. For the simple case of a cylindrical superconducting wire, the relation $J_c = \frac{B_c}{\mu_0^2 \lambda}$ can be derived. Where J_c is the critical current density in the superconductor defined as the critical current per unit area. This relation is modified in samples with different geometries or when one of the length scales of the superconductor is smaller than the London penetration depth.
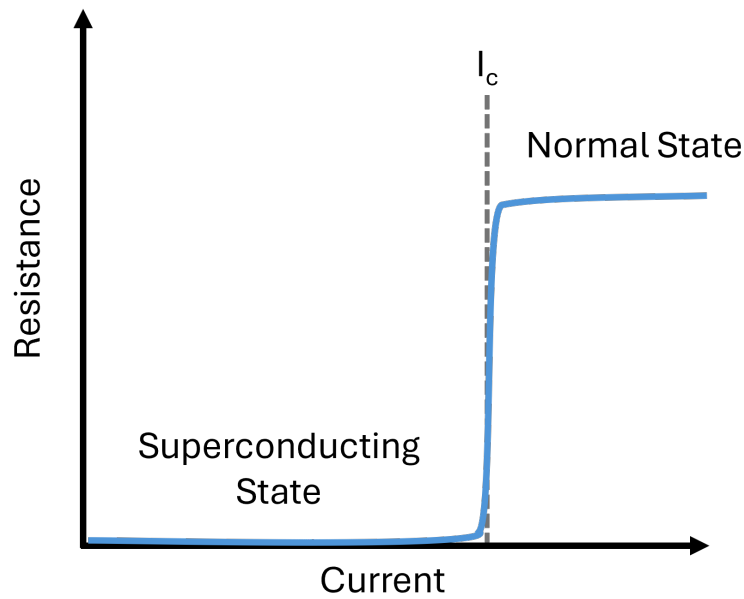
Figure 2.4: Diagram showing the critical current of a superconductor.

Lastly, I will briefly touch on the two fundamental theories that describe the behavior of superconductors. In 1957, Bardeen, Cooper, and Schrieffer established a microscopic theory to describe how, below the superconducting transition temperature, an attractive

electron-phonon interaction can cause pairs of electrons to condense into a bosonic quantum state. It would later be found that other interactions can give rise to superconductivity besides electron-phonon coupling, in so-called unconventional superconductors. This condensate consists of Cooper pairs and is separated from electronic states by the superconducting gap, 2Δ. Above this gap is an enhanced quasiparticle density of states, which was 'pushed' out of the superconducting gap, see Fig. 2.5. These peaks in the density of states can be used to identify the superconducting gap in a multitude of measurements. The BCS theory is particularly useful in its description of quasiparticles states. These Bogoliubov quasiparticles are unpaired superpositions of electron and hole states which exists outside of the superconducting gap. The existence of quasiparticles in superconductors has a number of significant impacts on devices, which we will discuss in Chapter 5.
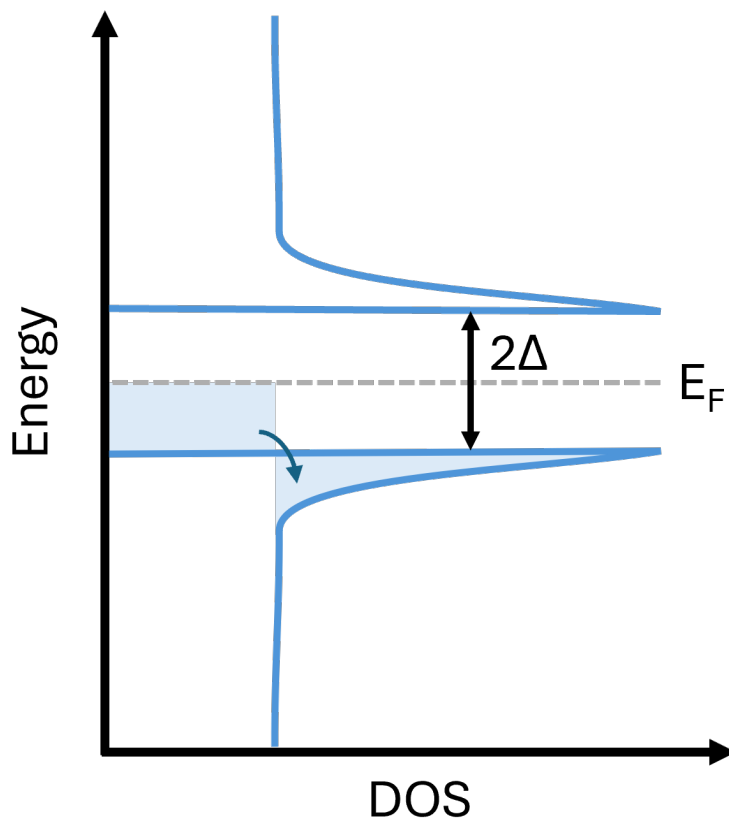
Figure 2.5: Diagram showing the electron density of states around the Fermi energy in a superconductor.

In order to describe the spatially-dependent phenomena in superconductors, the Ginzburg-Landau theory was developed, which defines a macroscopic order parameter based on the theory of second-order phase transitions. This order parameter turns out to be the macroscopic wavefunction of the superconductor and is defined as $\psi = \psi_0 e^{i\varphi}$. Where $\psi_0 = \sqrt{n_s}$, and n_s is the Cooper pair density. φ is the macroscopic phase of the superconductor which is crucial for understanding the dynamics of systems involving superconductors, as we will discuss in Chapter 4. It was later shown by Gor'kov that this theory could be derived from the BCS theory. The wavefunction of a macroscopic superconductor represented by a single phase leads to a number of interesting phenomena, such as flux quantization, Type II superconductors, superconducting vortices, and most importantly for this study, the Josephson effect. The Josephson effect occurs when two superconductors are separated by a non-superconducting layer that is sufficiently thin to allow for phase-coherent transport. In these devices, the phase difference between the two superconductors evolves according to the Josephson equations, which will be discussed in detail in Chapter 4.1.

Chapter 3

Review of FeTeSe

FeTe$_{1-x}$Se$_x$ is a class of materials derived from the parent compounds FeTe and FeSe, which demonstrates varying material properties based on the ratio of Te to Se. Under certain substitutional compositions, the class of FeTe$_{1-x}$Se$_x$ crystals demonstrate superconductivity and topological surface states, which has motivated significant research efforts aimed at the realization of Majorana fermions, since the discovery of superconductivity in FeTe$_{1-x}$Se$_x$ in 2008 (Ref. [4]). This came less than 1 year after the discovery of the first iron-based superconductor LaOFeAs (Ref. [5]), which shocked the scientific community because superconductivity and magnetism are considered antagonistic electronic phases.

3.1 Crystal Structure and Parent Compounds

FeTeSe and its parent compounds FeSe and FeTe are two-dimensional van der Waals (vdW) materials. This means that they are composed of atomically thin 2D layers of strongly covalently bonded atoms, which are weakly bonded by van der Waals forces to subsequent layers, as shown in Fig. 3.1. The prototypical example of a 2D material is graphene. In 2004, single-layer graphene was produced using scotch tape to separate an individual atomic layer from a bulk piece of graphite (Ref. [6]), which is known as graphene (Gr). This demonstration of a free-standing 2D material challenged previous assumptions based

on early works by Pierls in 1935 (Ref. [7]) and Landau in 1937 (Ref. [8]), which implied that divergent out-of-plane fluctuations would cause 2D materials to be unstable. Furthermore, in 1966 (Ref. [9]), works by Mermin-Wagner suggested that there could be no long-range order in one-dimensional or two-dimensional systems due to the enhancement of long-range fluctuations. It should be noted that Honenburg is sometimes credited alongside Mermin and Wagner for his earlier unpublished proof, and Berezinskii is sometimes credited as well for his independent proof. It is now widely accepted that Gr was realizable because it is not a perfect 2D system in the way the theoretical treatments assumed; the finite size of graphene monolayers and out-of-plane displacements (ripples) of the 2D structure relax the strict requirements of these theoretical works. The discovery of two-dimensional layers of graphene led to intense research over the past 20 years. Many interesting phenomena have now been demonstrated in 2D materials, and most significantly for this study, superconductivity.

Besides being a 2D material, the layers of FeTeSe form a tetragonal PbO-type structure at room temperature, as can be seen from the diagram of FeSe shown in Fig. 3.1, where a square structure can be seen along the c-axis. The central Fe atoms in vdW layer are bonded to Se atoms, alternating above or below the Fe plane. In FeTeSe crystals, a percentage of Se atoms will be substituted with Te atoms according to the overall composition. At lower temperatures, certain compositions of FeTeSe crystals undergo a structural transition to the orthorhombic phase, breaking the C4 rotational symmetry and resulting in C2 rotational symmetry. This occurs at $\sim$90 K in FeSe crystals and is related to an electron-nematic phase transition (Ref. [10]). In FeTe, which is not superconducting, there is no electronic-nematic transition. Instead, there is a phase transition to an antiferromagnetic phase below $\sim$70 K (Ref. [11]).
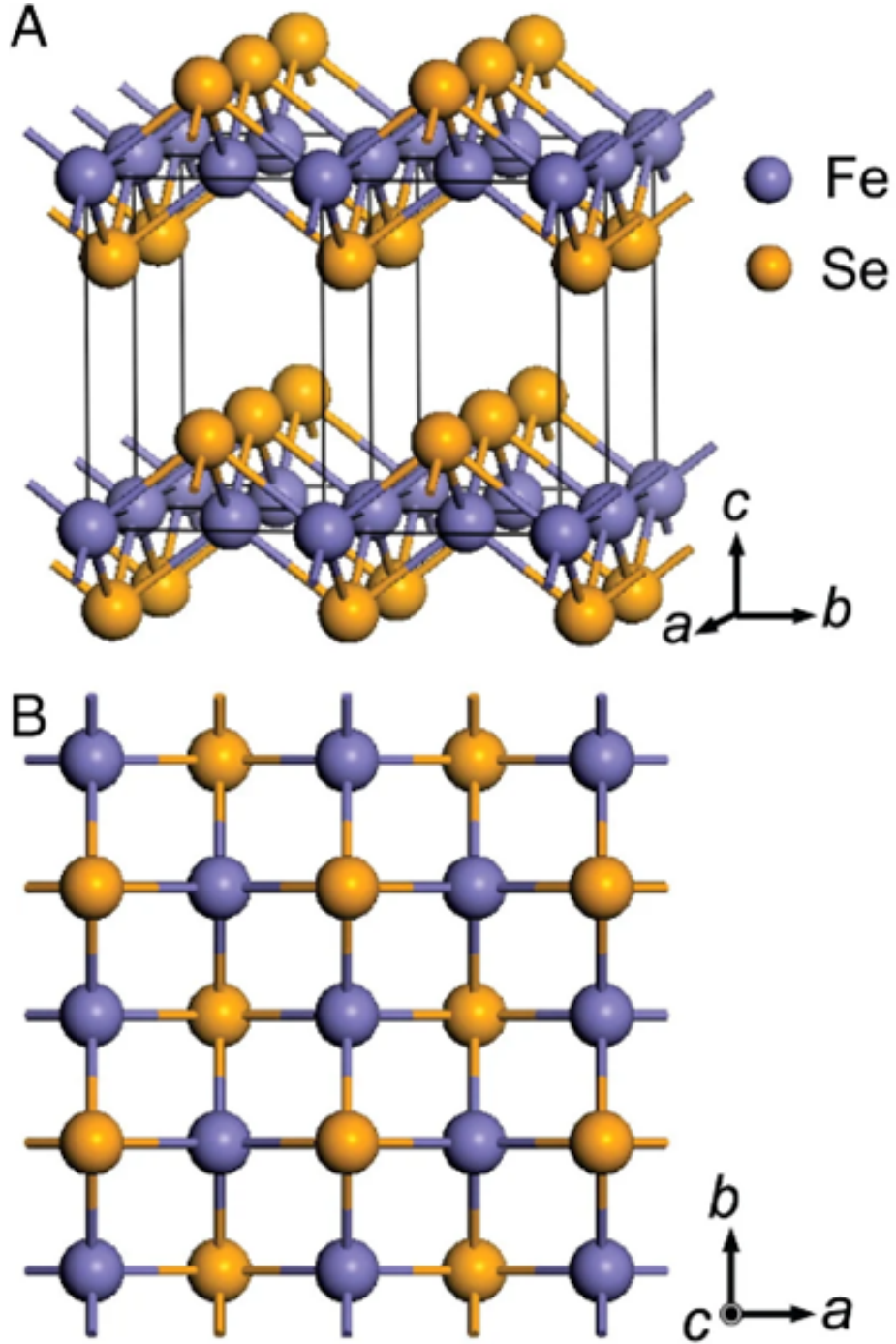
Figure 3.1: a,b) The 2D tetragonal crystal structure of $FeTe_{1-x}Se_x$. The larger spacing between layers bonded by weak vdW forces and smaller spacing in the layer due to strong covalent bonds is visible in (a). The tetragonal structure is most clear from the square structure visible along the c-axis of the material (b). Adapted from Ref. [4].

3.2 Superconductivity in FeTeSe

3.2.1 Notable Attempts to Increasing T_c

As can be seen in the phase diagrams of $FeTe_{1-x}Se_x$, the parent compound FeSe is a superconductor with a T_c of $\sim$9 K in bulk crystals (Refs. [4, 12, 13]) and FeTe is an antiferromagnet which demonstrates no superconductivity (Ref. [11]). $FeTe_{1-x}Se_x$ demonstrates superconductivity within a range of x=0.1 to x=1, depending on the growth process. Despite the non-superconducting nature of FeTe, when FeSe is substituted with Te, the T_c can be enhanced to 14 K. For our $FeTe_{0.55}Se_{0.45}$ crystals, we measured the T_c in the range of 13 K to 14 K, see Fig. 3.3, which is in the typical range for this composition. The highest T_c is typically measured in samples of $FeTe_{0.6}Se_{0.4}$ which can reach $\sim$15 K (Ref. [14]).
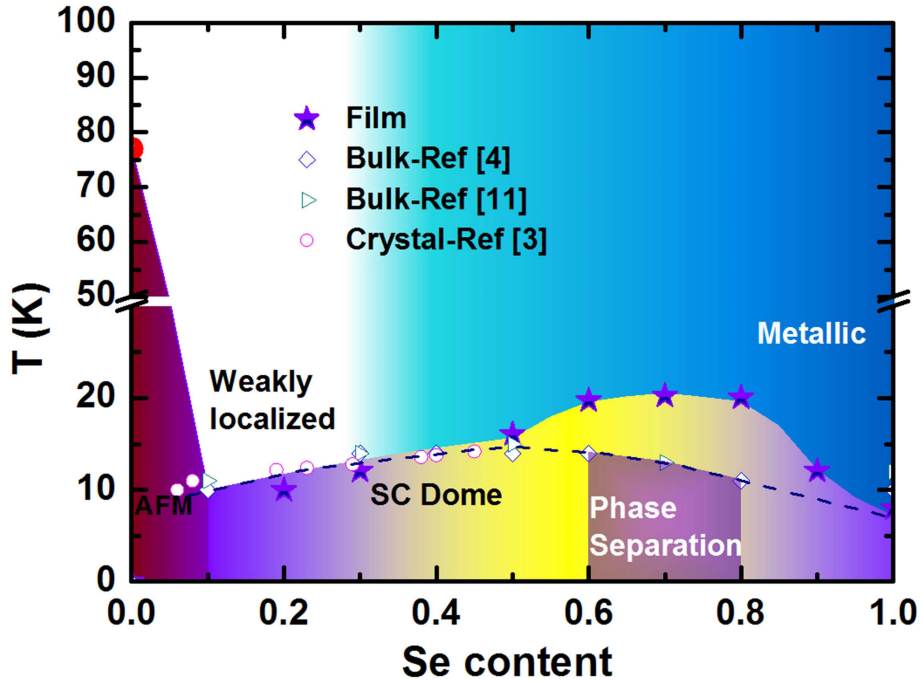
Figure 3.2: Doping dependence of $FeTe_{1-x}Se_x$, showing the antiferromagnetic state when Se = 0.0 and the superconducting state from Se = 0.1 to Se = 1.0. The references in the figure are; *'Bulk-Ref [4]': Ref. [15], 'Bulk-Ref [11]': Ref. [16], 'Crystal-Ref [3]': Ref. [17].* Adapted from Ref. [18].

As with all superconductors, there have been substantial efforts to study and increase the T_c of the family of FeTeSe materials, with the idea of understanding high-temperature
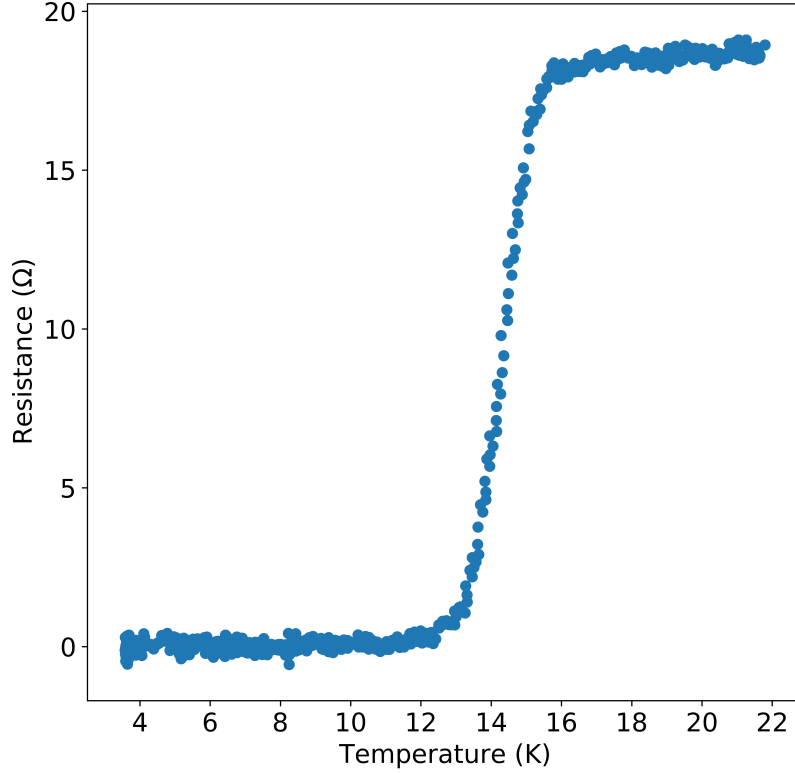
Figure 3.3: Resistance vs temperature that we measured for a $FeTe_{0.55}Se_{0.45}$ flake, showing a T_c around 14 K.

superconductivity or realizing room-temperature superconductivity. Below, I give a summary of the efforts to enhance superconductivity in the class of FeTeSe superconductors.

Initial improvements to the T_c were mostly realized by improving the composition of the crystals. As was mentioned previously, excess iron helps stabilize the growth of FeTeSe crystals (Ref. [19]); however, it is detrimental to the material performance. This was demonstrated in Ref. [14], where they showed an enhancement of the T_c (measured from the onset of superconductivity) from 11.6 K to 14.8 K by reducing the Fe content from $Fe_{1.11}Te_{0.6}Se_{0.4}$ to $Fe_{1.04}Te_{0.6}Se_{0.4}$, as is shown in Fig. 3.4. Further, magnetic susceptibility measurements showed a sharp transition to a diamagnetic state in $Fe_{1.04}Te_{0.6}Se_{0.4}$ suggesting bulk superconductivity, whereas $Fe_{1.11}Te_{0.6}Se_{0.4}$ samples showed a broad transition which

would suggest a reduction in the superconducting volume fraction. They suggested that these excess Fe atoms, which sit between the vdW layers of FeTeSe, are coupled to the Fe in the vdW layers and may lead to the localization of the superconductivity. In order to solve the issue of the beneficial role of excess Fe for growth and the detrimental effect on superconductivity, a number of groups investigated oxygen annealing methods to remove excess Fe after the growth of FeTeSe crystals (Refs. [19–22]). Specifically, it was shown that the excess Fe could be reduced from 1.5% to 0.1% by annealing at 400° C at ~1.5% molar ratio of oxygen to Fe for more than 1 hour (Ref. [19]). The T_c and J_c (critical current density) were enhanced as the O_2 percentage was increased, until around 1.5% when the J_c started to slightly decrease, as is shown in Fig. 3.5.

Another method of increasing the T_c in the family of FeTeSe crystals was pressure. In studies on FeSe crystals, the T_c was enhanced to ~37 K by the application of ~7-9 GPa of hydrostatic pressure (Refs. [23, 24]). At higher pressures, the T_c decreases, and a hexagonal structure arises (Fig. 3.6). The initial increase in T_c up to ~7-9 GPa coincides with the significant reduction of the unit cell volume (~10% at 1.5 GPa). This increases the interaction strength between the atoms, which likely drives the increase in T_c. We will discuss the unconventional mechanism of superconductivity in the family of FeTeSe crystals in Section 3.2.2.

Finally, the largest enhancement in T_c was seen in monolayer FeSe films grown on SrTiO$_3$ substrates. In these devices, a superconducting gap was observed above 65 K (Refs. [25–27]) and later confirmed by studies utilizing Angle Resolved Photoemission Spectroscopy (ARPES) (Refs. [28, 29]) as well as in-situ four-probe measurements (Ref. [30]). The physical origin of the drastic increase in T_c was the subject of intense investigation, and, ultimately, it was suggested that the unusual pairing mechanism of FeSe is enhanced by forward scattering electron-phonon interactions between FeSe and the SrTiO$_3$ substrate, despite not being a typical BCS superconductor (Ref. [31]). This assertion was backed by growing SrTiO$_3$ with different oxygen isotopes, which modifies the strength

14
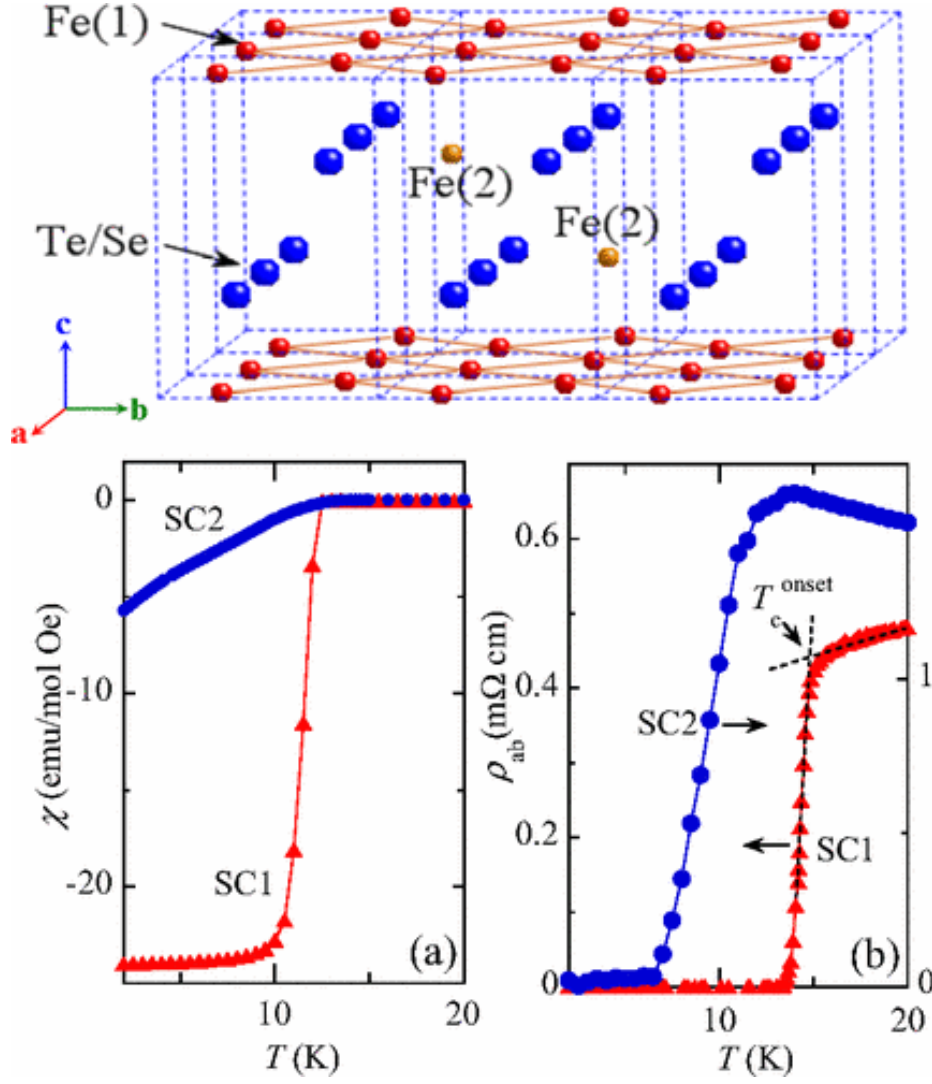
Figure 3.4: T_c enhancement by removing excess Fe atoms. The positions of excess Fe atoms are shown to be at an interstitial location within the crystal. The magnetic susceptibility and resistivity are shown as a function of temperature for the higher Fe concentration (SC2, 11% excess Fe) and for the lower Fe concentration (SC1, 3% excess Fe). The lower Fe concentration improves the diamagnetic response and the T_c of the crystal. Adapted from Ref. [14].

of the electron-phonon interaction (extracted from ARPES measurements), resulting in modifications to the size of the bandgap of FeSe.
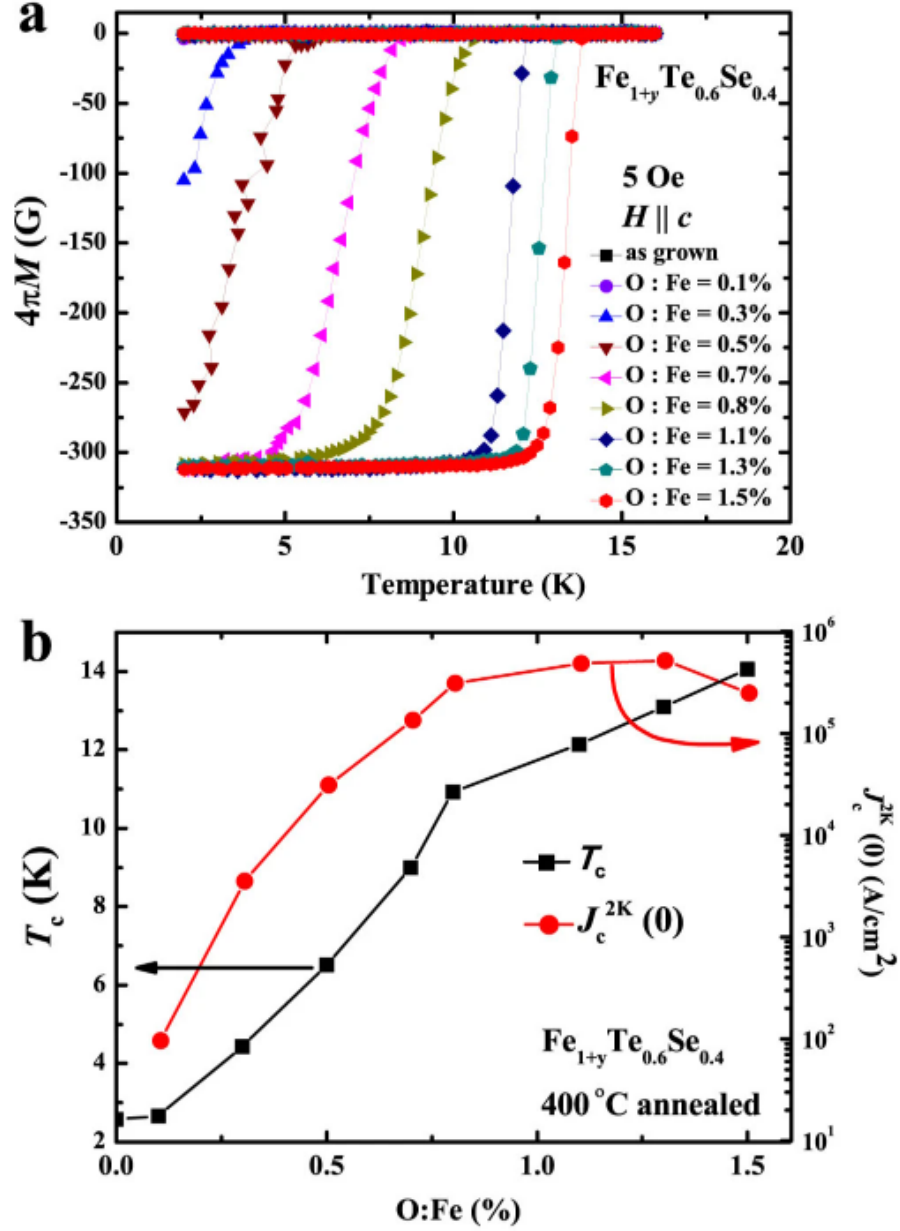
Figure 3.5: The effect of oxygen annealing on removing excess Fe and improving the T_c. The diamagnetic response, critical temperature, and critical current are all enhanced due to the effective removal of excess Fe by oxygen annealing. Adapted from Ref. [19]

3.2.2 Fermi Surface/Pairing Mechanism/Pairing Symmetry

To understand the pairing symmetry in FeTeSe and the larger class of iron-based superconductors, I highly recommend the excellent perspective by Hoffman (Ref. [32]), which I will follow here. In order to discuss the pairing symmetry in FeTeSe, it is instructive to
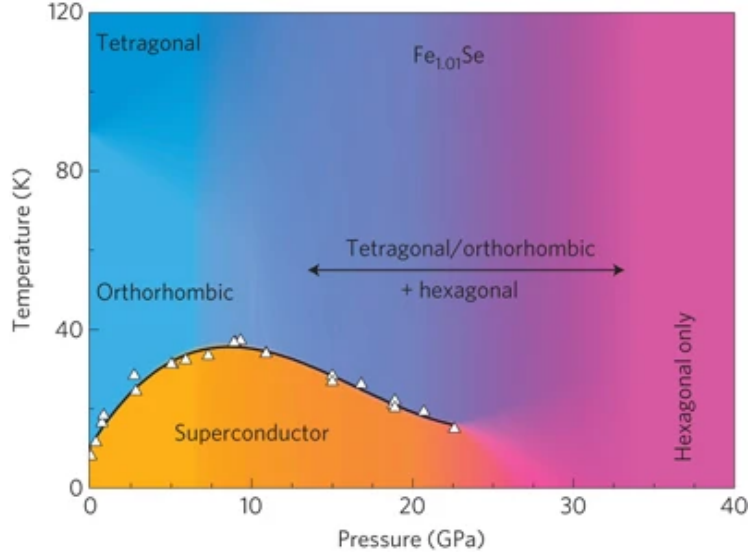
Figure 3.6: A phase diagram showing the pressure and temperature-dependent behavior of FeSe. Specifically, the pressure-dependent enhancement of T_c can be seen until 10 GPa. Afterward, this FeSe begins to undergo a transition to the hexagonal phase. Adapted from Ref. [23]

discuss the Fermi surface in the larger class of iron-based superconductors. Specifically, in the case of $LaFeAsO_{1-x}F_x$, Mazin et al. calculated the Fermi surface in the case of x = 0 (Fig. 3.7) and found that there were two electron cylinders centered on the M point and two hole cylinders centered on the Γ point (Ref. [33]). There is also a heavy hole band at the Γ point; however, Mazin showed that this went away at the relatively small doping of x = 0.04 - 0.05. This Fermi surface turns out to be representative of a large number of iron-based superconductors. It was further deduced by Mazin that these Fermi surfaces may be similar enough to be linked by a small range of K vectors in the Brillouin zone. Two Fermi surfaces linked by a common wavevector result in significant Fermi surface nesting, which may give rise to a number of emergent phenomena. If superconductivity were mediated by spin-fluctuations (a proposed pairing mechanism for the high T_c cuprate superconductors), this would require the order parameter on the electron and hole pockets to have opposite signs. This is denoted as S$\pm$ pairing, as there is a change in the sign of the order parameter between the two pockets (hence $\pm$), but the order parameter is isotropic and nonzero in each of the pockets (hence S). This is in contrast to the nodal order parameter in the d-wave

17

superconductivity of cuprate superconductors, which has multiple lobes.
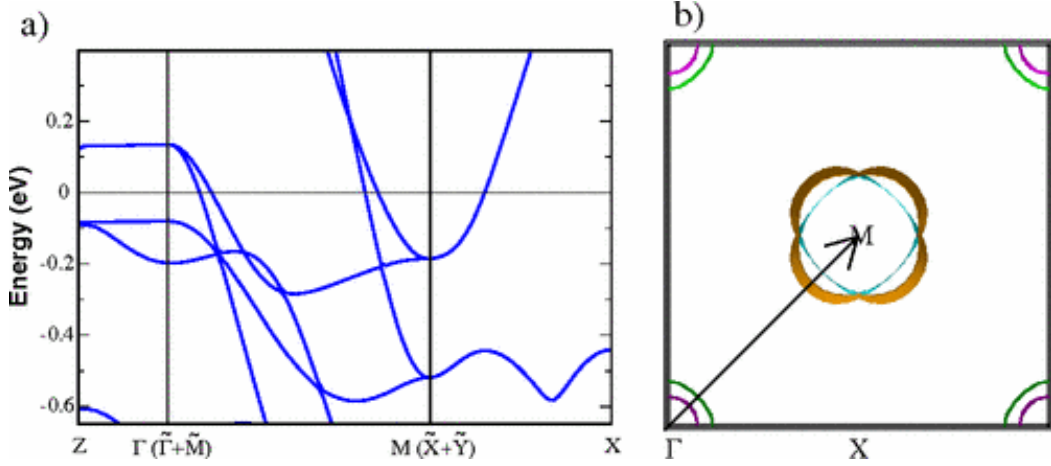
Figure 3.7: The calculated band structure (a) and Fermi surface (b) of $LaFeAsO_{1-x}F_x$. The key properties here are two electron cylinders around the M point and two hole cylinders around the Γ point. Adapted from Ref. [33]

In the case of FeTeSe, the Fermi surface was experimentally verified by orbital-polarization resolved ARPES (Ref. [34]). Further, the spin-fluctuation mediated superconductivity was confirmed using neutron scattering to measure the spin resonance in the superconducting state of $FeTe_{0.6}Se_{0.4}$, which was found to be characterized by a wavevector matching the Fermi surface nesting wavevector (Ref. [35]). Finally, the pairing symmetry was confirmed by scanning tunneling microscopy (STM) (Ref. [36] using a technique known as quasiparticle interference imaging (Ref. [37]). Typical STM measurements either measure the tunneling current as a function of applied bias voltage (Fig. 3.8b), which can reveal the superconducting gap, or map the tunneling current as a function of position (Fig. 3.8a), which can reveal structures within the superconductor. In order to measure quasiparticle interference, the ratio of the conductance at positive bias and negative bias was mapped in order to probe particle-hole symmetric quasiparticles (Fig. 3.8c). A Fourier transform was then applied to this mapping, giving rise to a map of the quasiparticle intensity as a function of wavevector (Fig. 3.8d). Because the different wavevectors scatter between pockets of the same sign or opposite sign, and the magnetic field induces vortices, which may provide additional time-reversal-odd scattering, the intensity of scattering for

the different wavevectors should differ. This is seen in the experimental results, as q3, which connects pockets of the same sign, is enhanced, and q2, which connects pockets of opposite sign, is suppressed (Fig. 3.8e). This confirms the sign reversal of the order parameter between electron and hole pockets and, therefore, the S± pairing symmetry in FeTeSe superconductors.
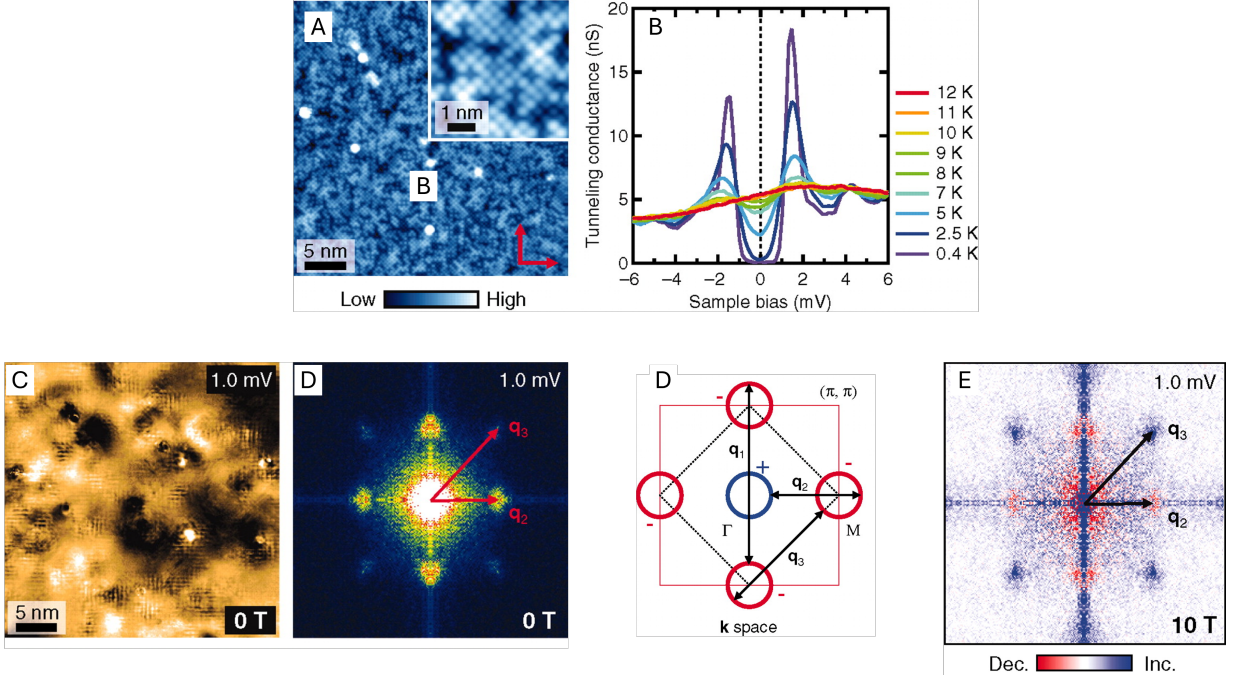
Figure 3.8: Quasiparticle interference probes of the unconventional superconductivity of FeTeSe. a) The tunneling current as a function of position. b) The tunneling current as a function of sample bias, showing the reduced tunneling current due to the quasiparticle gap. c) The ratio of the conductance at positive and negative voltage bias as a function of position. d) The Fourier transform of (c) showing the quasiparticle intensity vs the wavevector. e) The quasiparticle interference under a magnetic field of 10 T showing the enhanced or suppressed scattering based on the phase difference between the pockets, confirming the S± pairing symmetry. Adapted from Ref. [37]

3.3 Topology

One aspect of FeTeSe crystals I have not yet touched on is the topological nature of the electronic states in these crystals. This is central to the interest in FeTeSe as combined

topology and superconductivity give rise to Majorana bound states, which have been posed as an attractive platform for quantum computing. I will begin by providing a brief historical and phenomenological survey of topological materials, which will follow the excellent perspective by Moore (Ref. [38]).

At their simplest level, topological insulators are materials that possess linear-dispersion (Dirac-like, i.e., graphene) electronic states at their surfaces when interfacing with non-topological materials or media. Topological insulators get their name from the mathematical field of topology, which covers the properties of objects or spaces that can be smoothly transformed between one another. Associated with this 'smoothness' is the topological invariant of the system. There is an old joke that a topologist can't tell the difference between a coffee mug and a doughnut. This classic example of topology is based on the idea that a coffee mug can be smoothly deformed into a doughnut without tearing the surface, as both objects have one hole, which serves as the topological invariant in this system. However, transitioning from a ball to a doughnut would require an abrupt transition, i.e., tearing the surface. In crystals, there are many different types of topological invariants, so I will briefly cover the most straightforward examples.

The discovery of the quantum Hall effect, where 1D conductive edge states flow around the edge of a 2D electron gas under external magnetic fields (Ref. [39]), led Haldane to suggest that such an effect could be realized in crystals without an externally applied magnetic field. This led to the idea of topological insulators, which were predicted (Ref. [40]) and later shown to be realizable in a 2D quantum well, characterized by edge states with quantized conductance, shown in Ref. [41]. In this system, the spin-orbit interaction takes the place of the external magnetic field in producing the edge states. After this, a 3D topological insulator was first realized in Bi_xSb_{1-x}, where the dispersion relation of the surface states was revealed and a linear Dirac point was identified (Ref. [42]). These topological surface states arose due to the opening of a band gap by the spin-orbit interactions in these crystals, which induce band inversion.

I will now give a simplified description of what gives rise to topological surface states. In a simple case of a topological crystal, spin-orbit coupling modifies energies in the band structure of the material, and when spin-orbit coupling is strong, these bands can be inverted in the bulk of the material. To match the symmetry of the bands at the interface between a topological insulator and a normal insulator (or vacuum), the inverted bands must revert to the uninverted case. In the process, these bands must cross the Fermi energy, and therefore, electronic states are generated at the surface (Fig. 3.9). In reality, band inversion is not the only requirement for a topological insulator, and the Berry curvature should be calculated around a closed surface in the Brillouin zone, which classifies the topological invariant of the material. Additionally, I have not touched on the symmetries in these systems; the topological states in these systems can be protected by a number of symmetries, such as time reversal symmetry (quantum Hall effect), as well as various crystal symmetries. For a detailed discussion of topological materials, refer to Ref. [43].
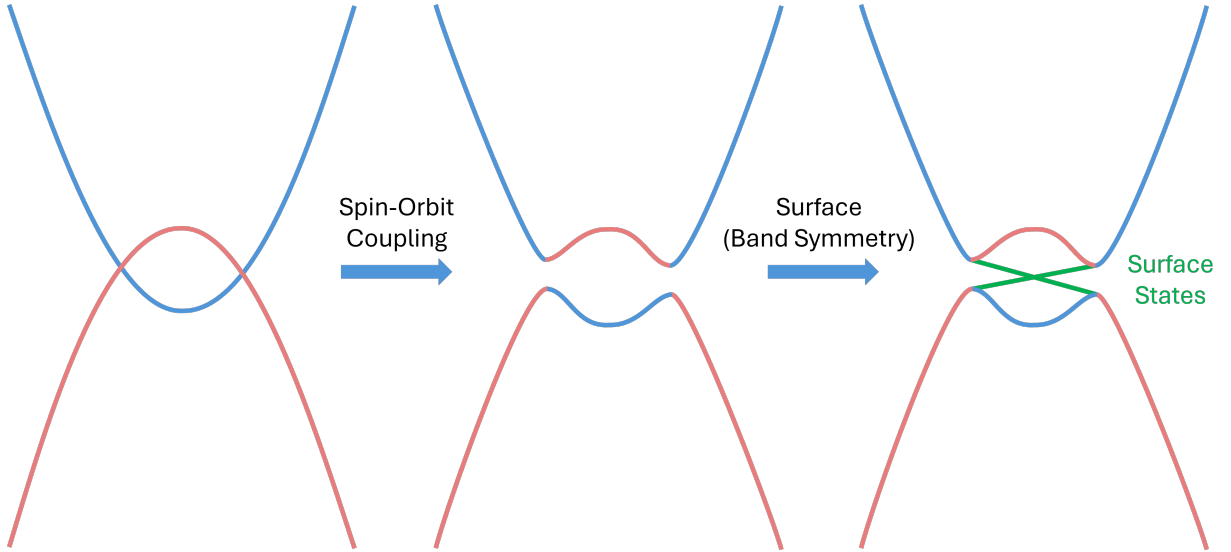
Figure 3.9: Illustration of the band inversion effect giving rise to topological surface states. The strong spin-orbit coupling opens a bandgap and causes twisting of the bands (i.e., band inversion). At the interface with materials without band inversion, the bands must be reverted to an untwisted non-inverted state and must cross to do so. This closes the bandgap locally, giving rise to topologically protected surface states.

Now that a simple understanding of topological materials has been established, we

can touch on the suggested topology of FeTeSe, which is still being debated. Unlike in the above examples, FeTeSe is not an insulating material in the bulk. Although the insulating states in the bulk of topological insulators make the isolated measurement of the surface states easier, the topological nature of the surface states is not dependent on an insulating bulk of the material. Additionally, because both the topological states and the current flow in superconductors happen at the surface, probes of the topology of FeTeSe are still realizable, as will be shown next.

3.3.1 Topology In FeTeSe

The topological states in FeTeSe were first intensively investigated by Wang et al. (Ref. [44]), who carried out first principle calculations of the band structure comparing the band structure of FeSe and $FeTe_{0.5}Se_{0.5}$, as well as ARPES measurements of $FeTe_{0.5}Se_{0.5}$ crystals to support their findings. Intuitively, the heavier Te atoms, as opposed to the lighter Se atoms, would suggest an increased magnitude of spin-orbit coupling, due to the relativistic nature of this effect. Therefore, one may imagine that as the content of Te is increased, the topologically trivial FeSe may transition to a topologically non-trivial state in $FeTe_{1-x}Se_x$. Calculations of the band structure of FeSe and FeTeSe revealed similar structures, with electron and hole pockets around the M and Γ points, respectively, as is typical for most Fe-based superconductors. However, there is one clear difference between these two band structures. Relative to the case of FeSe (Fig. 3.10a), in FeTeSe (Fig. 3.10b) the Γ_2^- band (bolded in red) is pushed down in energy, and along the Γ-Z direction now crosses the Fermi energy, as well as other bands near the Fermi level. After this, the authors added the spin-orbit interaction to their calculation (Fig. 3.10c), which reveals that one of the crossings is avoided due to the spin-orbit interaction and a bandgap is opened (Fig. 3.10d). This avoided crossing mixes (often referred to as twists) the bands, similar to the case of traditional 3D topological insulators, resulting in band inversion. They confirmed a non-zero topological invariant, assuming a curved chemical potential represented by a

dashed line. Topological surface states can arise in non-insulating materials, and therefore, utilization of a curved Fermi surface is necessary to exclude any effects of the chemical potential crossing a band on the calculated Berry curvature. After this, the Γ_-^2 band crossing the Fermi energy was confirmed by ARPES measurements taken as a function of successive K doping of the $FeTe_{0.5}Se_{0.5}$ crystals.
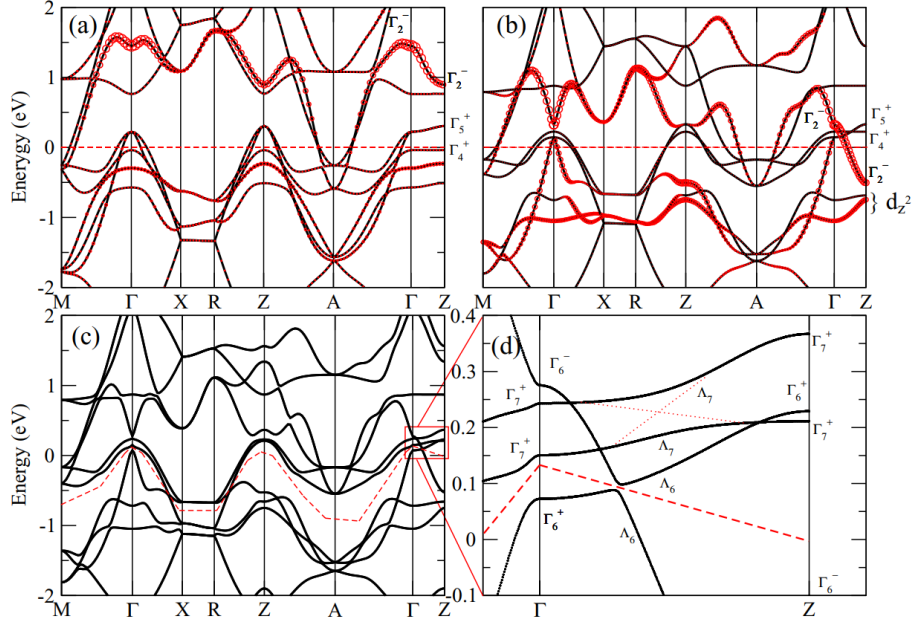
Figure 3.10: First principles calculation of the band structure of FeTeSe, revealing band inversion and a non-zero topological invariant. a) The band structure of FeSe. b) the band structure of FeTeSe, neglecting the spin-orbit interaction. The main difference from FeSe (a) is that the Γ_-^2 band (bolded in red) is pushed down in energy and crosses the Fermi energy along the Γ-Z direction. c) The band structure of FeTeSe after adding the spin-orbit interaction. d) A zoom-in on the Γ-Z direction showing the avoided crossing which gives rise to the band inversion and topology in FeTeSe. Adapted from Ref. [44]

3.4 Topological Superconductivity

So, what is the significance of topological surface states in FeTeSe? This significance is related to Majorana bound states, which can emerge when superconducting and topological systems are combined, and may have applications in topologically protected quantum computation due to their unique exchange statistics. Below, I will give a brief overview

of Majorana Fermions, Majorana-bound states, and a simple description of the exchange statistics. For a more in-depth discussion, please refer to the referenced articles.

The term Majorana Fermion refers to a Fermion which is its own antiparticle, and was originally proposed in the context of particle physics. Because particles and antiparticles must have opposite charge, a Majorana Fermion, which is its own antiparticle, must have zero charge. In superconducting systems, electron-hole symmetry is imposed by the superconducting condensate, and quasiparticle excitations that are combinations of electron and hole creation operators can be generated (Ref. [45]). These quasiparticles are commonly referred to as Bogoliubov quasiparticles. Among the Bogoulibov quasiparticles in a typical superconductor, a Majorana Fermion may be generated if a quasiparticle is its own antiparticle. In order to realize such a quasiparticle, the normal electron states in the superconductor must follow a linear Dirac-like dispersion, according to Ref. [46]. Based on this idea, in 2008, breakthrough theoretical works by Fu and Kane (Refs. [47, 48]) suggested that a superconductor coupled to the linear dispersion of electron states in a topological insulator could realize Majorana bound states. They demonstrated that these Majorana bound states would exhibit non-Abelian exchange statistics that would make them useful for quantum computation.

A brief note on exchange statistics: Abelian exchange statistics are what describe typical Fermions and Bosons, which accrue a complex phase $e^{i\phi}$ in the wavefunction when two particles positions are exchanged, where $e^{i\phi}$ will be 1 for Bosons (due to the symmetric wavefunction) and -1 for Fermions (due to the antisymmetric wavefunction). Non-Abelian exchange statistics imply that when two particles are exchanged, a phase is accrued and, critically, the mode of the wavefunction is modified as well. Further, the non-abelian exchange statistics imply the wavefunction depends on the order in which particle exchanges are performed and the rotation direction of the exchange. Since the wavefunction can be controlled this way, a method of entanglement known as braiding was proposed as a basis for qubits. Figure 3.11 shows a schematic of Majorana braiding where the qubit is initially

in the ground state ($|0_{12}0_{34}\rangle$) and finally in a superposition of the ground and excited state $((|0_{12}0_{34}\rangle + |1_{12}1_{34}\rangle)/\sqrt{2})$.
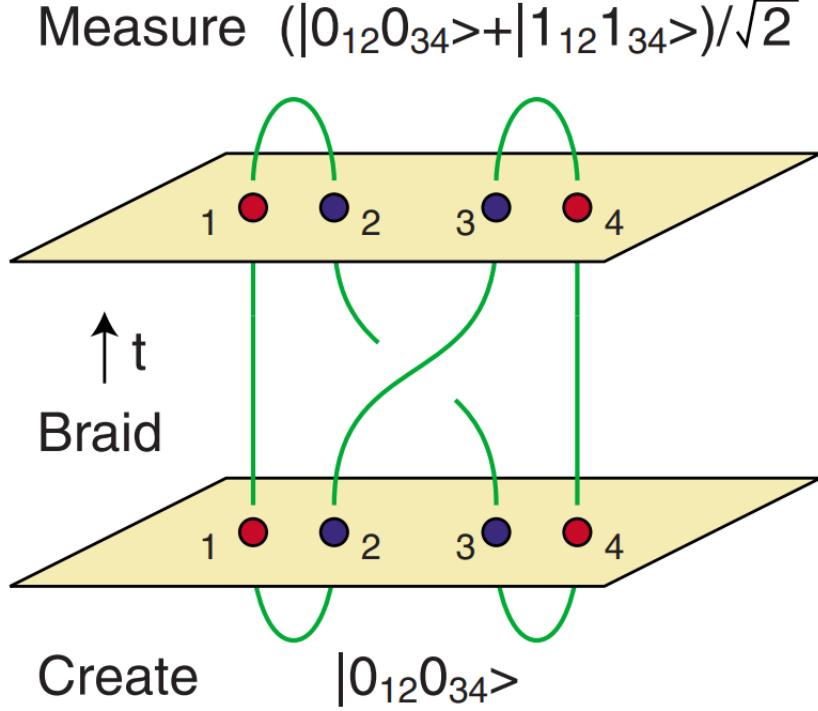
Figure 3.11: Illustration of braiding operations on Majorana bound states. The Majorana wavefunction starts in the ground states defined by pairs of Majorana particles. By exchanging the particles' positions, the wavefunction will now be in a superposition of the ground and excited states. For successive braiding operations, the order of exchanges affects the final state. Adapted from Ref. [43]

3.4.1 Topological Superconductivity in FeTeSe

Along with the prediction of surface states in FeTeSe by Wang et al. (Ref. [44]), the author also noted that the combination of topological surface states and superconductivity in a single material (FeTeSe) could give rise to Majorana bound states on the surface of FeTeSe. The superconducting quasiparticle gap Δ, however, will 'gap out' these surface states, making them inaccessible to experimental probes. Fortunately, the order parameter (and therefore the quasiparticle gap) becomes zero at the core of Abrikosov vortices (Fig. 3.12). Therefore, it was predicted that Majorana bound states could be bound to

the cores of Abrikosov vortices in topological superconductors (Refs. [47, 49]). ARPES measurements were able to prove topological superconductivity in FeTeSe by imaging the spin-polarized Dirac-like surface states of $FeTe_{0.55}Se_{0.45}$ as well as proving the s-wave nature of the superconductivity (Ref. [50]).
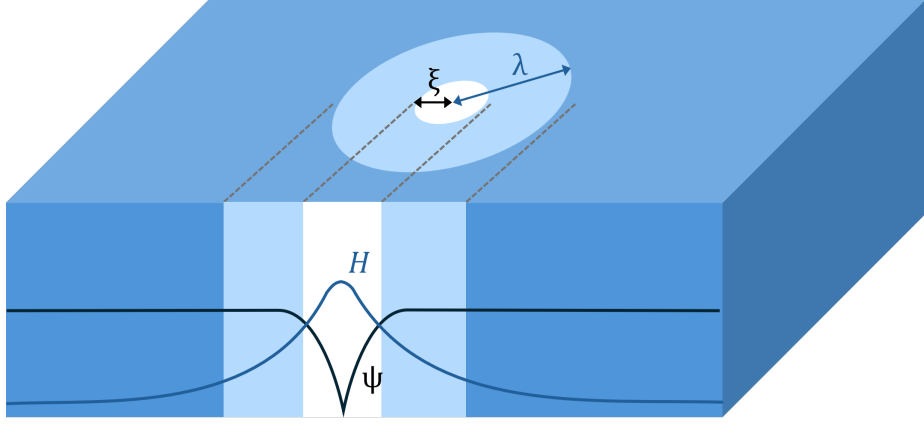
Figure 3.12: Illustration of a vortex in a superconductor. The order parameter (ψ) is reduced inside a radius equal to the coherence length (ξ), eventually becoming zero at the core of the vortex. The magnetic field intensity (H) decays over the penetration depth of the superconductor (λ).

That same year, the first direct experimental probe of Majorana bound states in FeTeSe was achieved (Ref. [51]). This was achieved using STM, which we discussed above for the determination of the pairing symmetry. STM locally probes the density of states as a function of energy by measuring the tunneling conductance from an atomically sharp tip as a function of bias voltage. Additionally, STM is able to resolve spatial features with a resolution smaller than 0.1 nm, which allows spatial probing on the atomic scale, and is much smaller than the nm scale vortices. With these advantageous properties Wang et al. (Ref. [51]) were able to image vortices on the surface of $FeTe_{0.55}Se_{0.45}$ under an applied magnetic field of 0.5 T. The tunneling conductance was then measured as a function of energy at the center of the vortex and at the edge of the vortex (Fig. 3.13). These measurements reveal a zero-bias peak in the conductance at the center of the vortex, a signature of tunneling through the Majorana bound states, which are predicted to occur at zero energy (Refs. [47–49]). The author also ruled out Caroli de Gennes Matricron (CdGM)
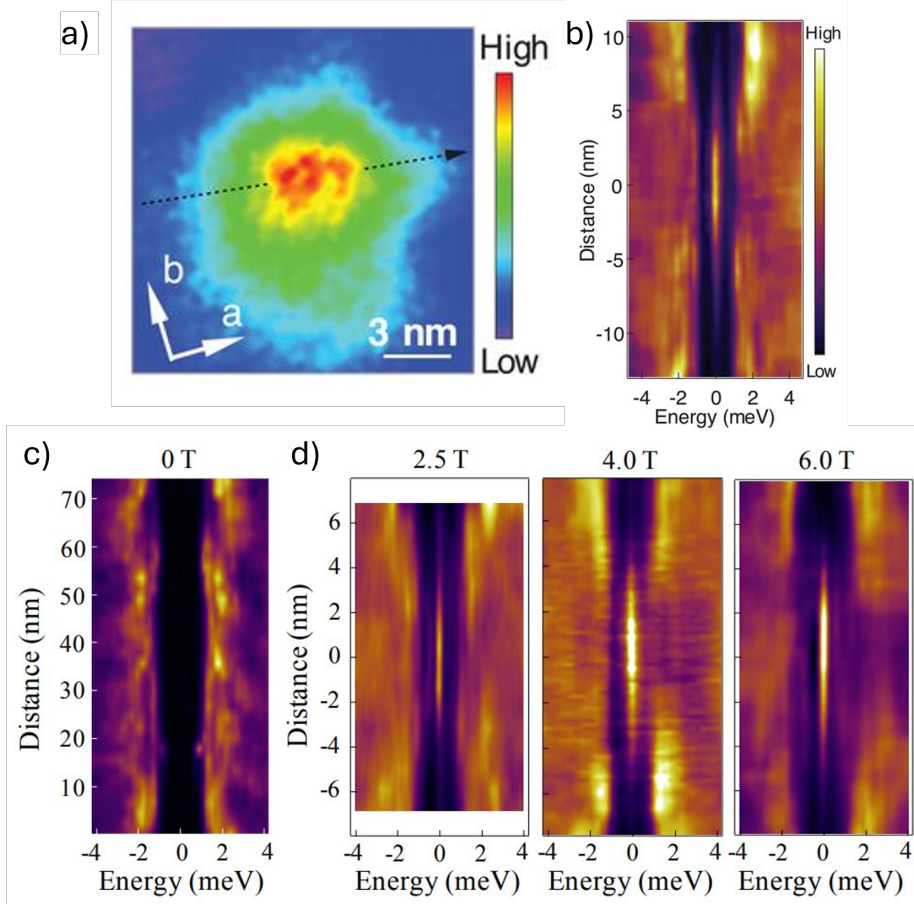
Figure 3.13: A direct probe of Majorana bound states at the core of a superconducting vortex using STM. A peak in the conductance can be seen at the core of the vortex using STM (a). This peak in the conductance can be shown to be centered on zero energy, as well as at the core of the vortex (b). An insensitivity to magnetic field was also demonstrated, ruling out CdGM states and Kondo resonances (c,d). Adapted from Ref. [51]

states (Ref. [52]) and Kondo resonances (Ref. [53]), which can occur at low energies and masquerade as Majorana bound states. In the case of CdGM states, these are predicted to occur at discrete energy levels of $\mu\Delta^2/E_F$ for $\mu = 1/2, 3/2, 5/2, ...$ (Ref. [52, 54]). However, the most convincing evidence is that CdGM states should split as a function of space when moving away from the vortex center (Ref. [55]), this behavior was not observed, see Fig. 3.13b. In regard to Kondo resonances, these tunneling states would typically take place at a magnetic impurity, and as a function of applied magnetic field, should split in energy (Ref. [56]), which was also not observed (Fig. 3.13c,d).

3.4.2 Higher Order Topological Superconductivity in FeTeSe

So far, we have discussed topological materials in which the topological states exist with dimensions $N-1$, where N is the dimension of the parent material (1D edge states in 2D Electron gases, 2D surface states in 3D topological insulators). However, it is possible to have what is known as a higher-order topological insulator, where topological states can exist in $N-2$ (1D edge modes in a 3D platform) or $N-3$ dimensions (0D bound states in a 3D platform). Zhang, Cole, and Das Sarma (an early pioneer of topological superconductivity) predicted that higher order topological superconductivity could potentially be realized in FeTeSe, due to the combination of 2D topological surface states and anisotropic S± pairing symmetry (Ref. [57]). They showed that the anisotropy would result in surface states on the top surface with a sign reversal of the pairing potential compared to the side surfaces. Due to the sign reversal of the pairing potential, there must be an angle where the pairing potential passes through zero, and therefore, the superconducting gap is closed, resulting in 1D helical hinge Majorana zero modes. Fig. 3.14 from Ref. [58] schematically shows how topology and S± superconductivity come together to realize this phenomenon.

3D Topological Insulator   **s± Superconductor**   **Helical Majorana Hinge Mode**
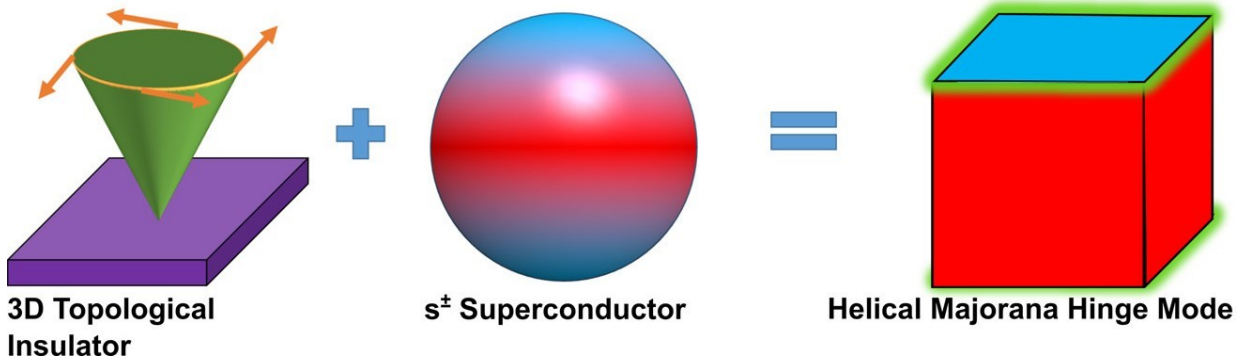
Figure 3.14: Visualization of the S± superconductivity on the surfaces of FeTeSe, and the resulting helical hinge zero modes. The closing of the superconducting gap at an angle between the two surfaces of FeTeSe and the topological surface states give rise to the higher order topology in this material. Adapted from Ref. [58].

That same year, Gray et al. confirmed the existence of these helical hinge zero modes (Ref. [58]). They fabricated two types of contacts to $FeTe_{0.55}Se_{0.45}$, (1) using a hexagonal

boron nitride insulating layer to block the hinge so the electrode only touches the top surface, and (2) contacting both the hinge and the top surface. They found a sharp peak in conductance at zero bias in the sample contacting the edge, which was absent in the contact to the top surface (Fig. 3.15). Additionally, they demonstrated that this peak likely does not arise from Andreev bound states by showing that the temperature dependence differed from what would be expected of Andreev bound states ($\propto \frac{1}{T}$). The discovery of helical hinge Majorana zero modes in $FeTe_{0.55}Se_{0.45}$ provides further evidence of the S± pairing symmetry, as gap anisotropy is necessary to realize these higher-order topological states.
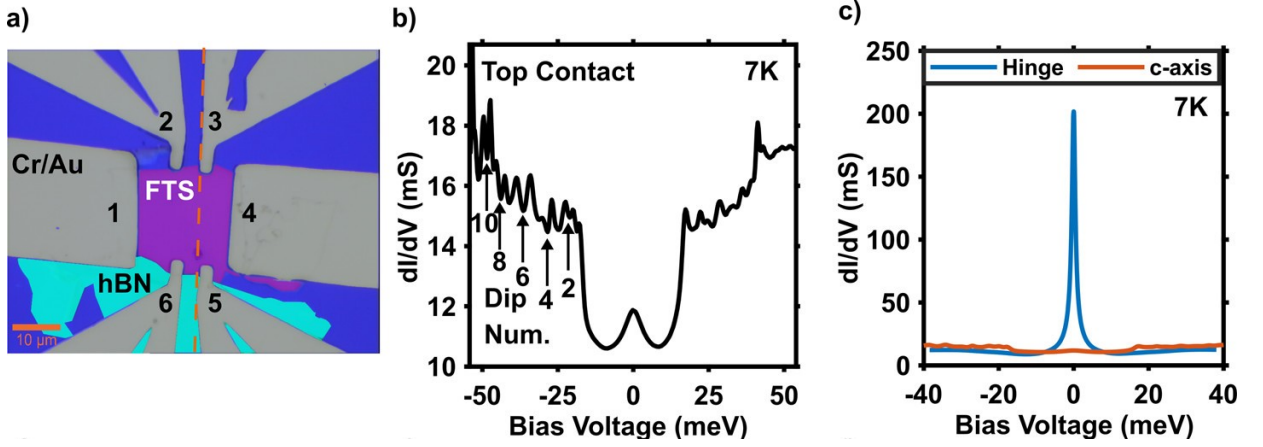
Figure 3.15: a-c) A transport study on FeTeSe (a) revealing a zero bias conductance peak when the electrode is in contact with the edge of the sample (c), which is absent when just contacting the top surface (b), confirming the presence of helical hinge zero modes. The small peak in (b) is likely due to tunneling through the hBN into the helical hinge zero mode, which exists at zero energy. Adapted from Ref. [58].

3.5 Josephson Effects in FeTeSe-Based Devices

Although we will discuss the specifics of Josephson junctions in the following Chapters, I will now give an overview of the current research that has been conducted on FeTeSe-based Josephson junctions. The first study revealing Josephson effects in FeTeSe was performed by Wu et al. (Ref. [59]). In their study, they fabricated FeTeSe-based constriction junctions using a focused ion beam to etch the FeTeSe down to widths ranging from ~250 nm to

~650 nm (Fig. 3.16a). In these devices they measured Shapiro steps matching the predicted height (Fig. 3.16b), as well as large induced gaps of up to 2 meV, determined by the I_cR_n product and the Ambegaokar-Baratoff relation, described in Ref. [60] (see chapter 5 for a more detailed discussion of the Ambegaokar-Baratoff relation). Another FeTeSe-based Josephson junctions was produced by Qiu et al. by stacking two FeTeSe crystals on top of one another (Fig. 3.17a). In this device they measured a number of novel properties, but most relevant to this study was the unusual dependence of the critical current on the magnetic field (Fig. 3.17b). This unusual dependence appears to be a mix of a 0-Junction (the typical case) and a π-Junction (typically only in systems with magnetic materials or multiband superconductors). They suggested that these effects arise due to ferromagnetism at the interface between the two FeTeSe flakes. However, they pointed out that excess Fe, which would be the most obvious cause of the interfacial ferromagnetism, is not likely driving the ferromagnetic behavior in these devices, as the hysteresis effects disappeared above the superconducting critical temperature of FeTeSe.
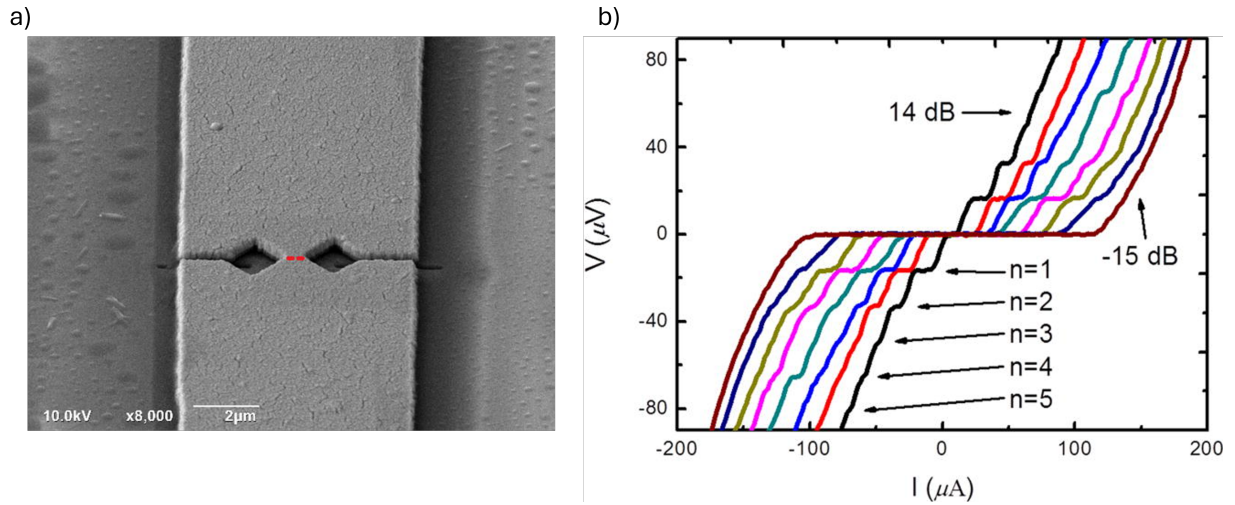
Figure 3.16: a) A constriction Josephson junction fabricated from FeTeSe crystals. b) Shapiro steps were reliable in this system, confirming the realization of a Josephson junction in this device. Adapted from Ref. [59].
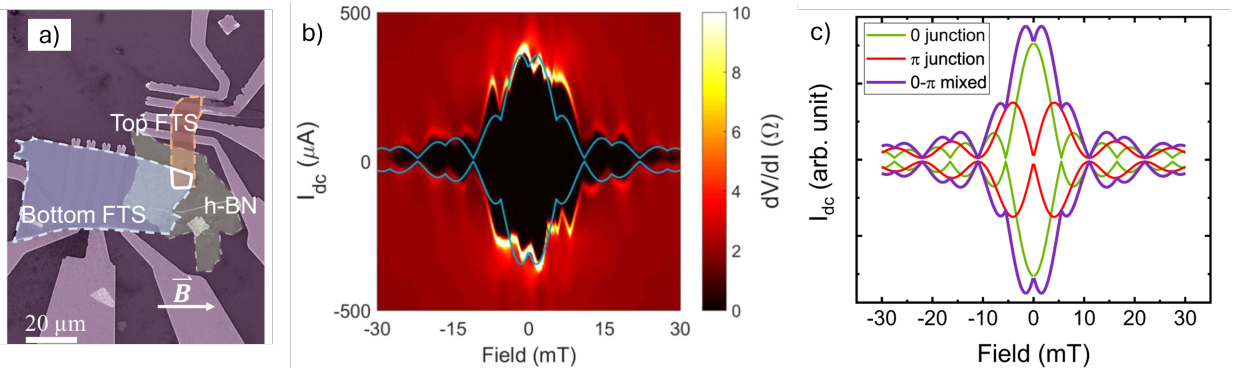
Figure 3.17: a) A FeTeSe-FeTeSe homojunction where the vdW gap between he crystals allows for tunneling between the FeTeSe flakes. b) The complicated magnetic field dependence of the critical current, showing asymmetry in B and a minimum close to zero. c) The description for the unusual magnetic field dependence is a combination between 0-junction behavior (the typical case) and π-junction behavior (arising in Josephson junctions with multiband superconductors or magnetic insulating layers). Adapted from Ref. [61].

Chapter 4

Josephson Junctions

4.1   Josephson Physics

Josephson junctions are devices where two superconducting electrodes are separated by
a thin non-superconducting region (Ref. 4.1). When the non-superconducting region
is thinner than the relevant coherence length (the superconductor coherence length in a
superconductor-insulator-superconductor junction and the normal metal coherence length
in a superconductor-normal metal-superconductor junction), there will be tunneling of
cooper pairs between the superconducting banks. As a consequence of the phase-coherent
transport, Josephson junctions demonstrate zero resistance for pair tunneling at zero bias
voltage, but finite resistance (in general) at finite bias. Brian Josephson first described
the governing equations of Josephson junctions in 1962, which are known as the Josephson
equations (Ref. [62]). Below, we will discuss the derivation of the Josephson equations as
well as the primary phenomena observable in this system.

4.1.1   Derivation of Josephson Equations

As Ginzburg-Landau theory demonstrates, each of the superconducting electrodes in a
Josephson junction can be described by a macroscopic wave function, respectively.
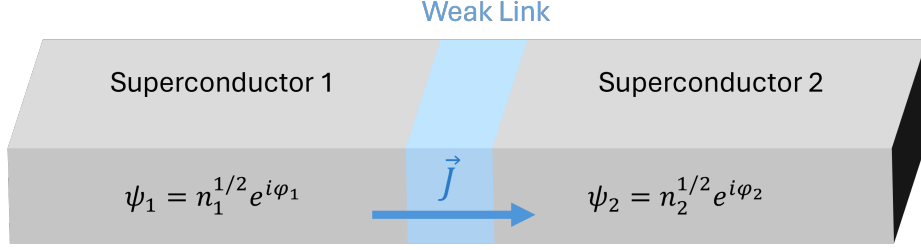
Figure 4.1: Schematic of a Josephson junction showing the macroscopic wavefunction of each superconducting electrode.

$$\psi_1 = \sqrt{n_1}e^{i\varphi_1} \tag{4.1}$$

$$\psi_2 = \sqrt{n_2}e^{i\varphi_2}, \tag{4.2}$$

where φ_1 and φ_2 are the macroscopic phases of the first and second superconducting electrodes, respectively, and n_1 and n_2 are the densities of Cooper pairs. We will later assume the electrodes are identical for simplicity; however, the electron densities must first be handled independently, as the charge passing from one electrode to the other will be represented by $\dot{n}_1$ or $\dot{n}_2$. This does not violate $n_1 = n_2$, because our system is attached to a battery, so the electrodes will not become charged by a finite $\dot{n}_1$ or $\dot{n}_2$. These equations do not explicitly account for the battery as a charge source or sink; therefore, this must be handled through a reasonable assumption which I will cover later.

The time-independent Schrodinger equation for a two-level system can be used to describe the coupling between the two electrodes, where the ground state energy U characterizes zero coupling between the two superconductors and the excited state energy K characterizes the coupling energy between the two electrodes. Because we will apply a voltage V between the two superconducting electrodes, we can assume $U_1 = +V/2$ and $U_2 = -V/2$. For now, we exclude the contribution of magnetic fields.

$$i\hbar\frac{d\psi_1}{dt} = \frac{qV}{2}\psi_1 + K\psi_2. \tag{4.3}$$

$$i\hbar\frac{d\psi_2}{dt} = -\frac{qV}{2}\psi_2 + K\psi_1. \tag{4.4}$$

Substituting the wavefunction of each electrode into the time-dependent Schrodinger equation results in the equations

$$i\hbar(\sqrt{\dot{n}_1} + i\dot{\varphi}_1\sqrt{n_1})e^{i\varphi_1} = \frac{qV}{2}\sqrt{n_1}e^{i\varphi_1} + K\sqrt{n_2}e^{i\varphi_2}, \tag{4.5}$$

$$i\hbar(\sqrt{\dot{n}_2} + i\dot{\varphi}_2\sqrt{n_2})e^{i\varphi_2} = -\frac{qV}{2}\sqrt{n_2}e^{i\varphi_2} + K\sqrt{n_1}e^{i\varphi_1}. \tag{4.6}$$

By equating the real and imaginary parts of each equation, we arrive at four equations. Where we have defined the phase difference between the junction as $\delta = \varphi_1 - \varphi_2$.

$$\dot{n}_1 = \frac{2K}{\hbar}\sqrt{n_1 n_2}\sin(\delta) \ , \ \dot{n}_2 = -\frac{2K}{\hbar}\sqrt{n_1 n_2}\sin(\delta), \tag{4.7}$$

$$\dot{\varphi}_1 = \frac{K}{\hbar}\sqrt{\frac{n_2}{n_1}}cos(\delta) - \frac{qV}{2\hbar} \ , \ \dot{\varphi}_2 = \frac{K}{\hbar}\sqrt{\frac{n_1}{n_2}}cos(\delta) + \frac{qV}{2\hbar}. \tag{4.8}$$

Where we can see that

$$\dot{n}_1 = -\dot{n}_2. \tag{4.9}$$

This represents the transport of Copper pairs between the electrodes, and as such, we can write

$$J = \frac{2K}{\hbar}\sqrt{n_1 n_2}\sin(\delta) = \dot{n}, \tag{4.10}$$

where J is the current density. Now we can make the reasonable assumption that $n_1 = n_2$, based on the idea that the Josephson junction is connected to a battery that will source or sink the charge in each electrode as the current flows through the junction. With this, we can additionally define $J_o = \frac{2K}{\hbar}n_1$. This is the critical current density of the Josephson junction, and is analogous to the critical current density of a superconductor on a simple

level. Using this definition, the first Josephson equation can be written as

$$J = J_o \sin(\delta). \tag{4.11}$$

By subtracting the equations in Eq. 4.8, and using our previous definition for the phase difference between the superconductors, we can write the second Josephson equation

$$\dot{\delta} = \frac{2eV}{\hbar}, \tag{4.12}$$

where we have substituted $q = 2e$ for the Cooper pair. And its time-integrated form.

$$\delta(t) = \delta_0 + \frac{2e}{\hbar} \int V(t)dt \tag{4.13}$$

The result of this equation is that if a finite DC voltage is applied across the junction, the phase will change at a constant rate, given in Eq. 4.12, causing oscillations of the current (Eq. 4.11), and there will be no net current flow from the superconducting state. In real devices, there will be conduction due to quasiparticles at this point, however, they are not treated within this model. A typical current-voltage curve, as measured by Shapiro et al., is shown in Fig. 4.2, where the voltage was swept (y-axis) and the tunneling current was measured (x-axis).

In comparison, if a small current less than J_o is driven through the junction, then there will be a constant finite phase difference between the superconducting electrodes, given by Eq. 4.11. From Eq. 4.12, this would mean that the voltage across the junction must be zero. Driving a current instead of a voltage is referred to as a current-bias measurement and is discussed in detail in Sec. A.1.2.
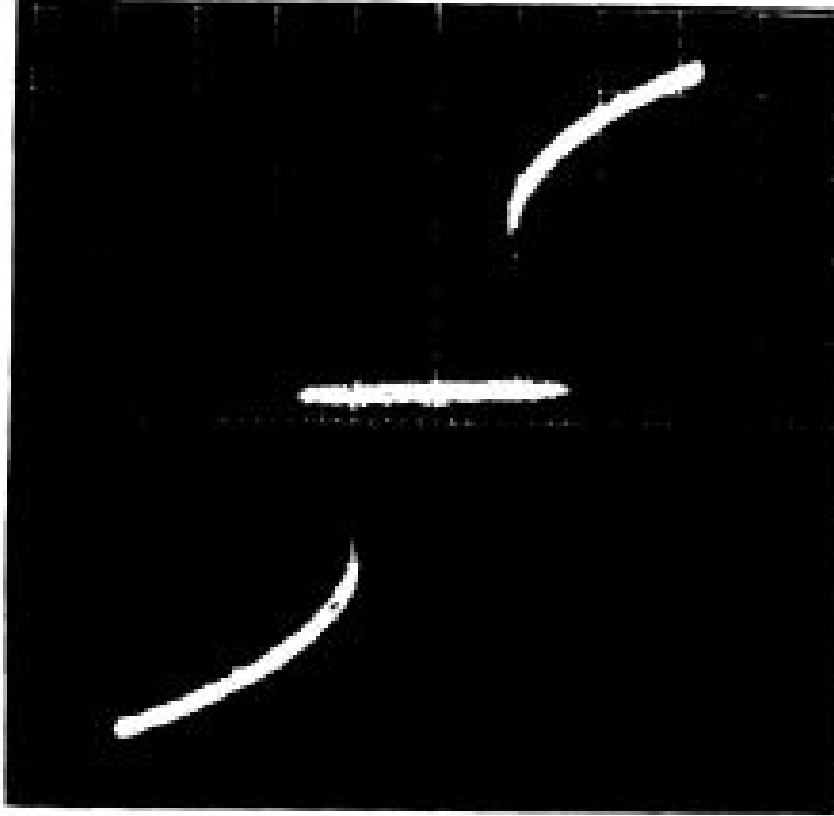
Figure 4.2:   A typical current-voltage curve, where current is shown on the x-axis and voltage is shown on the y-axis, adapted from Ref. [63].

4.1.2   Shapiro Steps

Only one year after Josephson's landmark publication, Sidney Shapiro measured the existence of finite jumps in the current-voltage curve in a Josephson junction irradiated by microwave photons (Ref. [63]). We will next discuss this phenomenon in detail.

Due to the microwave photons irradiating the sample, the voltage across the junction can be expressed as the sum of the DC voltage V_0 and the AC voltage V_1,

$$V = V_0 + V_1 \cos(\omega_1 t). \tag{4.14}$$

Substituting this into the integral form of the second Josephson equation (Eq. 4.13) results

in the equation

$$\delta(t) = \delta_0 + \frac{2eV_0}{\hbar}t + \frac{2eV_1}{\hbar\omega_1}\sin(\omega_1 t). \tag{4.15}$$

Substituting this into the first Josephson equation (Eq. 4.11), results in the equation

$$J = J_o \sin\left(\delta_0 + \frac{2eV_0}{\hbar}t + \frac{2eV_1}{\hbar\omega_1}\sin(\omega_1 t)\right). \tag{4.16}$$

Equations of the type $\sin(\sin(x))$ can be expanded as a sum of Bessel functions, resulting in the equation

$$J = J_o \sum (-1)^n \mathcal{J}_n\left(\frac{2eV_1}{\hbar\omega_1}\right)\sin\left(\gamma_0 + \frac{2eV_0}{\hbar}t - n\omega_1 t\right), \tag{4.17}$$

where $\mathcal{J}_n$ is the nth Bessel function of the first type. The current will oscillate with time and average out to zero unless $n\omega_1 = \frac{2eV_0}{\hbar}$ is satisfied. At which point, there will be a DC contribution for the nth term in the series. As a result, if the voltage is increased, there will be no increase in current until

$$V_0 = \frac{n\hbar\omega_1}{2e} = \frac{nhf}{2e}, \tag{4.18}$$

where the applied frequency f is typically in the range of GHz, and the voltage steps correspond to $\sim 2\mu V/GHz$. Similarly, if a current is applied to the junction, the voltage will remain constant until sufficient current exists to drive the voltage to jump to the nth step, shown in Fig. 4.3. This results in finite jumps in the current-voltage curves known as Shapiro steps, shown in Fig. 4.3.

Deviations from the typical Shapiro step behavior can be used as a probe of the properties of Josephson junctions. For example, voltage jumps occurring at fractional values of the Shapiro steps can indicate deviations from the typical current-phase relation $(\dot\delta = \frac{2eV}{\hbar})$. Specifically, higher frequency sinusoidal contributions to the current-phase relation can arise in highly transparent Josephson junctions, as is shown in Ref. [64].

Another example is the missing odd-value Shapiro steps, which are predicted to arise in the presence of Majorana bound due to the 4π period current phase relationship (Refs. [65, 66]). However, missing odd Shapiro steps have been observed in topologically trivial Josephson junctions as well (Ref. [67]), and therefore this is not direct evidence of Majorana bound states.
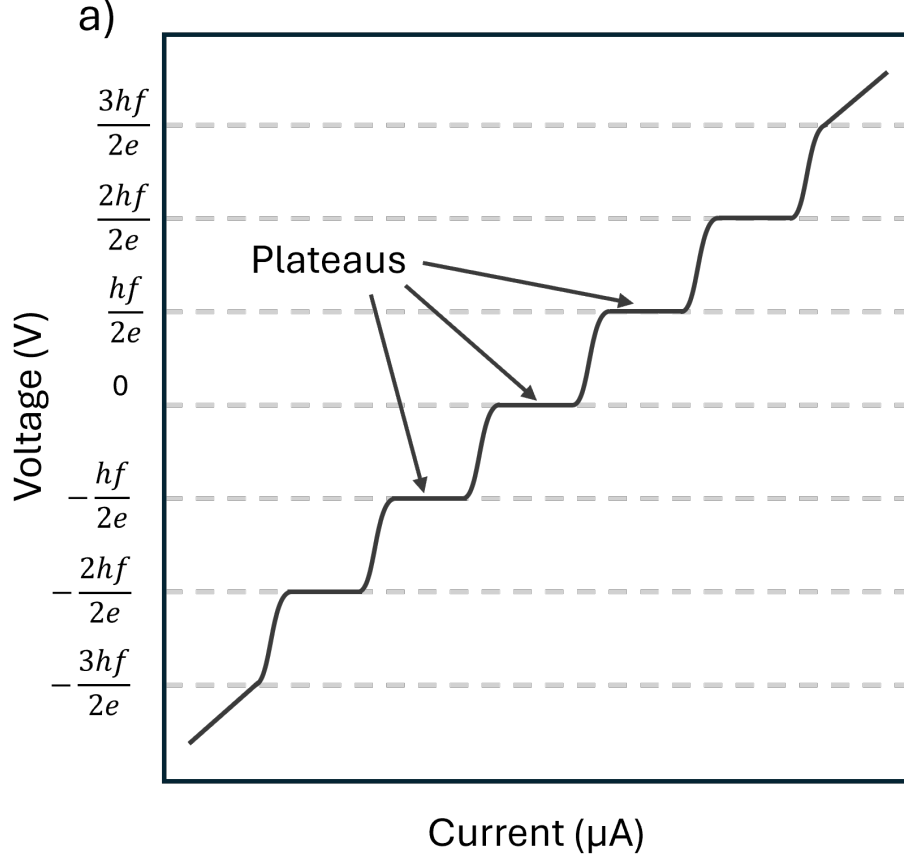
Figure 4.3: Diagram of Shapiro step behavior of a Josephson junction.

An important note about the current-voltage curves: As Tinkham notes in Chapter 6.3.4 of Introduction to Superconductivity (Ref. [1]), the above model assumes that a voltage is applied to the sample and that the current is measured. This is known as a voltage-bias measurement and gives rise to the relatively simple solutions shown above. However, in realistic cases, due to the zero resistance of the superconductor, the finite

resistance in the rest of the circuit sets the current through the Josephson junction, effectively rendering the measurement a current-bias measurement (where current is applied and the voltage is measured). For this reason, current bias measurements are often used to measure Josephson junctions (see the Appendix A.1.2 for a more in-depth discussion of the advantages of current-bias measurements). In the case of current bias measurements, an analytical solution similar to Eq. 4.17 can not be obtained and, therefore, numerical solutions are required. Numerical solutions show that finite DC currents can exist for voltages other than the Shapiro step heights (Refs. [68, 69]), such as between the Shapiro step plateaus, as is shown schematically in Fig. 4.3.

4.1.3   Magnetic Field Dependence of Josephson Junctions

I will now address the contribution of the external magnetic fields on the behavior of the Josephson junction. A brief summary of the derivation I will follow: I will look at the modification of the critical current in a short Josephson junction (relative to the penetration depth) in an applied magnetic field. In order to calculate the critical current, I use the gauge invariant phase difference across the junction. The dependence of the gauge invariant phase difference on the magnetic field can be derived by setting the sum of the order parameter around the loop equal to zero. After this, the order parameter is eliminated from the expression and a relationship between the gauge invariant phase and the magnetic field si obtained. We can imagine a Josephson junction comprising two superconductors separated by a thin non-superconducting material of thickness d, shown in Fig. 4.4. A spatially uniform magnetic field, $\vec{B} = B\hat{y}$, is then applied in the y-direction, perpendicular to the direction of the current flow (in the z-direction).

Due to the applied magnetic field, the phase difference across the junction, which will determine the supercurrent, is now the gauge invariant phase difference γ. Unlike the order parameter, γ will vary across the length of the junction (x-direction) under an applied magnetic field, which we will see later. The gauge invariant phase difference across the
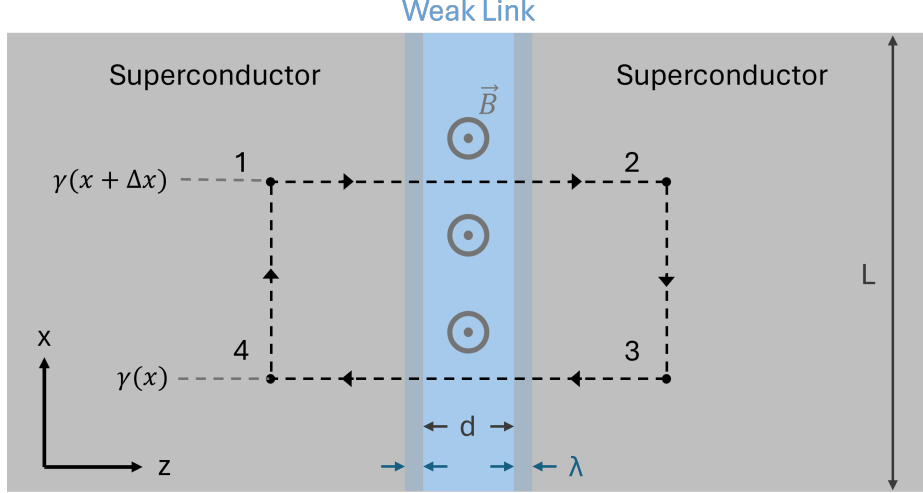
Figure 4.4: Diagram showing the magnetic field incident on a Josephson junction and the closed loop utilized to determine the magnetic field dependence.

Josephson junction is

$$\gamma(x) = \varphi_2 - \varphi_1 - \frac{2\pi}{\Phi_0} \int_1^2 A \cdot dl \tag{4.19}$$

$$-\gamma(x + \Delta x) = \varphi_4 - \varphi_3 - \frac{2\pi}{\Phi_0} \int_3^4 A \cdot dl, \tag{4.20}$$

where A is the vector potential due to the external magnetic field, and the minus sign on γ in the second equation is because the integral is in the opposite direction as the gauge invariant phase difference, which is defined from the left electrode to the right electrode. Φ_0 is the magnetic flux quantum and is defined by $\Phi_0 = \frac{h}{2e}$. According to the London equations, in the electrodes

$$\nabla \varphi = \frac{2\pi}{\Phi_0} (\Lambda J + A). \tag{4.21}$$

However, because we choose to take our path deep within the electrodes $J = 0$. Finally, in order to calculate the phase difference between the superconducting electrodes, we can first consider the phase around the entire loop, which must be single valued mod(2π) as this is the order parameter characterizing the superconductor. This can be represented by

the integral of the phase gradient around the loop

$$\int \nabla \varphi \cdot dl = (\varphi_2 - \varphi_1) + (\varphi_3 - \varphi_2) + (\varphi_4 - \varphi_3) + (\varphi_1 - \varphi_4) = 0. \qquad (4.22)$$

Which can also be written as

$$\int \nabla \varphi \cdot dl = (\varphi_2 - \varphi_1) + \int_2^3 \nabla \varphi \cdot dl + (\varphi_4 - \varphi_3) + \int_4^1 \nabla \varphi \cdot dl = 0. \qquad (4.23)$$

Substituting Eqs. 4.19, 4.20 and 4.21 into Eq. 4.32 the order parameter can be eliminated to yield

$$\gamma(x) + \frac{2\pi}{\Phi_0} \int_1^2 A \cdot dl + \frac{2\pi}{\Phi_0} \int_2^3 A \cdot dl - \gamma(x + \Delta x) + \frac{2\pi}{\Phi_0} \int_3^4 A \cdot dl + \frac{2\pi}{\Phi_0} \int_4^1 A \cdot dl = 0, \ (4.24)$$

which is equivalent to

$$\gamma(x + \Delta x) - \gamma(x) = \frac{2\pi}{\Phi_0} \oint A \cdot dl. \qquad (4.25)$$

Resulting in the equation,

$$\gamma(x + \Delta x) - \gamma(x) = \frac{2\pi\Phi}{\Phi_0}, \qquad (4.26)$$

where the flux can be represented by the area of penetration of the magnetic field $\Phi = BA$, with $A = (d + 2\lambda)\Delta x$. The penetration depth is incorporated in the thickness of the junction as the magnetic field will also penetrate this region. This results in the equation

$$\frac{\gamma(x + \Delta x) - \gamma(x)}{\Delta x} = \frac{2\pi}{\Phi_0} B(d + 2\lambda), \qquad (4.27)$$

which as Δx goes to 0 becomes

$$\frac{d\gamma}{dx} = \frac{2\pi}{\Phi_0} B(d + 2\lambda). \qquad (4.28)$$

Integrating this equation yields the gauge invariant phase difference as a function of x

$$\gamma(x) = \frac{2\pi}{\Phi_0} B(d + 2\lambda)x + \gamma_0. \tag{4.29}$$

Therefore, the current density in the junction will have a spatial dependence according to

$$J = J_0 \sin\left(\frac{2\pi}{\Phi_0} B(d + 2\lambda)x + \gamma_0\right), \tag{4.30}$$

which, under the assumption of a homogeneous critical current J_0, can be integrated over the length of the junction L to get the total current flowing through the junction

$$I = I_0 \sin(\gamma_0) \frac{\sin\left(\frac{\pi\Phi}{\Phi_0}\right)}{\frac{\pi\Phi}{\Phi_0}}, \tag{4.31}$$

where $\Phi = B(d + 2\lambda)L$. The current has a maximum value at $\gamma_0 = \pi/2$, resulting in the usual Fraunhofer diffraction pattern for the maximum current, shown in Fig. 4.5, given by

$$I_{max} = I_0 \left|\frac{\sin\left(\frac{\pi\Phi}{\Phi_0}\right)}{\frac{\pi\Phi}{\Phi_0}}\right|. \tag{4.32}$$

It should be noted that this calculation was done neglecting self-field effects, which become significant when $L > \lambda_J$, where $\lambda_J = \sqrt{\frac{\Phi_0}{2\pi\mu_0(d+2\lambda)J_c}}$, and is defined as the Josephson penetration depth.
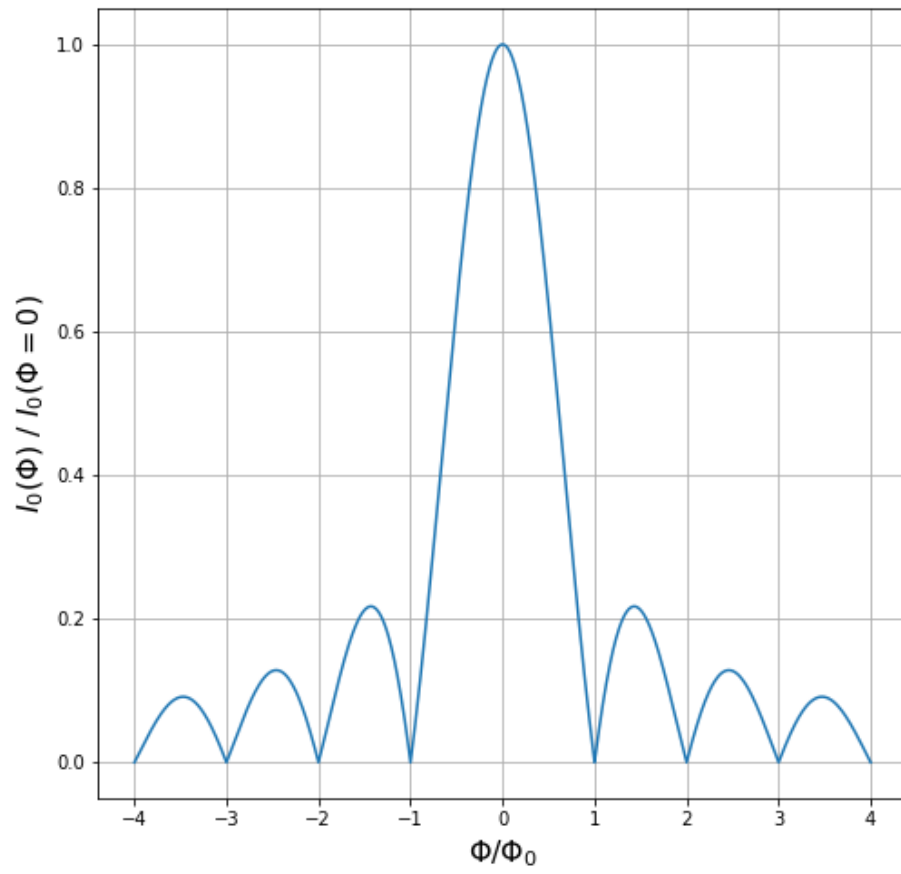
Figure 4.5: Plot of the Fraunhofer pattern showing the normalized critical current as a function of the magnetic flux.

Chapter 5

FeTeSe-Al Josephson Junction

We fabricated devices based on the interface between Al and $FeTe_{0.55}Se_{0.45}$, a material which provides a compelling platform for investigating phenomena associated with unconventional superconductivity. In this system, Josephson effects were observed, which deviate from the typical behavior of Josephson junctions shown in Section 4.1. For each of the unusual features seen, I will present the data step by step to highlight the atypical features demonstrated. For each of the unusual phenomena, I will discuss potential mechanisms driving the behavior. Ultimately, we find that the Josephson effects present in this system may arise from a phase slip line induced in $FeTe_{0.55}Se_{0.45}$ instead of the expected Josephson junctions at the Al-$FeTe_{0.55}Se_{0.45}$ interface.

5.1 Fabrication and Measurements

5.1.1 Fabrication

Before diving into the results, I will give a brief description of the fabrication and measurements of our devices, shown schematically in Fig. 5.1. In order to produce flakes of $FeTe_{0.55}Se_{0.45}$, which we can process using standard chip processing techniques, we first take bulk crystals of $FeTe_{0.55}Se_{0.45}$ and exfoliate them by the scotch tape method. The
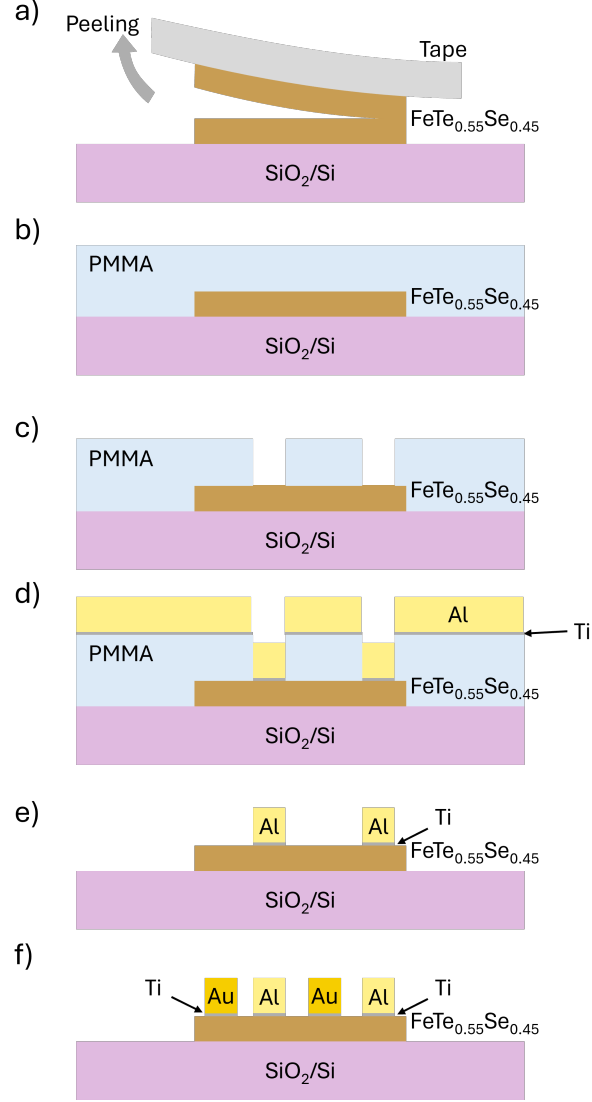
Figure 5.1: a-f) Overview of the fabrication process of the Al-FeTeSe devices. First exfoliation of the FeTeSe was performed (a), followed by spinning of an e-beam resist (b). A device pattern was then written into the e-beam resist and developed (c). Titanium/Aluminum 5 nm/50 nm was deposited by magnetron sputtering (d), and the excess Al was removed during the liftoff stage (e). This process was then repeated for Ti/Au 5 nm/ 50 nm, using electron beam deposition instead of sputtering.

adhesive force of the scotch tape is stronger than the weak inter-layer vdW force holding the 2D layers of $FeTe_{0.55}Se_{0.45}$ together. As a result, when the tape is peeled apart, the $FeTe_{0.55}Se_{0.45}$ crystal are cleaved. This tape is then applied to a clean substrate composed of conductive p-doped silicon capped with 285 nm SiO_2. Moderate pressure was applied and the sample was given approximately 5 minutes to ensure the $FeTe_{0.55}Se_{0.45}$ interfaces

the substrate well. After this, the tape is peeled back from the substrate and flakes of $FeTe_{0.55}Se_{0.45}$ will be cleaved by the adhesive force of the substrate and the tape (Fig. 5.1 a), leaving flakes of $FeTe_{0.55}Se_{0.45}$ approximately 1-10 μm wide and 10-100 nm thick. After flakes have been produced, electron beam resist (PMMA 950A4) can be spun onto the substrate and baked at 180 °C for 2 mins (Fig. 5.1b). Alignment marks are then written by electron beam lithography, and subsequently developed in a 3:1 mixture of isopropanol (IPA):methyl isobutyl ketone (MIBK). Optical images of the sample and alignment marks are then used to locate the position of the flake on the chip exactly, and then the intended electrodes can be patterned by electron beam lithography as well (Fig. 5.1c). In the case of our devices, there were two lithography and deposition steps. Aluminum electrodes were deposited by Magnetron Sputtering and Au electrodes were deposited by Electron Beam Deposition, where, in both cases, a thin adhesion layer of ~5 nm Ti was used (Fig. 5.1d). See Appendix A.5 for standard operating procedures, maintenance, and modifications to the Magnetron Sputtering system and the Electron Beam Deposition system. After metal deposition, the PMMA is removed by acetone, and therefore the metal on the surface of the PMMA is removed as well (Fig. 5.1e). This process is repeated for Au electrode (Fig. 5.1f). The resulting device is shown schematically in Fig. 5.2 and the device image is shown in Fig. 5.3. The area of the electrode-FeTeSe interface is $\sim 1.8 ~\mu m^2$.

5.1.2 Measurement Procedures

After device fabrication, the substrate was affixed to a small sample holder using PMMA glue, which was then affixed to a larger sample holder by vacuum grease. At this point, the electrodes on the device were connected to the electrodes on the sample holder by wire bonding (See Appendix A.3 for details of wire bonding). One of the electrodes is also connected to the bonding pad corresponding to the RF lines. This allows measurement of the samples using a Lock-in 4-terminal current-bias measurement scheme (shown in Fig. 5.4), while irradiating the sample with RF photons using Rhode and Schwarz SMB100A
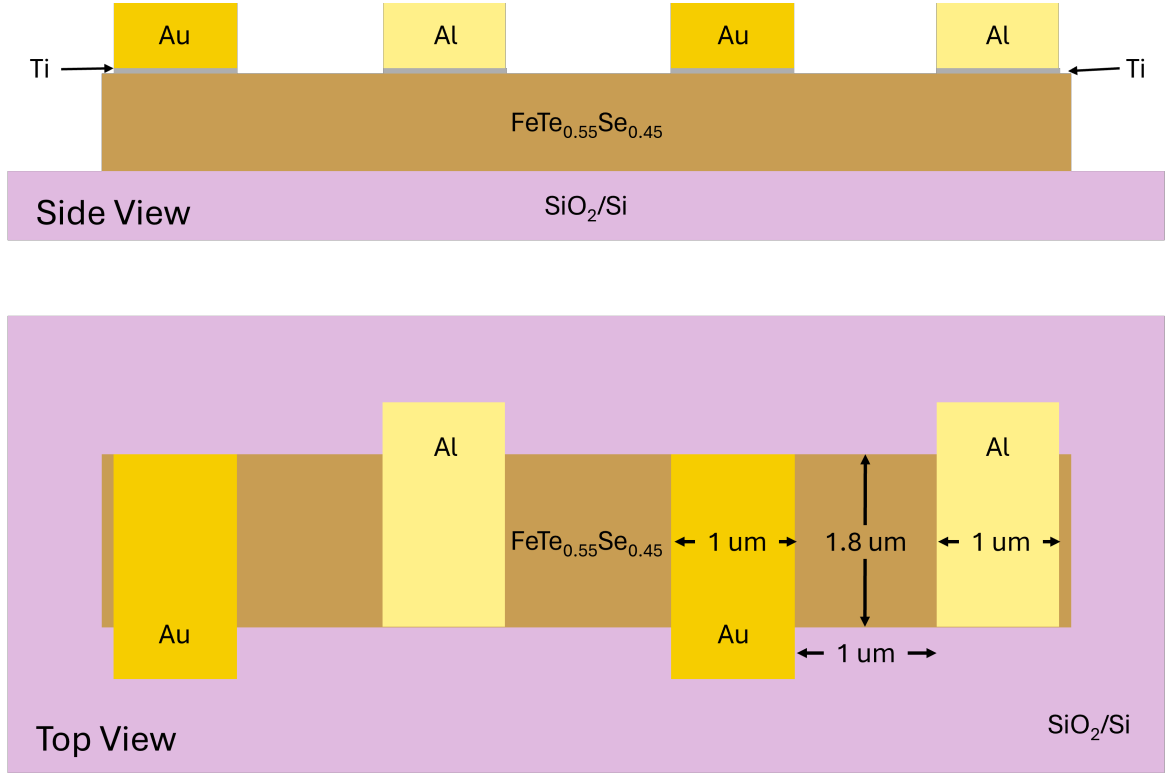
Figure 5.2: Schematic and dimensions of FeTeSe device showing the side view and top view. The FeTeSe flake is ∼1.8 μm wide and the Al electrode is ∼1.0 μm wide. The intended device was at the Al-FeTeSe interface, which has an area of 1.8 μm^2, however we will see that other regions in the device can potentially contribute as well.

microwave signal generator. Frequency ranging from 100 MHz to 7 GHz and an applied RF power ranging from -70 dBm to 5 dBm were used throughout the measurements. The real incident RF power on the device was likely reduced by greater than 10 dB due to attenuators in the lines. The specifics of 4-terminal measurements are discussed in Appendix A.1.2. The four terminal measurement scheme isolates the voltage drop across the Al-FeTe$_{0.55}$Se$_{0.45}$ interface (nominally including a Ti layer) from the voltage drop across the lines and other interfaces in the system (voltage drops across the small strips of Al and FeTe$_{0.55}$Se$_{0.45}$ comprising the electrodes could still be measured). After wire bonding, the samples are then loaded into either a Leiden Dilution refrigerator or an Oxford Instruments Dilution Refrigerator, which were utilized to achieve temperatures of ∼50 mK and ∼25 mK, respectively. See Appendix A.1.3 for details of DC and RF wiring.
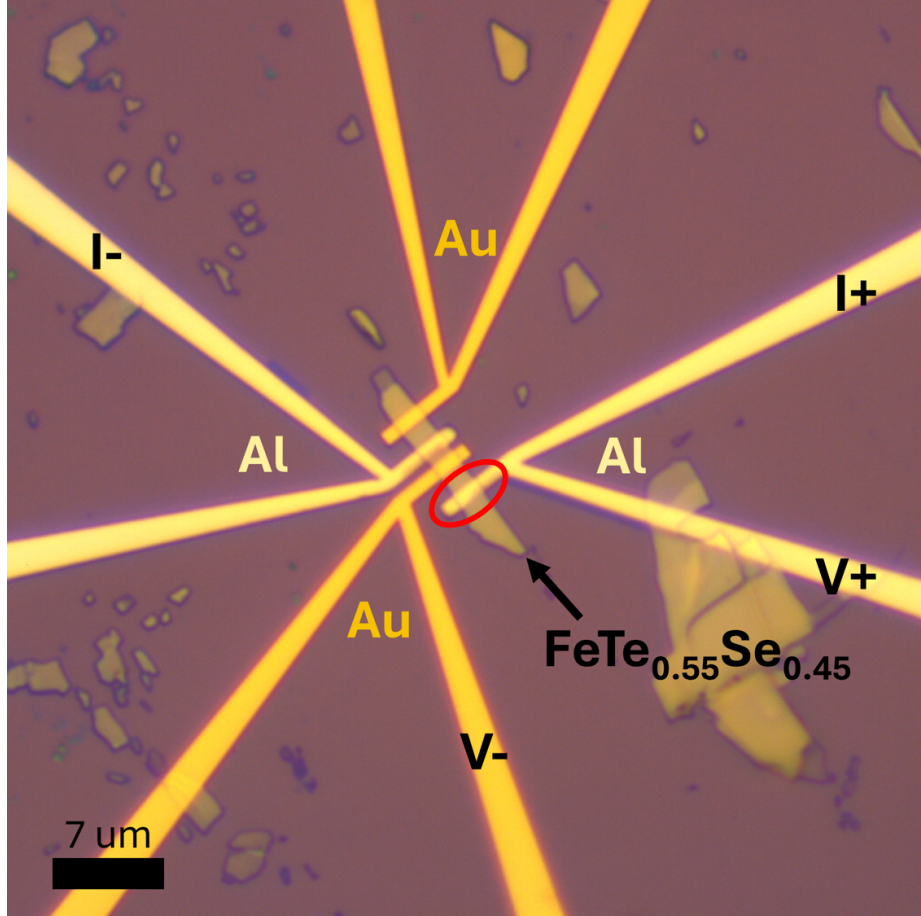
Figure 5.3: Optical image of the FeTeSe device structure showing the electrodes used for the four-terminal measurement. This four-terminal measurement should isolate the voltage drop across the Al-FeTeSe interface, and a small amount of the FeTeSe and Al materials as well, which we will see can potentially have a significant impact. This measured region is circled in red.
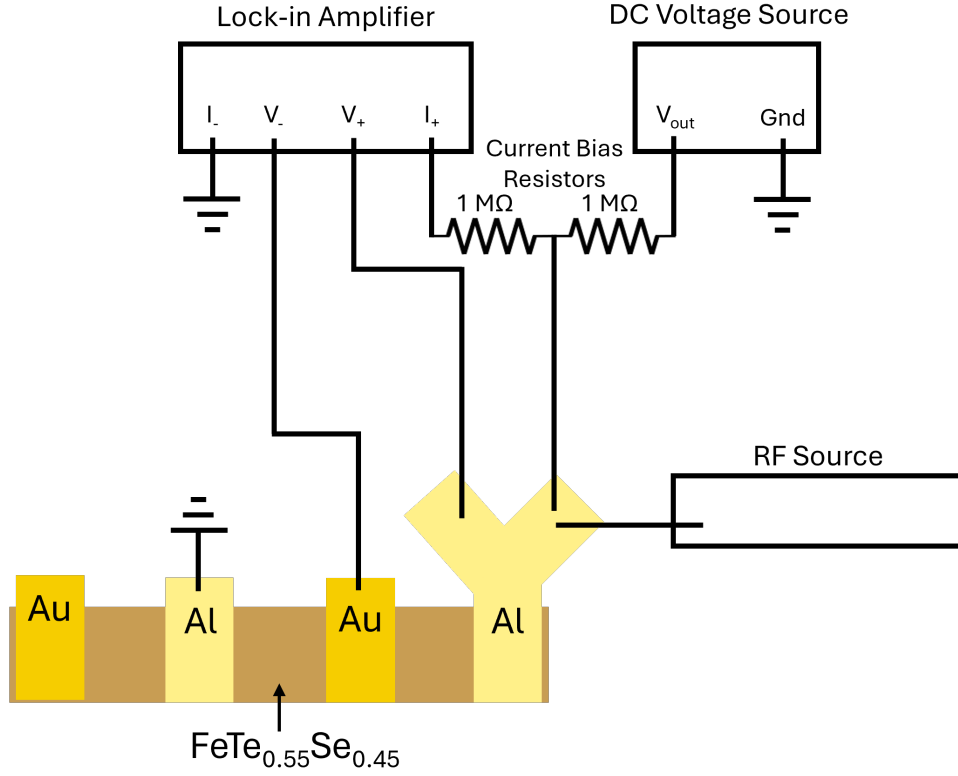
Figure 5.4: Circuit schematic of the measurement technique used to investigate the device; the 4-terminal current-bias measurement with a DC voltage source and an RF source. The lock in amplifier produced a low frequency AC voltage excitation which we convert into a current excitation I_+ using a bias resistor. The lock-in then measures the differential resistance $\frac{dV}{dI}$ in Ohms using a phase locked technique. This resistance was then measured as a function of DC current using a voltage source and a bias resistor, and as a function of RF frequency and power (using a SMB100A microwave signal generator). See Appendix A.1.2 for a more detailed discussion of the measurement methods.

5.2 Inner and outer junction effect

When measuring a Josephson Junction, the differential resistance (dV/dI) vs current measurement resembles measurements of a superconducting flake, but with a significantly reduced critical current. We therefore expect to measure zero resistance at zero bias current and a resistive state emerging at higher currents. We measured this phenomenon in our Al-FeTeSe Josephson junction at a base temperature of $\sim$50 mK, shown in Fig. 5.5a.
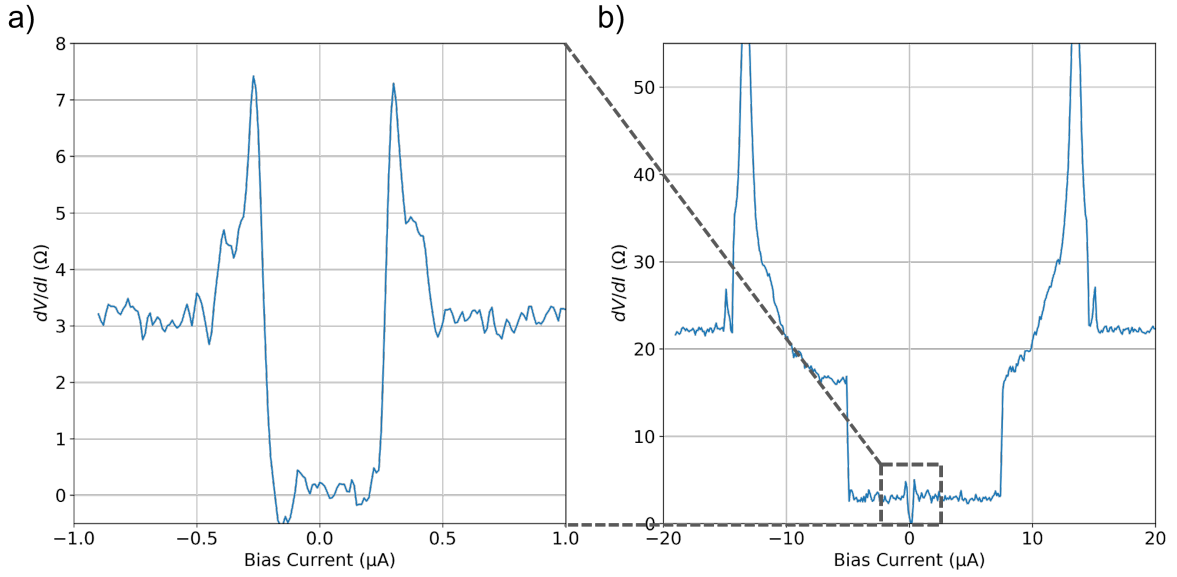
Figure 5.5: a,b) Initial $\frac{dV}{dI}$ vs I measurements of the FeTeSe device. An initial jump from a 0 Ω state to a 3 Ω resistance state occurs around 0.25 μA (a). Two other distinct jumps in resistance can be seen at 6 μA and 13 μA. We will later find Josephson effects emerginf for both the jump at 0.25 μA (the inner junction) and at 6 μA (the outer junction). The resistance jump at 13 μA likely corresponds to the bulk Al electrode, which will be shown later.

We can clearly see there is a nearly zero resistance state around zero bias current, and a critical current of approximately 0.25 μA, beyond which the differential resistance jumps to approximately 3 Ω (Fig. 5.5a). Expanding the range of our DC current sweep to 20 μA reveals that there is another jump in resistance to approximately 16 Ω occurring at a current of 7.5 μA (Fig. 5.5b). This is typical for Josephson junctions, as the electrodes

also have a critical current beyond which there will be a jump in the differential resistance. We will see later see, however, that other effects can also give rise to multiple jumps in resistance. There is a large jump in the resistance around 13 μA likely arising from the transition to the normal state for the aluminum electrode, which will be shown later in Section 5.4.

Next, I will investigate the AC Josephson effects in our device, namely the Shapiro steps. As demonstrated in Section 4.1.2, when discussing the Josephson equations, Shapiro steps will emerge at voltages of $V = \frac{hf}{2e}$ as the RF power is increased. In the measurements of dV/dI, the jumps in between the Shapiro steps will appear as spikes in the differential resistance, which can be clearly seen for the sweep at 0.5 GHz under -54 dBm RF power (Fig. 5.6). It should be noted that the RF power throughout this study is the applied RF power from the RF generator, not the incident RF power on the device. It likely represents an overestimate of the RF power arriving at the device.

The dV/dI vs I curve can then be numerically integrated in order to obtain the voltage vs current curve according to Eq. 5.1. This has advantages over taking a simple DC voltage vs current sweep, as the noise reduction advantages of a Lock-in amplifier are retained, which I discuss in Appendix A.1.1. It should be noted that the integrated voltage is set to zero at zero current after the integration of dV/dI.

$$V(I_j) = \sum_{i=0}^{j} \frac{dV(I_i)}{dI} \Delta I \tag{5.1}$$

The resulting Shapiro steps approximately follow the expected voltage dependence of $V = \frac{hf}{2e}$, as can be seen from Fig. 5.7. In this figure, the inner plateau is the superconducting state, and the first Shapiro step is visible at ± 0.3 μA. The slight deviations from the ideal Shapiro step height could be due to finite temperature of the junction in what is often referred to as 'melting' of the Shapiro steps, see Refs. [70–72]. Microwaves can have a significant heating effect at mK temperatures. For instance, when a RF power of ~5 dBm is applied, heating from ~50 mK to ~75 mK was measured by the mixing chamber
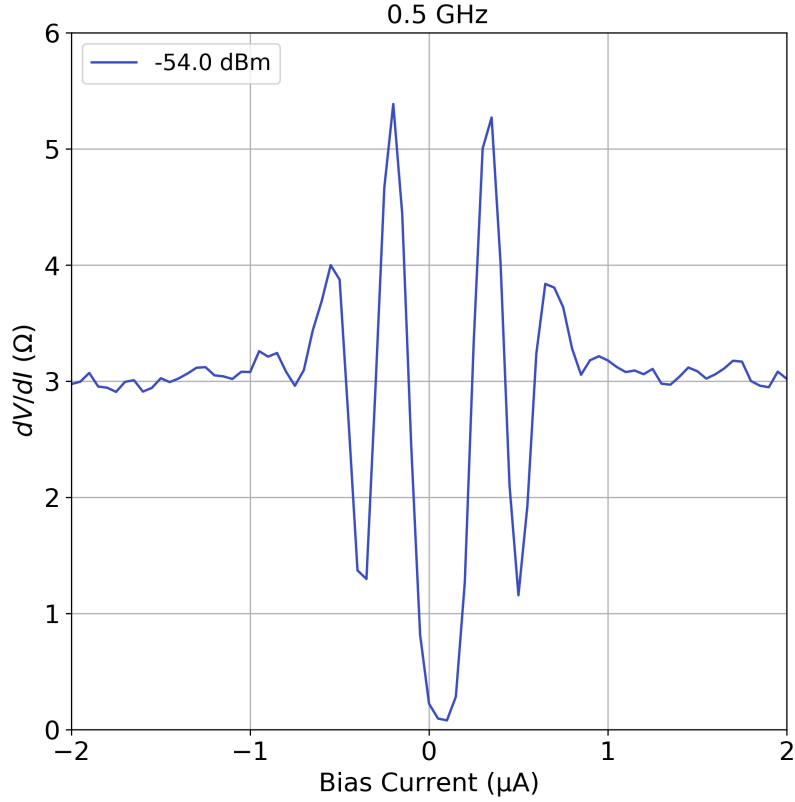
Figure 5.6: $\frac{dV}{dI}$ vs I measurements at a frequency of 0.5 GHz and a RF power of -54 dBm. This RF power corresponds to the output of the RF generator, not the RF power incident on the device. At this power, there are clear oscillations of the differential resistance. The peaks correspond to the jump between Shapiro steps and the minima correspond to the Shapiro step plateaus.

thermometer.

Next, power-dependent measurements of the Shapiro steps were performed. In order to visualize the evolution of the Shapiro steps most clearly, dV/dI vs I can be plotted, where the dark regions with low resistance indicate plateaus in the Shapiro step diagram, and the high resistance peaks indicate the jumps between these steps (Fig. 5.8). Throughout this dissertation, we will refer to this as Shapiro mapping or RF power mapping. The black dashed line shows the position of the line cut shown in Fig. 5.6 in the larger power-dependent map shown in Fig. 5.8.

One unusual thing we can notice from the map of dV/dI vs I curves is multiple
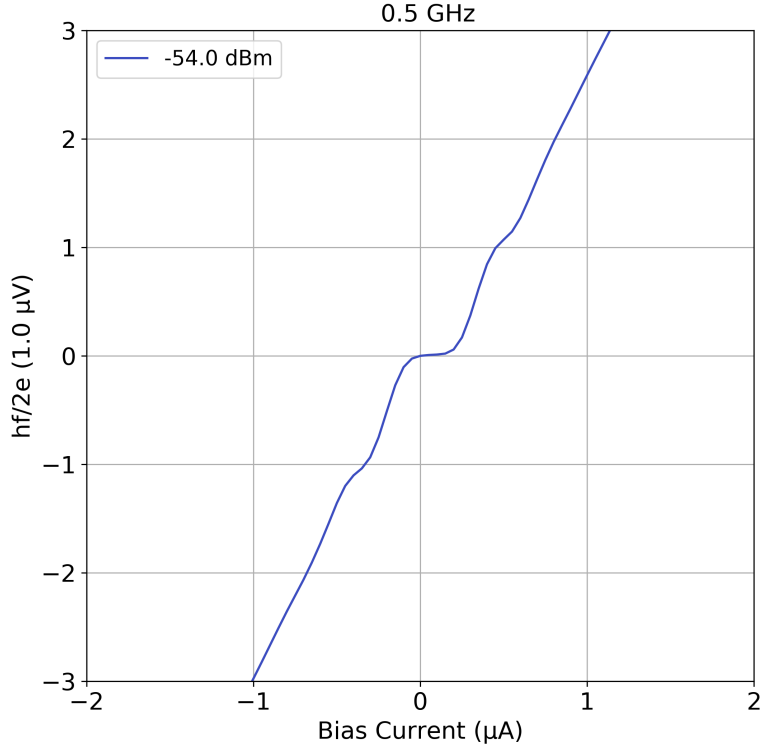
Figure 5.7: The result of numerically integrating Fig. 5.6 to reveal the voltage as a function of current and the associated Shapiro steps. The voltage is shown in units of the characteristic voltage step $V = hf/2e$, which for 0.5 GHz is 1.0 μV.

peaks in the differential resistance near the closure of the second, larger jump in resistance, occurring from approximately -35 dBm to -25 dBm. Interestingly, when the RF frequency is increased to 3.97 GHz, we see these fluctuations become more prominent, resembling Shapiro steps in a Josephson junction (Fig. 5.9). To clearly distinguish these two Josephson phenomena, I will refer to the Josephson effects with a small critical current of ∼0.25 μA as the inner junction and the Josephson effects with the larger critical current of ∼6 μA as the outer junction, which have been highlighted in Fig. 5.9. Additionally, we can see that the peaks resembling Shapiro steps in the outer junction appear to be cut off by an envelope characterizing the transition to the normal non-superconducting state of the junction. This behavior is in contrast to the inner junction 5.8, which demonstrates a more typical Shapiro step map.
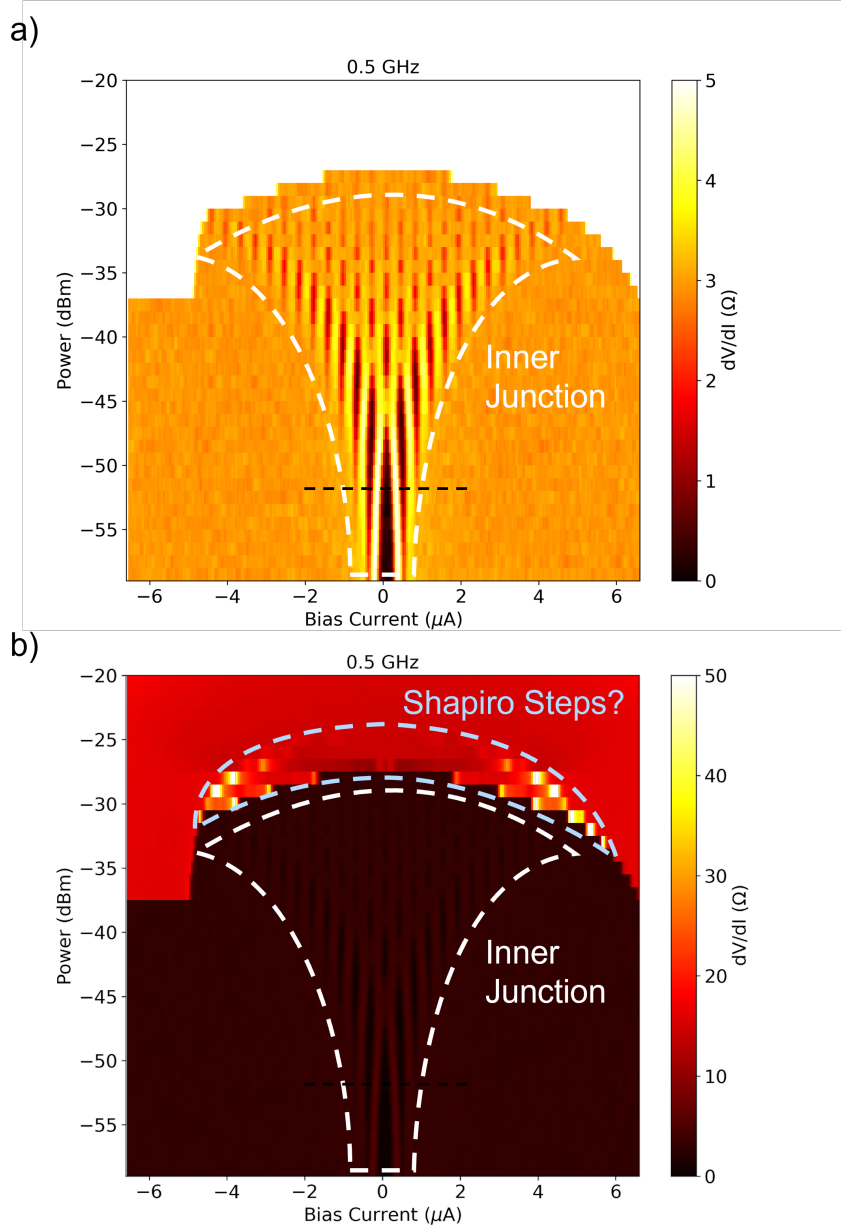
Figure 5.8: a,b) Map of $\frac{dV}{dI}$ vs I vs RF power, revealing the Bessel function-like dependence of the Shapiro steps (a). See Refs. [68, 73] for more details on the dependence of the Shapiro steps in the current-bias, which follow a Bessel function-like oscillation. When the scale is modified, additional features are also visible in the range of -35 dBm to -25 dBm (b), which resemble Shapiro steps (in the outer junction), but are not clearly resolvable in this sweep.

Before moving on, I will touch on the asymmetry for positive current and negative currents visible in the outer junction in Figs. 5.5,5.9. In these measurements, the current is swept from negative currents to positive current, therefore, first the Josephson junction will
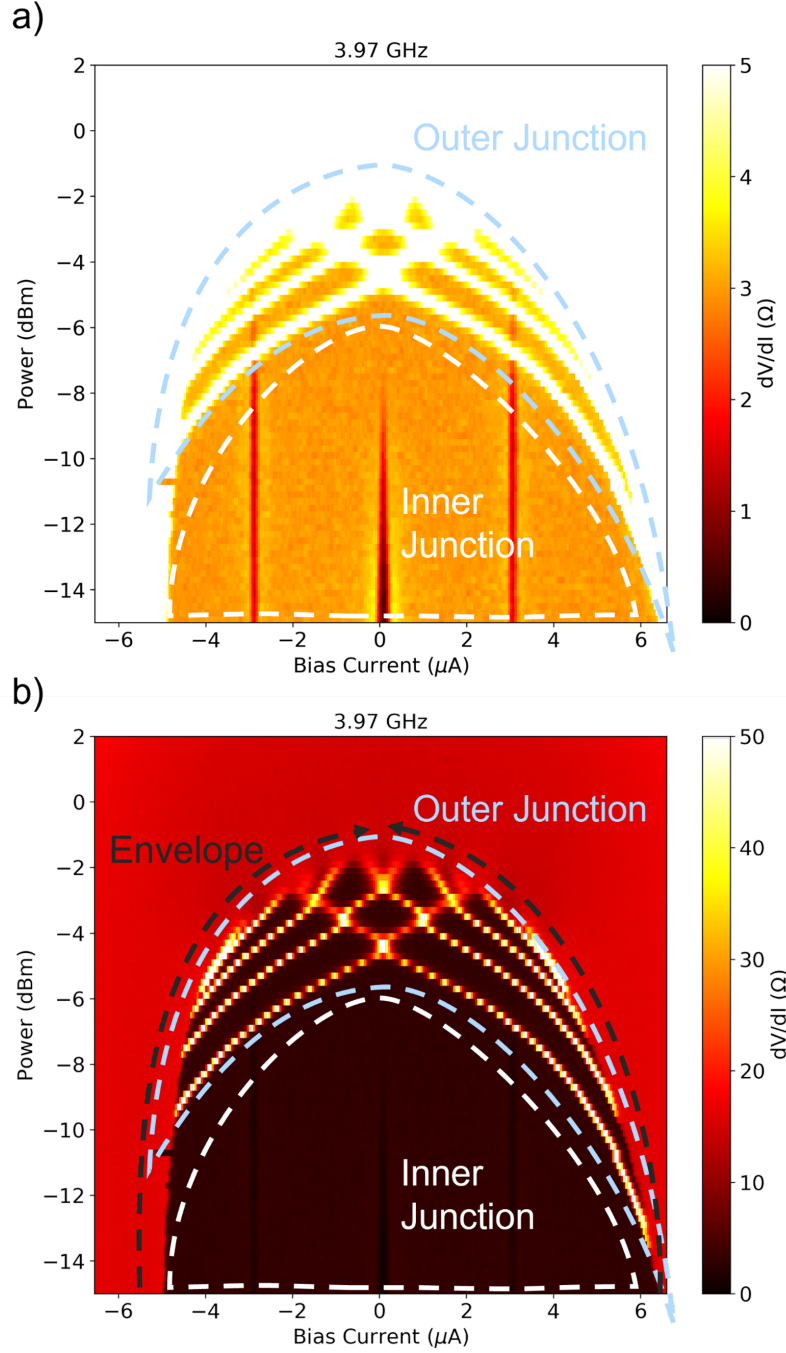
Figure 5.9: a,b) Map of $\frac{dV}{dI}$ vs I vs RF power at 3.97 GHz. The minimum in the $\frac{dV}{dI}$ is still clearly visible for the inner junction (a). However, when the scale is adjusted, additional peaks are visible, which strongly resemble a Shapiro step map for the outer junction (b).

transition from the normal state to the superconducting state at ~5 μA. This is known as the retrapping current of the Josephson junction and is typically smaller than the critical

current of the Josephson junction, where the junction transitions from the superconducting state to the normal state. In the outer junction, this happens at positive currents ~ 6 μA. The difference between the retrapping current and the critical current is determined by the degree of damping of the phase oscillations in the junction. This can be described by modeling a Josephson junction shunted by a resistance and a capacitance, as is described in Refs. [1, 68, 74]. The consequence of this model is that for highly damped Josephson junctions (small capacitance), the critical and retrapping currents are the same, and for minimally damped Josephson junctions (large capacitance), the retrapping current can be reduced to very small currents approaching zero current flow. For more detailed descriptions of the topic, I suggest Chapter 6.3 of Tinkham (Ref. [1]). Our outer junction is therefore in an intermediate state between these two extremes, as are many Josephson junctions without a large tunneling barrier (Refs. [75, 76]).

Next, to investigate the apparent Shapiro steps in the outer junction, the dV/dI vs I curves can be integrated to reveal the step height of the Shapiro steps (Fig. 5.10). Because there has already been an initial jump in dV/dI from the inner junction, we can see that the plateaus of the Shapiro step behavior are not flat, and therefore, the exact height of the voltage jump between each step is not easily apparent. To solve this, the resistance after the initial jump (when the inner junction is in the resistive state) can be subtracted from the dV/dI vs I curve before integration. For this purpose, I used a value of 3 Ω, which is approximately the resistance after the inner junction transitions to the normal state. After this subtraction, the voltage jumps match the expected Shapiro step height (Fig. 5.11).

The existence of two Josephson junction-like effects in a single device begs the question: What is giving rise to these two effects, and what information can we glean from the differences between the behavior of the inner junction and the outer junction? We will next give a few likely explanations, which will be refined as we investigate the other unusual phenomena in subsequent sections.
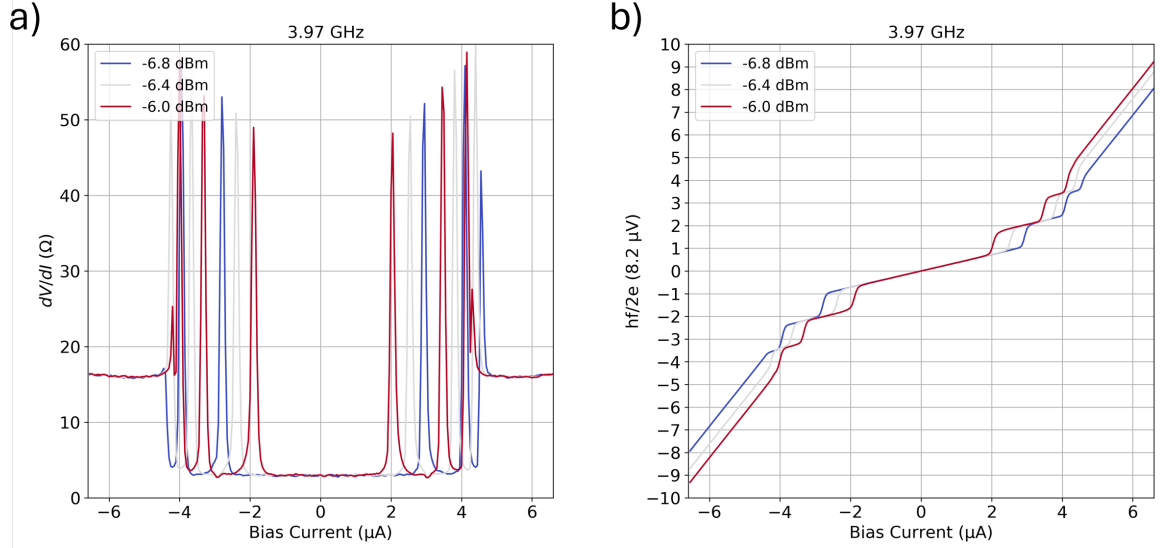
Figure 5.10: a) Linear cuts of the $\frac{dV}{dI}$ vs I vs RF power map at 3.97 GHz. b) The I-V curves resulting from numerically integrating the linear cuts in (a). The Shapiro step height can not be clearly resolved due to the finite slope where the plateaus in voltage would normally be. This arises from the 3 Ω background from the normal state resistance of the inner junction.

5.2.1 Discussion of Inner/Outer Junction

There are a few distinct differences between the Josephson effects observed in our Josephson junctions and the typical case described in Section 4.1, which may provide hints as to what is causing the inner junction and outer junction behavior. Specifically, the energy scales of the Josephson coupling and the shape of the envelope of the Josephson effects.

The Ambegaokar-Baratoff relation (Ref. [60]) is a useful and widely applicable formula for physicists investigating Josephson junctions, specifically as a probe of the energy scale of the Josephson junction. Taking advantage of the inverse scaling of the critical current (I_c) and the normal state resistance (R_n) of the junction with the area (A) and length (L) of a Josephson junction (Ref. [1]),

$$I_c \propto A/L, \quad R_n \propto L/A \qquad (5.2)$$
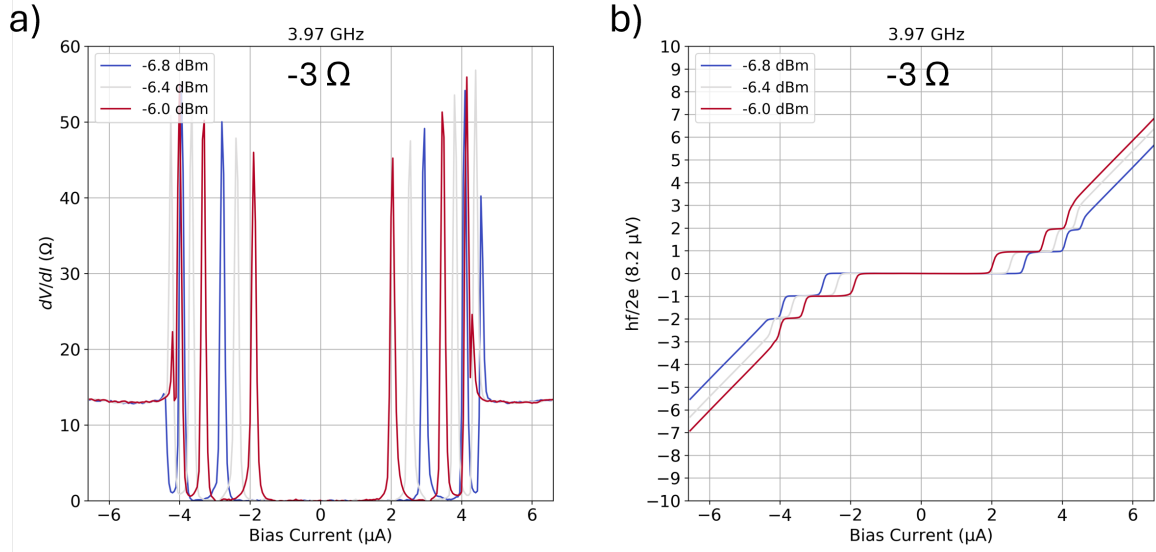
Figure 5.11:   a) Linear cuts of the $\frac{dV}{dI}$ vs I vs RF power map at 3.97 GHz minus the 3 Ω background from the normal state of the inner junction. b) The I-V curves resulting from numerically integrating the linear cuts in (a), revealing quantized Shapiro steps at the expected voltages of 8.2 μV. This suggests there are indeed Josephson effects for both the inner junction and outer junction.

an invariant value can be defined for junctions.

$$I_c R_n = (\pi \Delta / 2e) \tanh(\Delta / 2kT), \tag{5.3}$$

where Δ is the superconducting gap and T is the temperature. This relation is generally true for S-I-S Josephson tunnel junctions and for S-N-S metallic Josephson junctions near T_c. This turns out to be a useful general result for determining the effective gap induced in the weak link of the Josephson junction, as this will often differ from the value of the bulk band gap for metallic weak links, due to the reduced transparency. Alternatively, the junction transparency α can be extracted using the formulation

$$I_c R_n = (\alpha \Delta / 2e) tanh(\Delta / 2kT). \tag{5.4}$$

See section 6.2 of Tinkham for a more detailed description of barrier transparency

(Ref. [1]). In our system we have two different superconductors with bulk superconducting gaps of $\Delta_{FTS} \approx 1.1 - 2.1\ meV$ for FeTe$_{0.55}$Se$_{0.45}$ (Ref. [54]) and $\Delta_{Al} \approx 0.2\ meV$ for 30-nm-thick films of Al (Ref. [77]). Because this system is comprised of dissimilar superconducting electrodes and the cause of the Josephson behavior is not known, it will be easier to compare the apparent gap based on the $I_c R_n$ according to Eq. 5.3 to the bulk superconducting gaps, than it would be to extract a meaningful transparency. In the following, I will assume that we are sufficiently below T$_c$ such that the $tanh(\Delta/2kT) = 1$. This assumption is reasonable as the measurement temperature of 50 mK is far below the T$_c$ of Al (~ 1 K) and FeTeSe (~ 14 K). For the inner junction, the normal state resistance is $\sim 3\ \Omega$ and the critical current is $\sim 0.25\ \mu$A, therefore, based on Eq. 5.3, the apparent gap is $\sim 0.5\ \mu$eV. This is obviously much smaller than either of the superconducting gaps of the bulk electrodes, which could potentially suggest that the transparency of the Josephson junction is very low, or that there is some other phenomenon giving rise to this effect. In comparison, the normal state resistance of the outer junction is $\sim 16\ \Omega$, and the critical current is $\sim 7\ \mu$A, resulting in an apparent gap of $\sim 71\mu$eV. This is in the typical range of an Al Josephson junction, and would correspond to a relatively transparent junction. Low junction transparency can arise from junctions with thickness longer than the coherence length of the superconductor ξ. However, in our device, the inner junction with the smaller normal state resistance ($\propto$ thickness) is seemingly less coherent than the outer junction with the larger normal state resistance ($\propto$ thickness). Therefore, it seems likely that there may be another mechanism at work here.

The second contrasting feature between the inner junction and outer junction is the envelope of the Shapiro step interference pattern. For the inner junction, the interference has a typical Bessel function shape, and the envelope of the interference pattern expands as the power is increased (Fig. 5.8). In contrast, for the outer junction, the interference pattern arises within an envelope which decreases with applied power (Fig. 5.9), similar to the critical current in a superconducting strip. Beyond this envelope, there do not appear

to be any quantum coherent effects giving rise to interference.
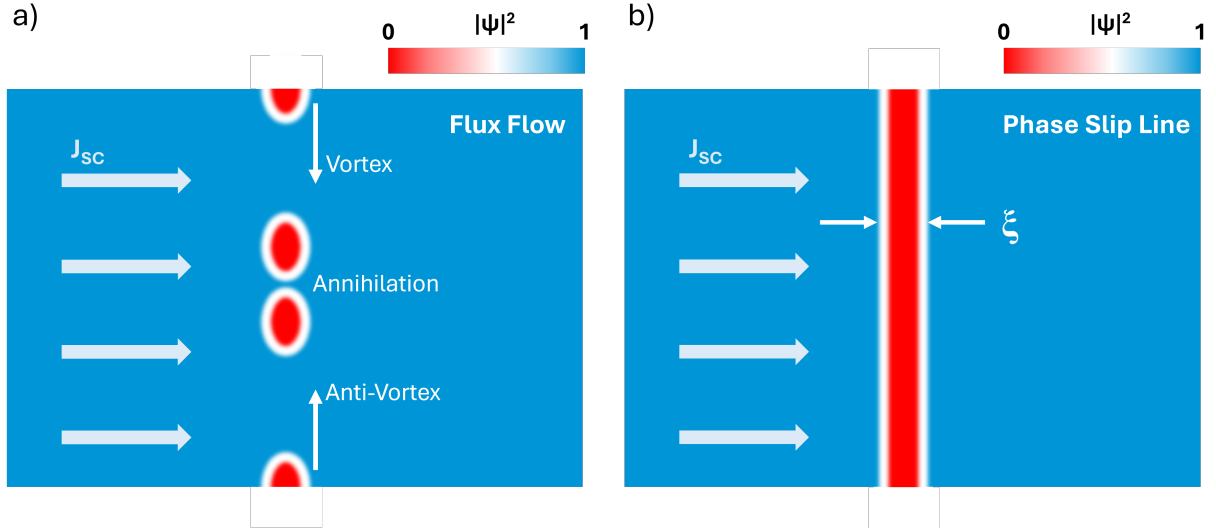
Figure 5.12: a) Schematic of vortex flux flow, whereby vortices and antivortices nucleate at weak points in the superconductor, and flow perpendicular to the supercurrent by the Magnus effect. The vortex contains quasiparticles states, which, when moved, will result in finite dissipation and therefore a finite resistance/voltage across the device. b) Schematic of a phase slip line, whereby the vortices moving in the wake of the following vortex become sufficiently deformed such that they are described by a normal dissipating line throughout the device. See Refs. [78, 79] for a discussion of phase slip lines and Refs. [80–82] for a discussion of the kinematic vortices in phase slip lines.

There is a quantum phenomenon in superconductors that can potentially describe both of these observations: flux flow resistance and phase slip lines. In Type II superconductors, where $\xi < \lambda$ and the superconductor width $w > \xi$, λ, the onset of finite resistance can occur due to the spontaneous generation of vortices which flow perpendicular to the supercurrent. This is a two-step process, where first, above a lower critical current, vortex/antivortex pairs begin to nucleate at the edges of the superconductor and flow towards the center of the superconductor, where they annihilate (Refs. [78, 79]). In vortices, due to the reduction of the superconducting gap over the length scale of ξ, there will be quasiparticle states (CdGM states, Ref. [52]) which move with the vortex and cause finite dissipation (see the Bardeen-Stephen Model for a simplified treatment in Ref. [83]), resulting in the onset of a small resistance state. This regime is referred to as the flux-flow regime and is

shown schematically in Fig. 5.12. Because the order parameter is suppressed at the cores of the vortices, there will be a 'wake' of suppressed superconductivity behind the vortex (Ref. [84]). As the current is increased and the vortex flows faster, the vortices will be attracted to the wake of the previous vortex (Refs. [84, 85]), because there is a smaller energetic cost to form a vortex where the superconductivity is weaker. Eventually, a second transition to the resistive state will take place when the vortex states become sufficiently deformed into a phase slip line (PSL) (Fig. 5.12). The PSL is a line of suppressed superconductivity which can be approximated as a kinematic vortex (behavior in between that of an Abrikosov vortex and a Josephson vortex) with an arbitrarily large velocity (see Refs. [78, 79] for a discussion of phase slip lines and Refs. [80–82] for a discussion of the kinematic vortices in phase slip lines). In the phase slip state (Ref. [85]), AC Josephson effects with quantized Shapiro steps have been demonstrated previously. Further, Tran et al. demonstrated multiple Josephson effects in a device consisting of the 2D superconductor $NbSe_2$ (Ref. [86]), which was revealed to occur due to the generation of phase slip lines. The phase slip line mechanism is further supported by the Shapiro steps of the outer junction, which emerge from the envelope that defines the transition to the normal, non-superconducting state. This is consistent with a superconducting-normal transition for a phase slip line, and is in contrast to typical Josephson junctions, which do not have an envelope encompassing the Josephson effects and expand with a Bessel function dependence much like the inner junction.

If we reasonably assume that the flux flow/phase slip line description indeed governs the effects in our device, then we should clarify the difference between steps in the V vs I curves characteristic of Shaprio steps, and the steps in the resistance ($\frac{dV}{dI}$) vs I curves characteristic of phase slip lines. Similar to the case of phase slip centers (the 1D analog to a phase slip line), the generation of n additional phase slip lines would result in a total differential resistance which is n times the differential resistance of a single phase slip line (see Ref. [87]). This phenomenon was demonstrated in phase slip centers in tin whiskers,

61
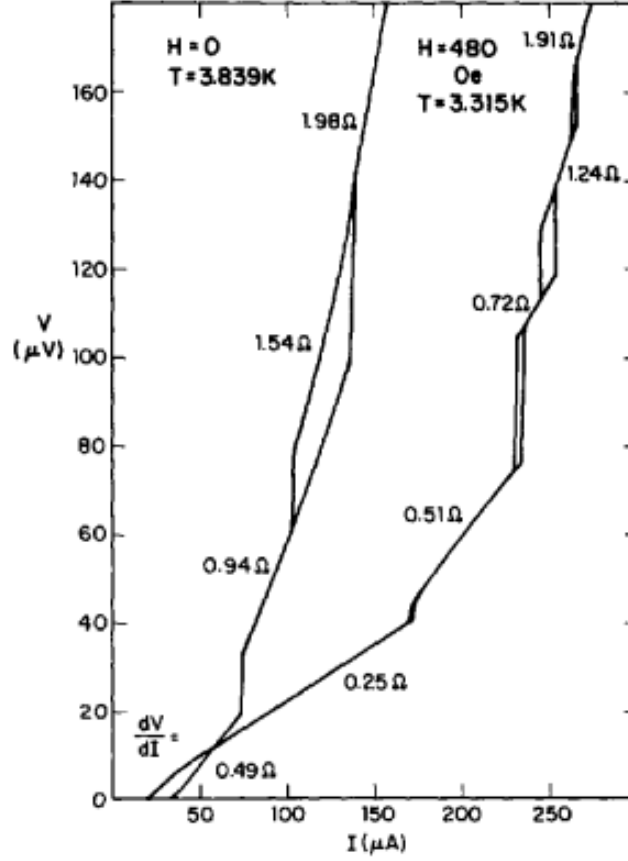
Figure 5.13: Diagram showing the voltage vs current curves arising due to the successive nucleation of phase slip lines, adapted from Ref. [87]. Specifically, when the current is increased, additional phase slip lines are generated, which contribute the same amount of resistance to the device. This would result in steps in the resistance vs current curves, which can also be seen from the steadily increasing slope observed in the voltage vs current curves corresponding to jumps in the resistance by $\sim 0.25\Omega$.

and is shown in Fig. 5.13, where the slope of the I-V curve increases by ~ 0.25 Ω after each new phase slip is introduced. In our resistance $(\frac{dV}{dI})$ vs I curves, we would expect to see resistance jumps by a uniform value, however, because we are measuring Shapiro steps, the differential resistance approximately returns to its minimum value at each of the steps. This can be seen in the outer junction (Fig. 5.10) and is specifically highlighted in Fig. 5.14a, where the outer junction clearly doesn't demonstrate the uniform steps in resistance. For the inner junction, it is unclear if this effect is present in Fig. 5.7. However, if another RF power is inspected (Fig. 5.14b), there is clearly no uniform resistance step height in

62

the resistance. The lack of signatures of additional phase slip formation in these devices suggests that a small region of the device with weakened superconductivity may give rise to a single flux flow region or phase slip line. This is in contrast to a relatively uniform device where many phase slip lines could be formed at similar currents (5.13).
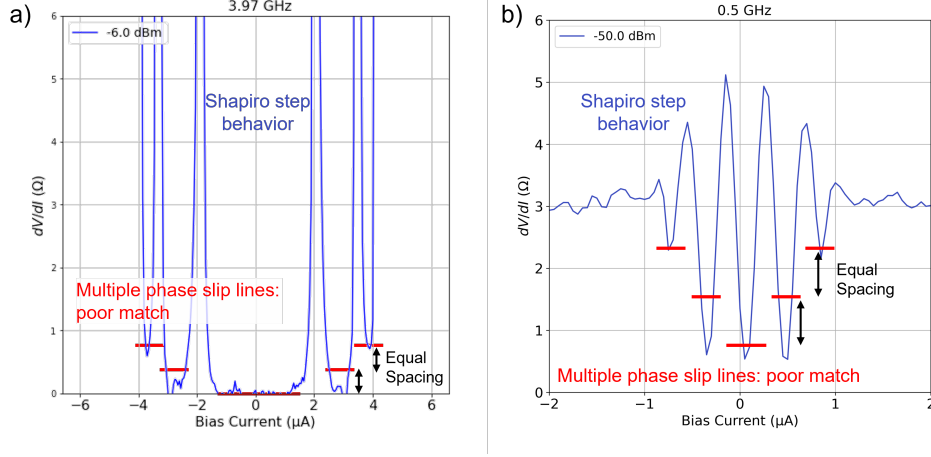
Figure 5.14: $\frac{dV}{dI}$ vs I measurements at a frequency of 3.97 GHz at a power of -6 dBm (a) and 0.5 GHz at an RF power of -50 dBm (b). The absence of a clear, consistent step height in resistance suggests that the generation of additional phase slip lines does not have to do with the jumps measured in $\frac{dV}{dI}$. This suggests that if the Josephson effects are indeed generated by phase slip lines, then there is likely a single flux flow region or phase slip line as opposed to the generation of multiple phase slip lines.

Phase slip lines are generated by a critically large current density in superconducting materials, and therefore a comparison between the critical current density in our device and the critical current densities established in the literature is necessary. The potential regions for phase slip lines in our device are in the Al electrode or in the FeTeSe flake. The thickness of our Al electrode is ~50 nm and the width is ~1 μm, resulting in a cross-sectional area of $\sim 5 \times 10^{-14}$ m^2. The thickness of the FeTeSe flake was not measured but is estimated to be ~50 nm and the width is ~1.8 μm, resulting in a cross-sectional area of $\sim 9 \times 10^{-14}$ m^2. The critical current of the inner junction is ~ 0.25 μA and the critical current of the outer junction is ~ 6 μA; therefore, in the Al electrode, the current density would be $\sim 5 \times 10^6$ A/m^2 for the inner junction and $\sim 1 \times 10^8$ A/m^2 for the outer junction. For the FeTeSe flake, the current density would be $\sim 3 \times 10^6$ A/m^2 for the inner

junction and $\sim 7 \times 10^7 \ A/m^2$ for the outer junction. The current density of 19 nm thick Al is $> 10^{10} \ A/m^2$ according to Ref. [88], and the current density of 120 nm thick FeTeSe is also $> 10^{10} \ A/m^2$ according to Ref. [89]. These are both significantly higher than the current densities of the inner junction or outer junction, and would therefore support the idea that, if phase slip lines are driving the Josephson effects, then a region of weakened superconductivity (with a reduced critical current density) must be necessary to form the phase slip line.

Before moving on, we should note that it is possible for two Josephson junctions in series to give rise to two Josephson effects in a single device. However, based on the Shapiro steps emerging from an envelope characterizing the normal state, it would be more likely that a phase slip line (outer junction) is in series with a Josephson junction (inner junction). Josephson effects arising from a phase slip line are further supported by the dynamic effects, which we will discuss next.

5.3 Jumps in Shapiro Mapping

We investigated the AC Josephson effect for a large number of frequencies and found a surprising phenomenon at select frequencies. Specifically, in the outer junction, there exists a discontinuous jump in the map of dV/dI vs I as the RF power is increased. Figure 5.15 shows this phenomenon for frequencies of 3.45 GHz, where a discontinuous jump occurs at -4.2 dBm. Additionally, it can be seen that after the RF power is increased past -4.2 dBm, the transition to the fully normal state occurs at a higher current (i.e., the outer envelope of the Josephson phenomenon expands after the jump). This would seem to imply a sudden change resulting in enhanced superconductivity at larger RF powers; however, first we must investigate whether these effects are simply an artifact of the measurement.

One reasonable thought when noticing such a jump in the interference pattern of the junction is to question whether it is due to some internal change in the RF source or some
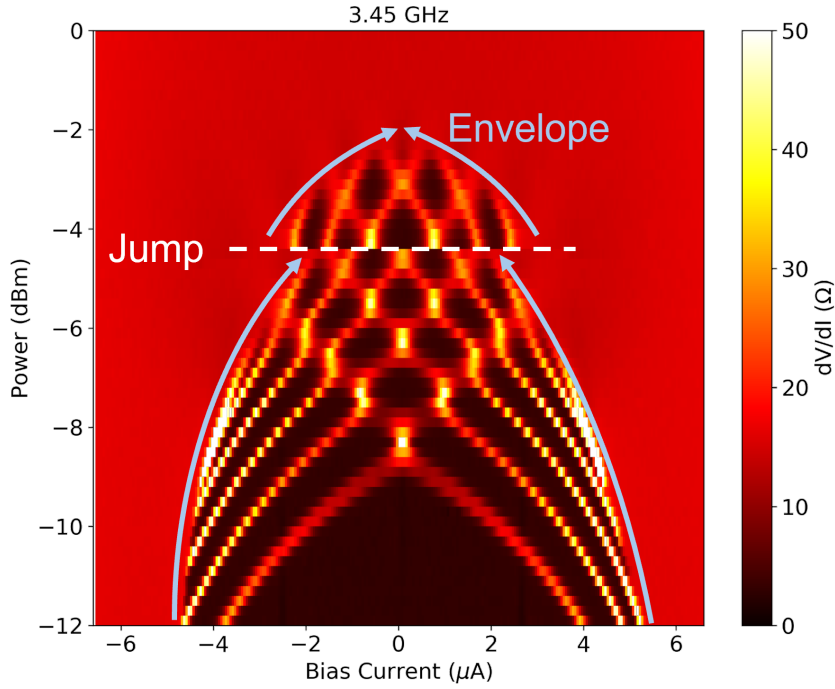
Figure 5.15: A $\frac{dV}{dI}$ vs I vs RF power map at 3.45 GHz. A discontinuous jump in the mapping can be seen at $\sim$-4 dBm. This jump is most evident in the jump in the envelope of the Shapiro steps, which represents the transition to the fully normal state. Another unusual feature of this jump is that, despite the RF power being increased (which would typically decrease the critical current due to heating effects), the current defining the envelope of the Shapiro steps is actually enhanced after increasing the RF power beyond this jump.

artifact of the measurement. However, there are two points that strongly suggest this is not the case.

The first point addresses the idea that the RF power irradiating the junction may have been suddenly lower than expected due to an issue with the RF source, resulting in the sudden jump in the pattern. If this were the case, the dV/dI vs I curve after the jump would be expected to match a region at lower applied RF power. In Fig. 5.16, the peaks in the dV/dI after the jump are outlined in blue (the region above -1 dBm), which can then be matched to a point before the jump (below -1 dBm) based on the envelope of the Josephson phenomena (indicated by a white arrow). The white dotted line shows where the peaks in $\frac{dV}{dI}$ would be if the pattern were shifted down to match the envelope. Besides
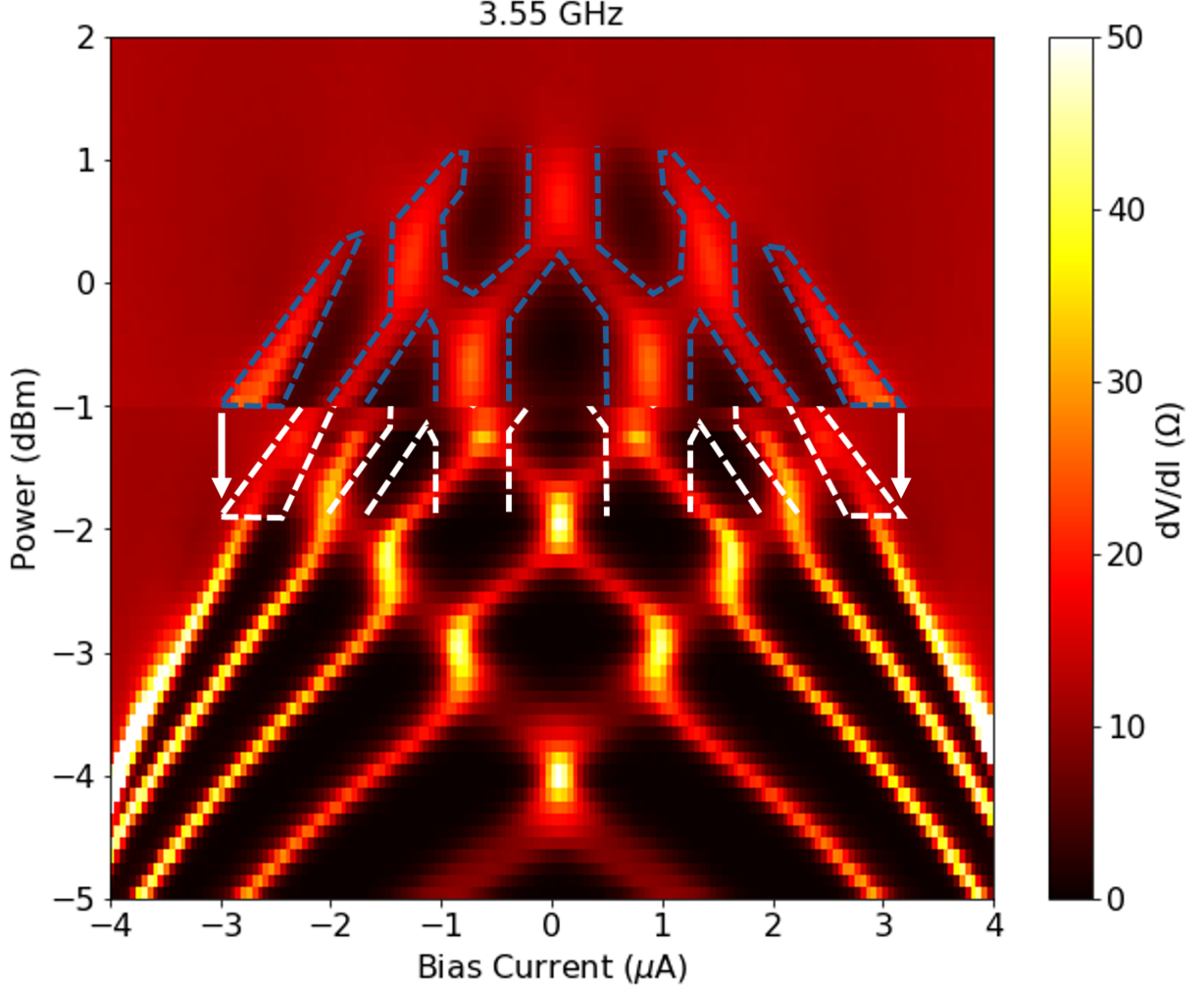
Figure 5.16: A fine resolution mapping of $\frac{dV}{dI}$ vs I at a frequency of 3.55 GHz. In order to determine if the jump is an artifact of the measurement and simply corresponds to a shift in the applied power, we can see if the pattern after the jump can be mapped to a region before the jump. The jump does not appear to be an artifact of the measurement, as the pattern after the jump (highlighted in blue) does not align with the pattern before the jump (highlighted in white). The envelope of the Shapiro steps was used as a guide to decide how much to shift the pattern down.

the envelope, which we intentionally matched, the peaks in the dV/dI curve do not align after being shifted downwards, ruling out the possibility of a shift in the applied power due to the experimental setup.

The second point addresses the idea that this effect may not be repeatable and may occur randomly, which would explain why it is only observed at specific RF frequencies.

Four different mappings were performed at 3.55 GHz with different start and end points and different step sizes (Fig. 5.17). For all of these curves, a jump is observed at -1 dBm, demonstrating that these jumps are not random. However, there are clearly an additional two jumps in (Fig. 5.17d), that do not appear in the other mapping sweeps. This suggests that dynamics are involved in the generation of the jumps, which we will explore further in the discussion section.
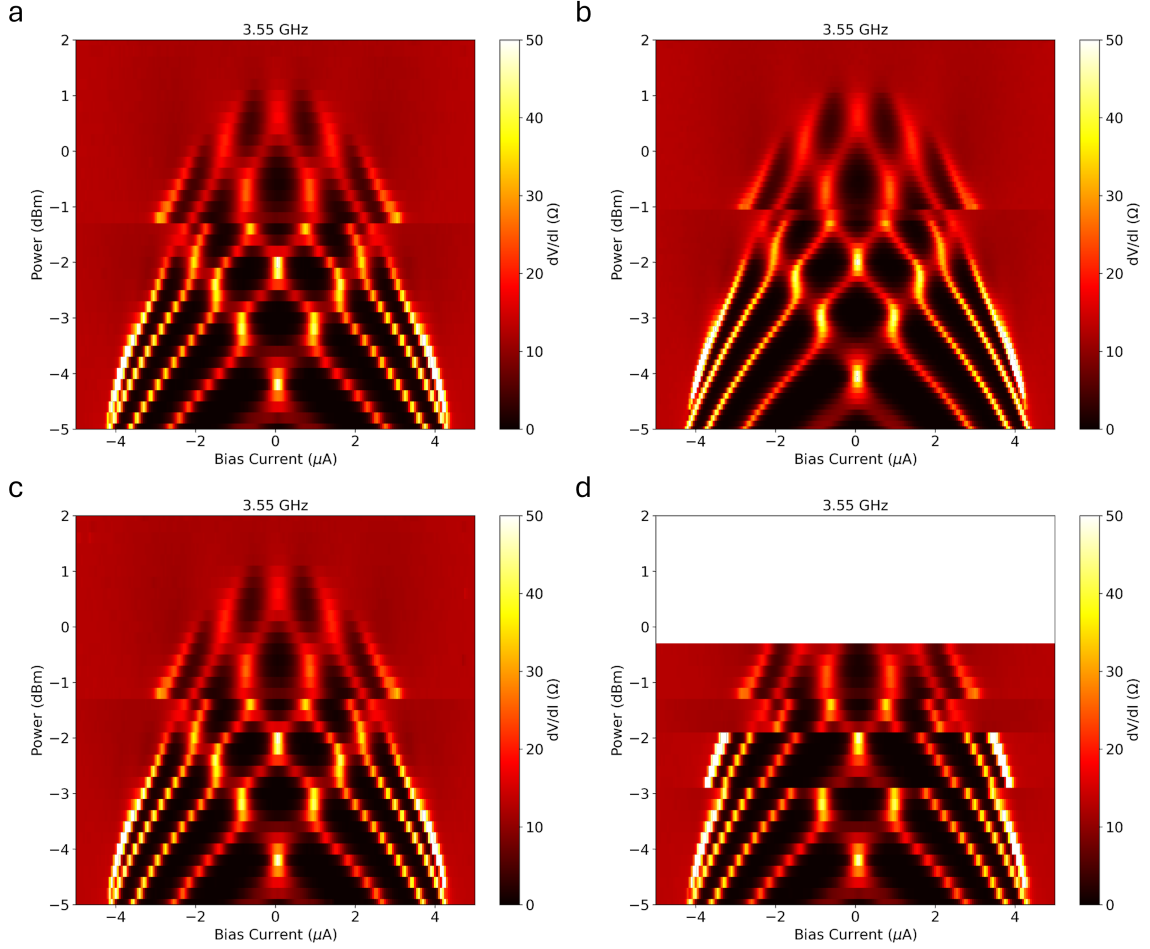
Figure 5.17: a-d) $\frac{dV}{dI}$ vs I vs RF power mapping at a frequency of 3.55 GHz, repeated 4 times. This demonstrates that the jumps are a real, repeatable phenomenon and not due to a random occurrence, such as someone bumping the system. However, it should be noted that this does seem to be a dynamic effect, because in (d) there are two additional jumps at -3 dBm and at -2 dBm not seen in (a), (b), and (c).

Although less pronounced, at higher frequencies, an apparent crossover was observed

in the shape of the Josephson diffraction, without a change in the shape of the envelope of the diffraction. This is most easily visible at 3.98 GHz, where the jump occurs approximately between -1.8 dBm and -1.5 dBm (Fig. 5.18). This is unique, as in other measurements, the jump occurs in a single sweep at a given power step, whereas in this measurement, the individual peaks in dV/dI are modified with a dependence on RF power. Some of the main differences visible before and after the jump are the abrupt change in the peak positions, the modified slope of the peaks vs current and RF power, and the apparent blurring of the peaks. While this is particularly pronounced in this measurement, this effect is visible in other measurements as well (See Data Dump A.4).
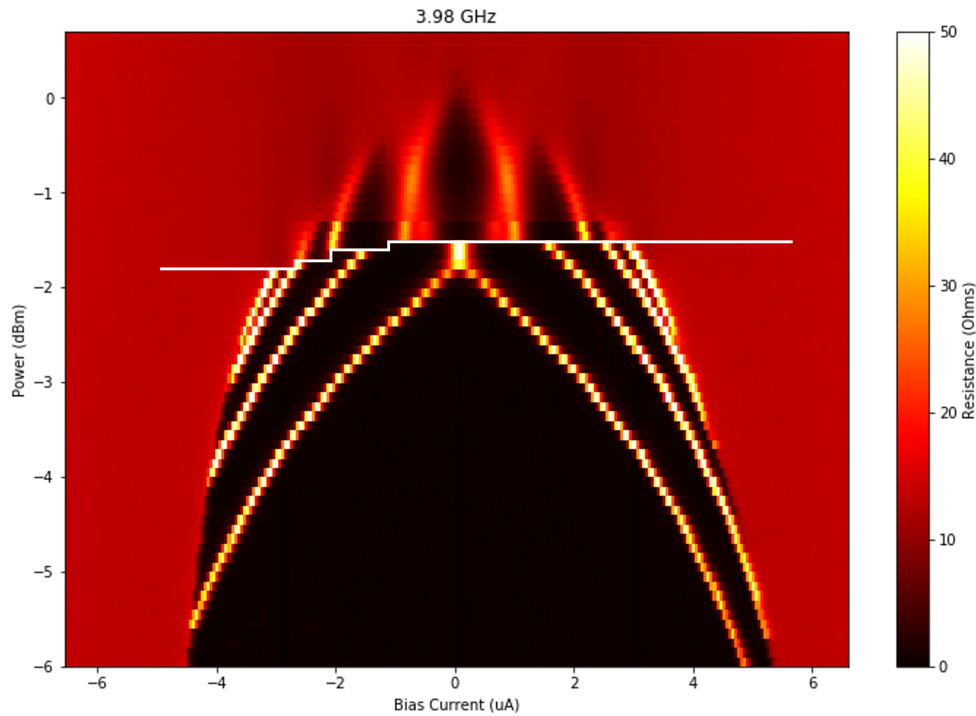
Figure 5.18: $\frac{dV}{dI}$ vs I vs RF power mapping at a frequency of 3.98 GHz. In this measurement, there is minimal change in the envelope of the Shapiro steps; however, there is a clear change in the behavior of the junction. Specifically, there is a discontinuous jump in the peaks in $\frac{dV}{dI}$ as a function of current, and the slope of these peaks vs RF power and DC current changes after the jump. Most interesting is the fact that the jump happens over a range of powers as opposed to at a specific power. This likely rules out frequency infidelity as causing the jumps, as there is unlikely to be a shift in the frequency that occurs differently for positive and negative DC currents, unless it is a physical property of the Josephson junction.
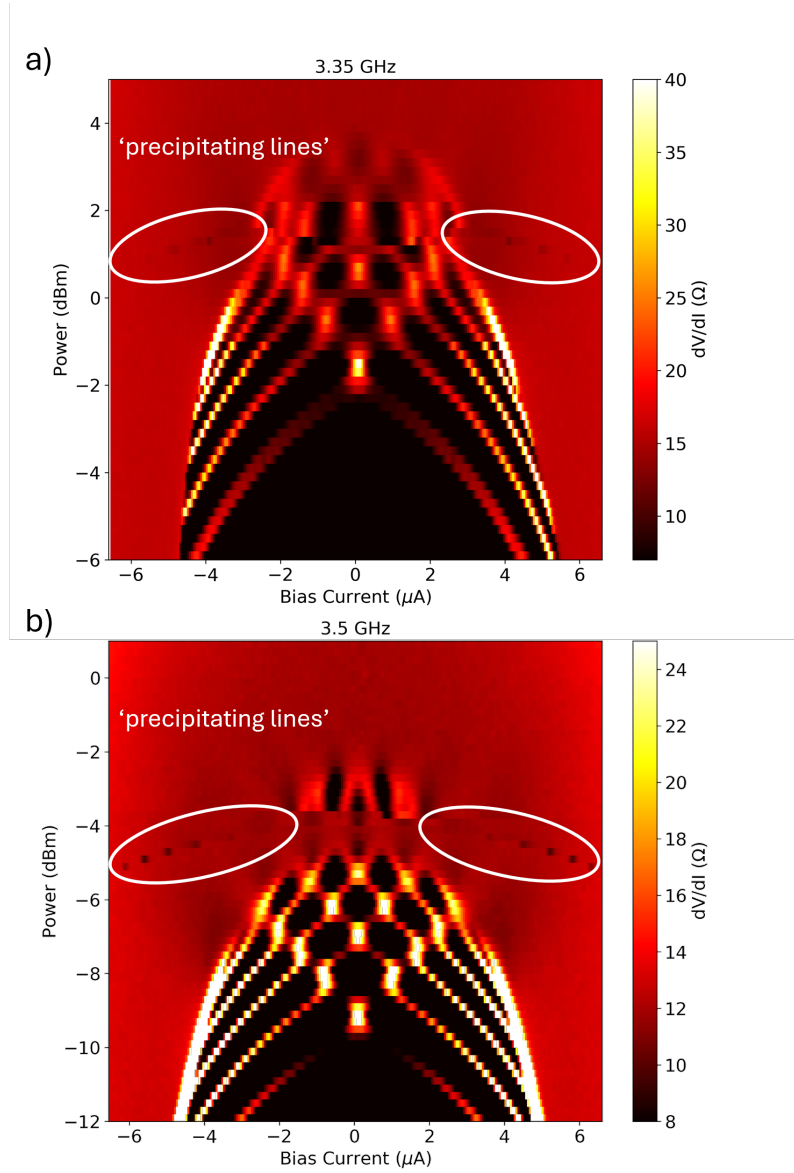
Figure 5.19: a,b) $\frac{dV}{dI}$ vs I vs RF power mapping at a frequency of 3.35 GHz (a) and 3.5 GHz (b). At these frequencies, a small dip can be seen in the differential resistance, which occurs at progressively lower currents as the RF power is increased. These lines seem to precipitate the occurrence of jumps, and in the case of the 3.5 GHz mapping (b), a reemergence of the Shapiro steps after they had nearly disappeared. These precipitating lines further support that the jumps in the Shapiro mapping are a physical phenomenon within the device and not an artifact of the measurement, as they link the lower power behavior before the jump to the higher power behavior where the jump takes place.

Another reasonable question is whether anything measurable precipitates these jumps in the mapping of the dV/dI, which may give some hint as to the origin of this phenomenon.

Indeed, for a number of frequencies, a small dip in the differential resistance approaches the envelope and approximately intersects the point at which a jump occurs (Fig. 5.19). We will refer to these dips as the precipitating lines. It should be noted that color bars on these plots have been modified to highlight the precipitating lines in dV/dI. The interaction between the precipitating lines and the jumps is most clear at 3.5 GHz at -3.5 dBm, see Fig. 5.19b. Specifically, at -4.5 dBm, the interference pattern of the junction has already been considerably weakened, and the resistance is nearly equal to the normal state resistance. However, at -3.5 dBm, the interference becomes strengthened again before diminishing around -2 dBm. This reemergence of the interference clearly seems to be initiated by the precipitating lines. The potential mechanisms giving rise to this effect will be covered in the discussion section. Additionally, the precipitating lines are also visible in devices that demonstrate no jump in the $\frac{dV}{dI}$ mapping (Fig. 5.20); however, for all measurements where the lines are visible and would intersect the envelope, a jump appears (refer to the Appendix Data Dump A.4).

Additionally, frequency infidelity was not previously discussed as a potential cause of the jumps we observe. One could imagine this describing the non-matching of the shifted map (Fig. 5.16), as a different applied frequency will result in a modified interference pattern. Additionally, this could reasonably account for a change in the envelope shape, as different frequencies will be absorbed by the sample more or less effectively (this can be seen from the overall pattern shifting up/down in dBm for different RF frequencies, see Data DumpA.4). However, based on the gradual modification of individual peaks in dV/dI as a function of power, demonstrated in Fig. 5.18, this is extremely unlikely as the frequency infidelity would not occur individually for different peaks (i.e., different values of the DC current) as the power is increased. Further, the precipitation of the jumps by the dips in dV/dI strongly suggests a physical mechanism driving this unusual phenomenon. In the following, I will discuss some potential explanations that may give rise to the jump effect.
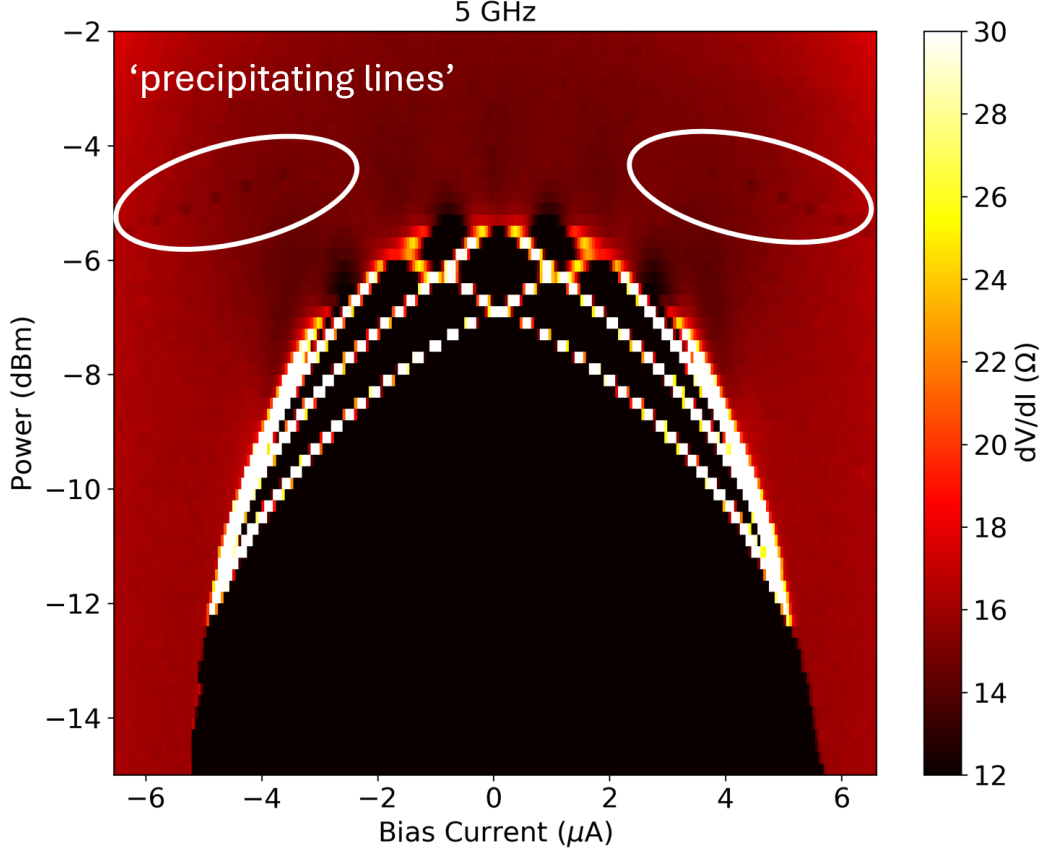
Figure 5.20: $\frac{dV}{dI}$ vs I vs RF power mapping at a frequency of 5 GHz. The precipitating lines are visible within this mapping, but do not intersect the envelope of the Shapiro steps. Consequently, there is no jump in the behavior of the Josephson junction.

5.3.1 Discussion of Jumps in Shapiro Mapping

The jumps in the mapping of the dV/dI spectrum of the 'outer junction' can be described phenomenologically in the context of non-equilibrium superconductivity by two explanations: (1) microwave enhancement of the superconductivity (Ref. [1, 90]) and (2) RF irradiation facilitating the release of trapped vortices, which may suppress superconductivity in the phase slip line through interactions mediated by quasiparticle diffusion.

Explanation 1: The occurrence of quantum coherence effects in phase slip lines necessitates a quantum coherent description, which, in order to accurately capture the contribution of quasiparticles, requires non-equilibrium descriptions of the superconductivity (Ref. [1]). Even for a typical superconducting material without a Josephson junction or phase slip line, there can be significant impacts due to the non-equilibrium quasiparticles generated by RF irradiation (Refs. [1, 90, 91]). In this section, we will follow Tinkham's description of the enhancement of superconductivity in a superconducting bridge under RF irradiation (known as the Wyatt-Dayem Effect) and make extensions to describe the potential phenomena in our system.

Specifically, in the typical BCS description of superconductivity in thermal equilibrium, the occupation of the quasiparticle states outside the superconducting gap can be described by the Fermi function $f = \frac{1}{e^{E_k/k_B T}+1}$. With the typical dispersion given by $E_k = \sqrt{(\Delta^2 + \varepsilon_k^2)}$ where ε_k is the kinetic energy relative to the Fermi level. In equilibrium, due to electron-hole symmetry, there should be an equal number of electron like excitations $(0 < E_{QP})$ and hole like excitations $(E_{QP} < 0)$, however when driven out of equilibrium there can be deviations due to injection of electron like or hole like states (this is referred to as the odd class of disequilibrium by Tinkham, see Ref. [1]). Additionally, modifications to the quasiparticle occupation can be made that respect electron-hole symmetry, effectively increasing or decreasing the quasiparticles symmetrically. This is the primary phenomenon we are interested in, as the modification of the density of quasiparticles will affect the gap of the superconductor, according to the BCS gap equation, $\frac{2}{V_{kl}} = \sum_k \frac{1-2f_k}{\sqrt{(\Delta^2+\varepsilon_k^2)}}$, where V_{kl} is assumed to be a constant by the BCS approximation, and the subscript kl is shown only to clarify this is not a voltage. In this equation, f_k denotes the occupation of the quasiparticle states, which will deviate from the typical Fermi function shown above. As a consequence, modifications to the quasiparticle spectrum that increase (decrease) the quasiparticle density will decrease (increase) the magnitude of the superconducting gap. It should be noted that, often, the odd modifications to the electron-hole symmetry will also

affect the quasiparticle density and will therefore also affect the superconducting gap.

This modification of the superconducting gap can now be applied to the relevant case of RF irradiation of a superconducting bridge. In the correct conditions, where RF irradiation can stimulate an existing quasiparticle state from a low-energy state to a high-energy state with lower quasiparticle density, the superconducting gap can be enhanced (Note: $\hbar\omega < 2\Delta$ such that no new quasiparticles are generated, and the downward transitions from the excited state to the ground state must not be present). Consequently, properties such as the critical current will increase. Wyatt et al. was the first to demonstrate this phenomenon (see Fig. 5.21), where they saw the critical current enhancement under microwave irradiation for low powers and then eventually at higher powers the microwave irradiation suppresses superconductivity, due to heating effects [90].

In our device, there is a sudden onset of enhancement of the superconducting envelope (concurrent with the transition to the normal state) at a critical power, see Figs. 5.15,5.16,5.17,5.19. This is in contrast to the slow increase in critical current at low powers shown in Fig. 5.21 from the original demonstration of the Wyatt-Dayem effect (Ref. [90]). If the Wyatt-Dayem effect were responsible for this phenomenon, then we would imagine that at a critically strong driving power, the quasiparticle spectrum changes. This could be due to a number of dynamic effects which create new quasiparticle states, such as the injection of vortices or the freeing of trapped vortices beyond a critical RF power. In conclusion, the Wyatt-Dayem effect offers a clear and simple explanation of the enhanced superconductivity due to RF irradiation; however, another effect is likely present, which causes the sudden onset of this enhancement effect.

Explanation 2: In our device, the microwave irradiation typically decreases the onset current of the envelope, due to heating. To describe the jump phenomenon, we can use the model of phase slip centers to understand the spatial distribution of quasiparticles in a phase slip line. In a phase slip center, the quasiparticles generated from the dissipation associated with the critical current or Shapiro steps will diffuse in the superconducting
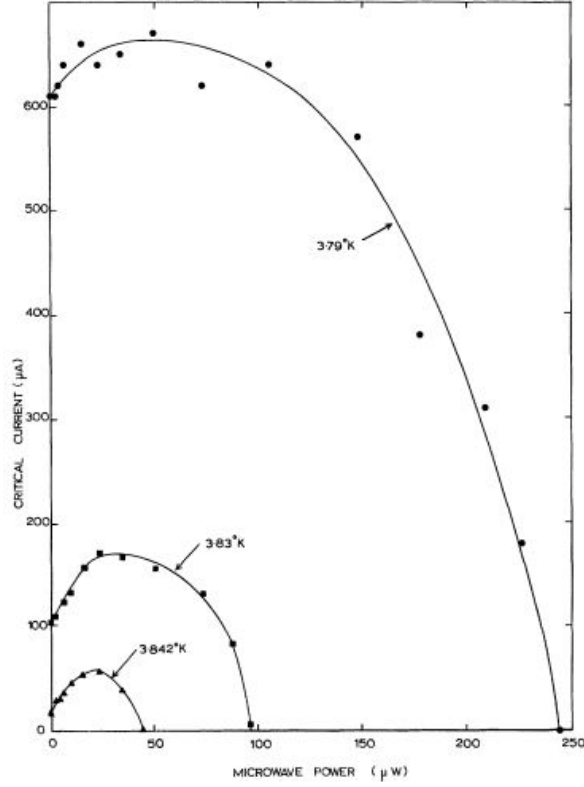
Figure 5.21: The Wyatt-Dayem effect demonstrates the enhanced critical current in superconducting strips of Tin under RF irradiation. Specifically, Wyatt measured the critical current as a function of RF power at a range of temperatures, reprinted from Ref. [90]. They found that for small RF powers, there was an enhancement of the critical current with RF irradiation, and that at large RF powers, the critical current was reduced, which is the typical behavior and is due to heating effects.

bridge over a length scale Λ_Q, which is typically on the order of a few μm (Ref. [1]); however, this can reach a few mm in specially engineered systems (Ref. [92]). In thin uniform bridges where multiple phase slip centers can easily form, this causes a large repulsive interaction between phase slip centers (Ref. [1]). In our system, as we showed earlier, we likely have only one phase slip line; however, other sources of quasiparticles also exist in FTS, such as the CGDM states in vortices pinned to interstitial Fe atoms. If the interaction between the quasiparticles generated in the junction and the quasiparticles of the CDGM states is repulsive (similar to the case of multiple phase slip centers), then pinned vortices in the vicinity of the phase slip line could suppress the superconductivity and decrease the onset current of the envelope. Then, when an RF drive is sufficiently

74

strong to dislocate the vortices from the pinning sites, they would flow away from the phase slip line, thereby decreasing the interaction energy and the quasiparticle density. This would then result in an enhancement of superconductivity, thereby increasing the onset current of the envelope. The proposed vortex-interaction effect is supported by the small dip in the differential resistance, which we refer to as the precipitating lines, which could arise from the generation of quasiparticles from the motion of pinned vortex states.

5.4 Magnetic Field dependence

I next investigated a magnetic field applied out of the plane of the device, shown in Fig. 5.22. If the Josephson effects in the device are governed by flux-flow and phase slip lines, interference effects should give rise to Fraunhofer patterns in the device, due to the perpendicular orientation of the magnetic field relative to supercurrent. In contrast, if the observed Josephson effects were due to the out-of-plane supercurrent at the $FeTe_{0.55}Se_{0.45}$-Al interface, the supercurrent through the junction and the magnetic field would be in the same direction, and therefore, typical Josephson interference would not be expected.
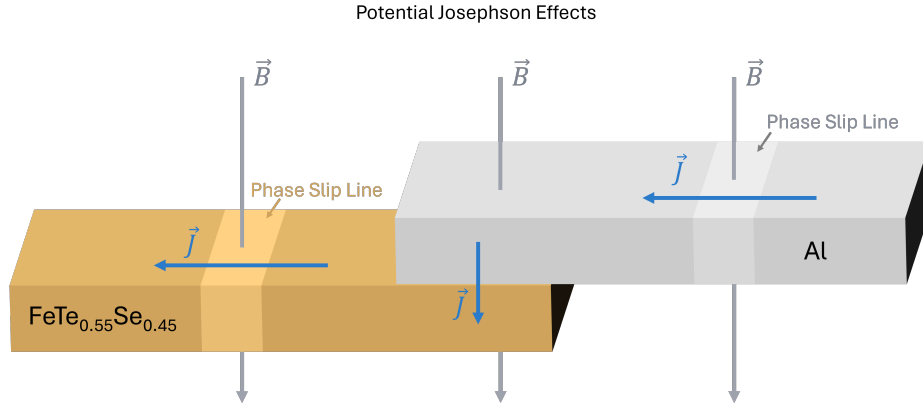
Figure 5.22: Diagram showing the potential regions giving rise to the Josephson effects in this device. The supercurrent is perpendicular to the magnetic field for the phase slip lines and parallel to the magnetic field for the Al-FeTeSe interface. In order to see the Fraunhofer effects usually present in Josephson junctions, the Magnetic field would need to be perpendicular to the supercurrent.

5.4.1 Fraunhofer Measurements of Inner Junction and the Outer Junction

We next examine the magnetic diffraction patterns of our device. In this section, we will comment on some key details and the unusual phenomenon. However, due to the multiple Josephson effects and various ways the magnetic field can interact with phase-coherent transport, we will avoid speculation about the exact mechanisms. Instead, we will focus on some of the extractable features and mention phenomena that resemble the results obtained.
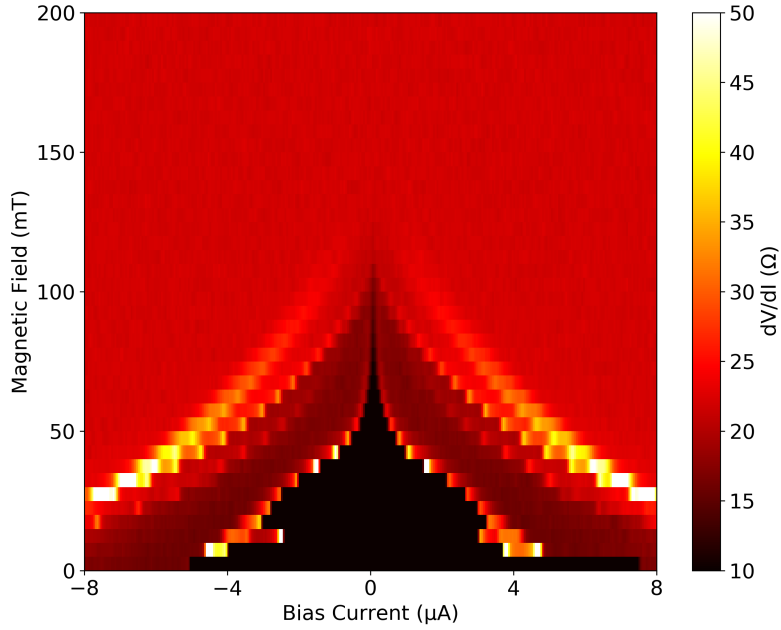
Figure 5.23: The initial sweep of $\frac{dV}{dI}$ vs I vs B up to a magnetic field of 200 mT. In this sweep, only the outer junction critical current is visible, and it appears to oscillate before dropping to zero.

We first performed an initial sweep to a relatively high magnetic field to understand the magnetic field effects in this device (Fig. 5.23). From this sweep, the resistance jump corresponding to the inner junction is not resolvable; however, the resistance jump corresponding to the outer junction is resolvable, and occurs around 4 μA at 0 mT. There appear

to be oscillations in the critical current of our outer junction, which we will investigate with fine sweeps later. Additionally, we can see that the additional resistance jump around 13 μA (with a peak in dV/dI) slowly decreases in current with increasing magnetic field until 100 mT, when these peaks diminish to zero current. This peak likely corresponds to the aluminum electrode being driven into the fully resistive state, as our aluminum electrode is ~50 nm thick and the critical field of aluminum around this thickness is ~100 mT.
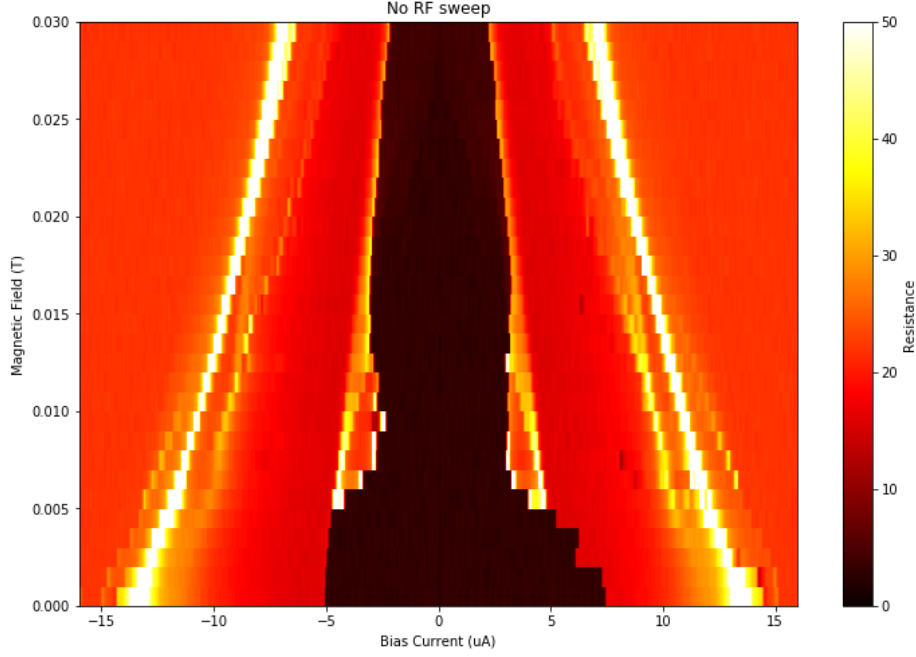
Figure 5.24: A finer sweep of $\frac{dV}{dI}$ vs I vs B up from 0 mT to 30 mT. In this sweep, oscillations of the critical current are visible, which resemble the Fraunhofer pattern typical of Josephson junctions. A Fraunhofer pattern is shown next to the data for reference.

We next investigate the outer junction magnetic field dependence with a fine sweep over a reduced magnetic field range (Fig. 5.24). From this measurement, we can see distinct fluctuations in the critical current of the outer junction, approximately corresponding to a Fraunhofer pattern. A magnetic field oscillation scale of 7-9 mT can be estimated for the interference pattern. Because the Fraunhofer pattern oscillated over a characteristic flux scale of the magnetic flux quantum $\Phi_0 = $ ~2 mT μm^2, the area of the outer junction can be approximated as 0.25 μm^2. If this corresponded to a phase slip line in the superconductors, this area would be equal to the width of the superconducting strip times the penetration

depth. The width of the FeTeSe flake is $\sim$1.8 μm and the width of the Al electrode is $\sim$1 μm; therefore, the width over which the magnetic field penetrates the junction would be $\sim$140 nm and $\sim$250 nm, respectively. This width should be approximately equal to twice the penetration depth of the superconducting films. The penetration depth of Al is $\sim$100 nm for $\sim$50 nm thick films (Ref. [93]) and therefore there is a good qualitative match for the envelope of the outer junction compared to FeTeSe with λ $\sim$0.4-0.5 μm (Refs. [94, 95]).

Next, I performed fine sweeps of the inner junction (Fig. 5.25); however, before doing this, I warmed up the sample above the critical temperatures of both superconducting electrodes to ensure there was no trapped flux in the sample, resulting from the relatively large magnetic fields applied. The critical current of the inner junction drops to zero at $\sim$2 mT and, based on the flux quantum $\Phi_0 = \sim$2 mT μm^2, the area of the junction would be approximately 1 μm^2. For the FeTeSe flake width of $\sim$1.8 μm, this would imply the magnetic field penetrates the phase slip over a width of $\sim$0.6 μm. This would correspond to a penetration depth of $\sim$0.3 μm, which agrees relatively well with the experimentally measured values of λ $\sim$0.4-0.5 μm in FeTeSe crystals (Refs. [94, 95]).

A brief comment on an alternative description: While above we have discussed the Fraunhofer patterns arising from a phase slip line, it is possible that either the inner junction and/or the outer junction exists at the FeTeSe-Al interface. In this case, the magnetic diffraction patterns may arise from the vortices induced in the Al or FeTeSe electrodes by the external magnetic field.

5.4.2   Magnetic Field and RF Irradiation

Motivated by the unusual AC Josephson effects we saw in (Fig. 5.3), I next investigated the magnetic field dependence under RF irradiation. Specifically, I investigated changes in the inner junction and the outer junction, as well as around the jumps in RF power.

For the inner junction, we investigated the magnetic field dependence at a number of frequencies and powers, focusing on the frequencies where the Shapiro steps are the most
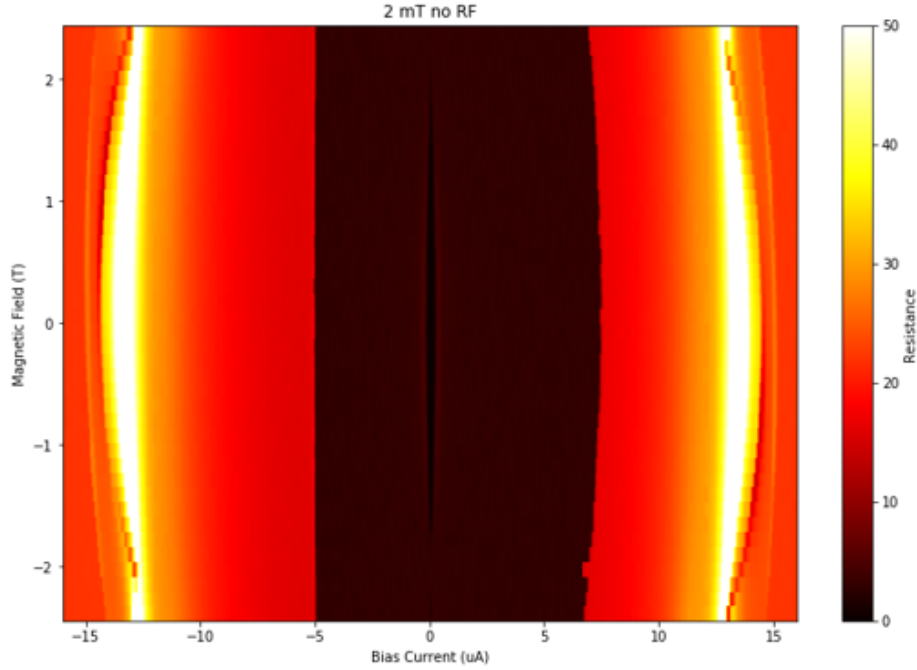
Figure 5.25: A fine sweep of $\frac{dV}{dI}$ vs I vs B from -2 mT to 2 mT showing the magnetic field oscillations of the inner junction. Concurrent with the typical case of Fraunhofer diffraction, there is a maximum of the critical current at B=0 and the critical current decays to zero at $\sim 2mT$.

pronounced. Figure 5.26) shows a sweep at 2 GHz and -45 dBm, the critical current decays over the same magnetic field shown in Fig. 5.25 (See the Data Dump A.4 for additional sweeps at different frequencies and powers). For both Josephson junctions and phase slip lines, this is typical behavior; the application of RF usually does not change the magnetic field diffraction substantially. One example in a more closely related system is phase slip lines in NbSe$_2$ crystals (Ref. [86]), which show the typical Fraunhofer in addition to some field-insensitive features.

Surprisingly, when the frequency is increased (Fig. 5.27), such that the Shapiro steps of the outer junction become pronounced, the magnetic diffraction pattern becomes modified. Specifically, the critical current and Shapiro steps have a minimum at $B = 0$ T (Fig. 5.27a) as opposed to the maximum at $B = 0$ T seen in the absence of RF irradiation (the typical Fraunhofer pattern). This unusual behavior, where the critical current and the Shapiro steps occur at larger currents under the application of a magnetic
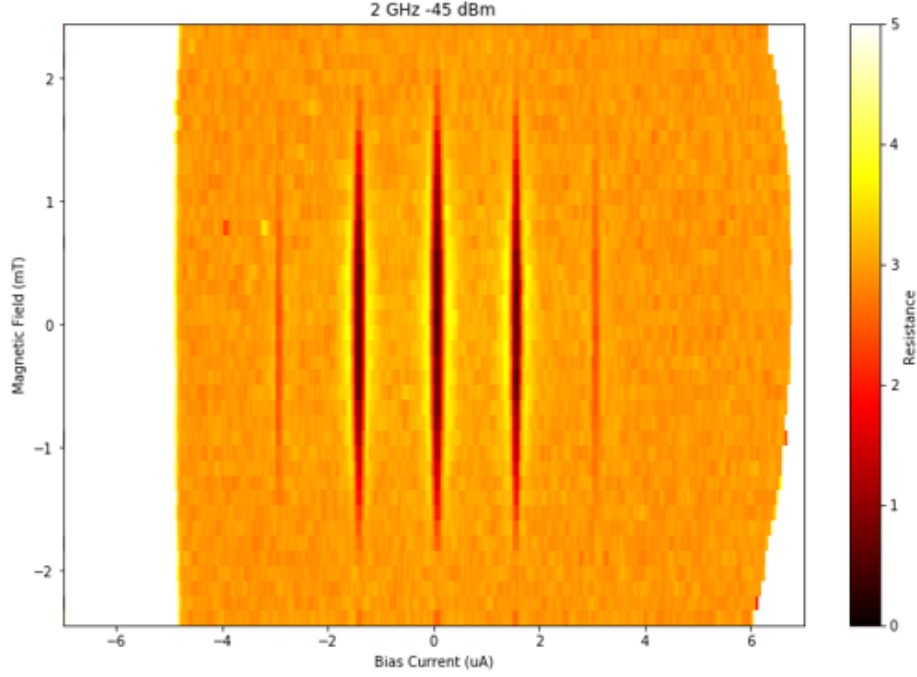
Figure 5.26: A fine sweep of $\frac{dV}{dI}$ vs I vs B from -2 mT to 2 mT, taken under 2 GHz RF irradiation at a power of -45 dBm. Similar to the case of no RF irradiation, the critical current decays over $\sim 2mT$. This is also the case for the Shapiro steps.

field, is typically only observable in systems utilizing magnetic materials (Ref. [96]) or multiband superconductors (Ref. [97]). Another feature of this magnetic diffraction is that the envelope of the outer junction is unmodified from its initial shape, and varies minimally over the small range of magnetic fields. We should note that this phenomena was measured at higher powers than we initially probed the inner junction. This was done so that the Shapiro steps could be resolved for the inner and outer junction, however it is reasonable to question if the increased power would have had a similar effect on the inner junction. When the scale is adjusted, the Shapiro steps of the inner junction are visible in Fig. 5.27 b and show the same qualitative behavior as in Fig. 5.25 (maximum in critical current at B=0) in contrast to the unusual behavior of the outer junction in Fig. 5.27.

We can investigate this effect now at a frequency where we initially saw a jump in the RF signal, 3.98 GHz (Fig. 5.28a). We first sweep the magnetic field at low power of -3 dBm, which is before the jump in the Shapiro mapping (Fig. 5.28b). This RF power is signified by a white line in the Shapiro map, shown in Fig. 5.28a. The mapping reveals a similar
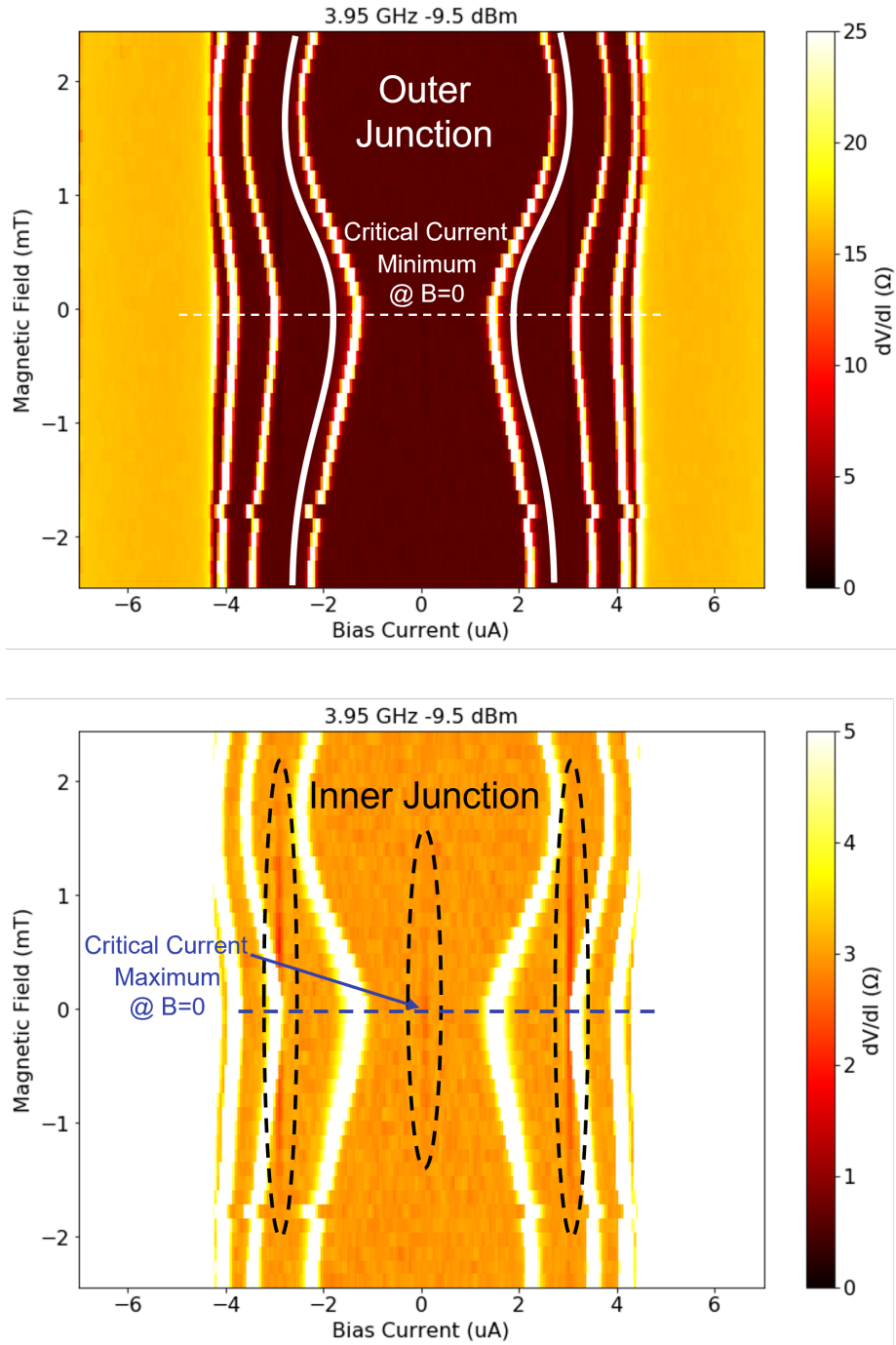
Figure 5.27: a,b) A fine sweep of $\frac{dV}{dI}$ vs I vs B from -2 mT to 2 mT, taken under 3.95 GHz RF irradiation at a power of -9.5 dBm. A minimum in the critical current of the outer junction can be found at B=0 (a). This unusual phenomenon is typically only found in Josephson junctions with magnetic tunnel barriers or multiband superconductor Josephson junctions. In contrast, at the same RF power and frequency, the inner junction retains the critical current maximum at B=0. This maximum is visible for the critical current as well as for the first Shapiro step of the inner junction.

phenomenon to Fig. 5.27 where there is clearly a minimum in the critical current and Shapiro steps at $B = 0 \ T$. Similarly to the data at 3.95 GHz, there is minimal modification of the envelope of the outer junction at this power.

Next, the magnetic field was swept at an RF power of -1 dBm at 3.98 GHz after the jump in Shapiro mapping, shown in Fig. 5.28c. Surprisingly, at this power, the envelope of the outer junction also demonstrates strong oscillations with the magnetic field, over the same magnetic oscillation scale of 5 mT as the Shapiro steps. Additionally, the dV/dI peaks exhibit varying dependence on the applied magnetic field, with some decreasing and others increasing. This is most visible from the splitting of the merged dV/dI peak at zero magnetic field as the magnetic field is increased. Additionally, there are crossings between these peaks at ± 1 dBm. This unusual phenomenon clearly demonstrates the coupling between the magnetic field and the dynamics of the outer junction.

5.4.3   Discussion

In a typical Josephson junction, the Fraunhofer pattern obeys the equation $I_{max} = I_0 \left| \frac{\sin\left(\frac{\pi \Phi}{\Phi_0}\right)}{\frac{\pi \Phi}{\Phi_0}} \right|$ as shown in Section 4.1, where I_0 is the critical current, Φ is the magnetic flux, and Φ_0 is the magnetic flux quantum. The maximum critical current occurs at $B = 0 \ T$, however, this is not the only possible case. In Josephson junctions incorporating magnetic materials as the barrier material, and in Josephson junctions comprising multiband superconductors, the minimum energy of the Josephson junction can occur at a nonzero phase. Under certain circumstances, this corresponds to a nonzero flux in the Josephson junction at $B = 0 \ T$, which is sometimes referred to as a π-Josephson vortex or a π-Josephson junction (in contrast to the typical case of a 0-Josephson junction). The result of this is a minimum of the critical current at $B = 0 \ T$ and an overall dependence given by $I_{max} = I_0 \left| \frac{\sin^2\left(\frac{\pi \Phi}{2\Phi_0}\right)}{\frac{\pi \Phi}{2\Phi_0}} \right|$ for some Josephson junctions based on multi band superconductors, shown in Fig. 5.29. Previous studies on FeTeSe-based Josephson junctions measured a mixture between 0-Josephson

junction behavior and π-Josephson junction behavior [61], which can often be due to disorder effects, and is in contrast to the clear critical current minimum at B=0 measured in our device (See Chapter 3, for more details about the previous FeTeSe Josephson junctions).

There are two probable explanations for the critical current minimum at B=0 measured in our device. 1) FeTeSe is a multiband superconductor, and Gray et al. (Ref. [58]) demonstrated higher-order topological superconductivity on the surface of FeTeSe. Whether by a phase slip line in FeTeSe or at the interface between Al and FeTeSe there could be a Pi-Josephson junction. However, it should be noted that for this to be the case, there would need to be a differential coupling to the two bands of FeTeSe, which would not be the typical case, as FeTeSe has an isotropic superconducting gap in k-space. In comparison, YBCO has superconducting nodes with opposite signs of the order parameters on either side of the node; therefore, by contacting the different faces of the YBCO crystal, differential coupling can be achieved spatially (Ref. [97]). It is possible that the opposite sign of the order parameter on the top and side surfaces could provide this differential coupling in FeTeSe (Ref. [58]). 2) FeTeSe is known to have excess Fe at the interstitial positions, as we discussed in Section 3.2. The interstitial Fe atoms can induce pinned superconducting vortices due to the magnetic impurity moments, as is shown in Ref. [98]. The magnetic field from pinned superconducting vortices can introduce non-zero flux in the Josephson junction/phase slip line at zero applied magnetic field, as has been shown by Ref. [99]. This could potentially account for the minimum in the critical current at $B = 0$ T measured in our devices.

Based on this description of a Pi-Josephson junction, the first minimum in the critical current should correspond to $2\Phi_0/\Phi$ as opposed to Φ_0/Φ. This would imply that the minimum at $\sim$5 mT actually indicates an evolution of Φ_0/Φ every $\sim$2.5 mT. This is very close to the magnetic oscillations of the inner junction, which occur at $\sim$ 2 mT, and as we stated previously, these match well to the FeTeSe width of 1.8 μm and the penetration depth of $\sim$0.4-0.5 μm (Refs. [94, 95]) based on the magnetic flux quantum of $\Phi_0 = \sim$2

mT μm^2. The agreement between the magnetic length scales of the inner junction and outer junction and the penetration depth of FeTeSe suggests the Josephson effects observed are likely related to phase slip lines in FeTeSe.

5.5   Summary

In summary, we measured unconventional Josephson effects in a FeTeSe-Al device. Two distinct Josephson effects were measured, which we suggest may arise due to a flux flow state and a phase slip line. Abrupt jumps were measured in the mapping of $\frac{dV}{dI}$ vs I and RF power. These likely arise due to non-equilibrium effects such as the Wyatt-Dayem effect (Refs. [90, 91]), or vortex-phase slip line interactions. A minimum in the critical current was measured at $B = 0\ T$ in analogy to Pi-Josephson junctions utilizing magnetic materials or multi-band superconductors. If the Fraunhofer pattern of the Josephson junctions based on multi-band superconductors is considered, the period of the diffraction is doubled. This would reconcile the different oscillation periods of the critical current of the inner junction ($\sim 2\ mT$) and the outer junction ($\sim 5\ mT$). The area of the flux penetration for a phase slip in FeTeSe is approximately twice the penetration depth ($0.4 - 0.5\ \mu m$) times the width ($\sim 1.8\ \mu m$). Therefore, there is a good match to the magnetic flux quantum of $\sim 2\ mT/\mu m^2$, suggesting phase slips in FeTeSe as the primary driver of the Josephson effects in our device.

For future investigations on similar devices, the use of a vector magnet could be extremely valuable. Vector magnets can apply magnetic fields with an arbitrary direction in 3 dimensions. This flexibility would not only improve the understanding of where the Josephson phenomena are taking place (in the phase slip lines vs Al-FeTeSe planar junction), but it could potentially offer a deeper understanding of the many novel effects arising in devices based on FeTeSe.
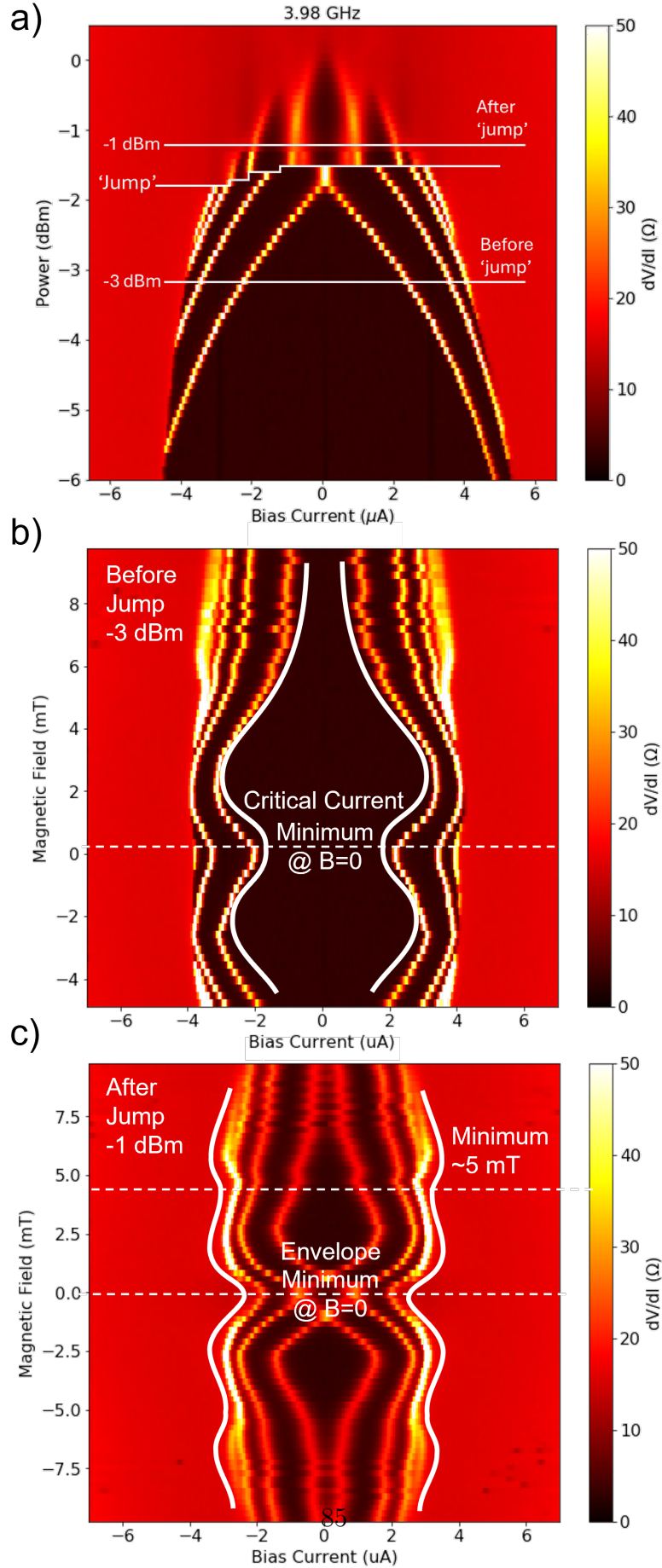
Figure 5.28: a) $\frac{dV}{dI}$ vs I measurements at a frequency of 3.98 GHz, highlighting the RF powers where the subsequent magnetic fields will be performed. b) $\frac{dV}{dI}$ vs I and B at a frequency of 3.98 GHz and a power of -3 dBm (before the jump). Here, a minimum of the critical current is observed at B=0; however, the envelope is relatively unmodified and retains a maximum at B=0. c) $\frac{dV}{dI}$ vs I and B at a frequency of 3.98 GHz and a power of -1
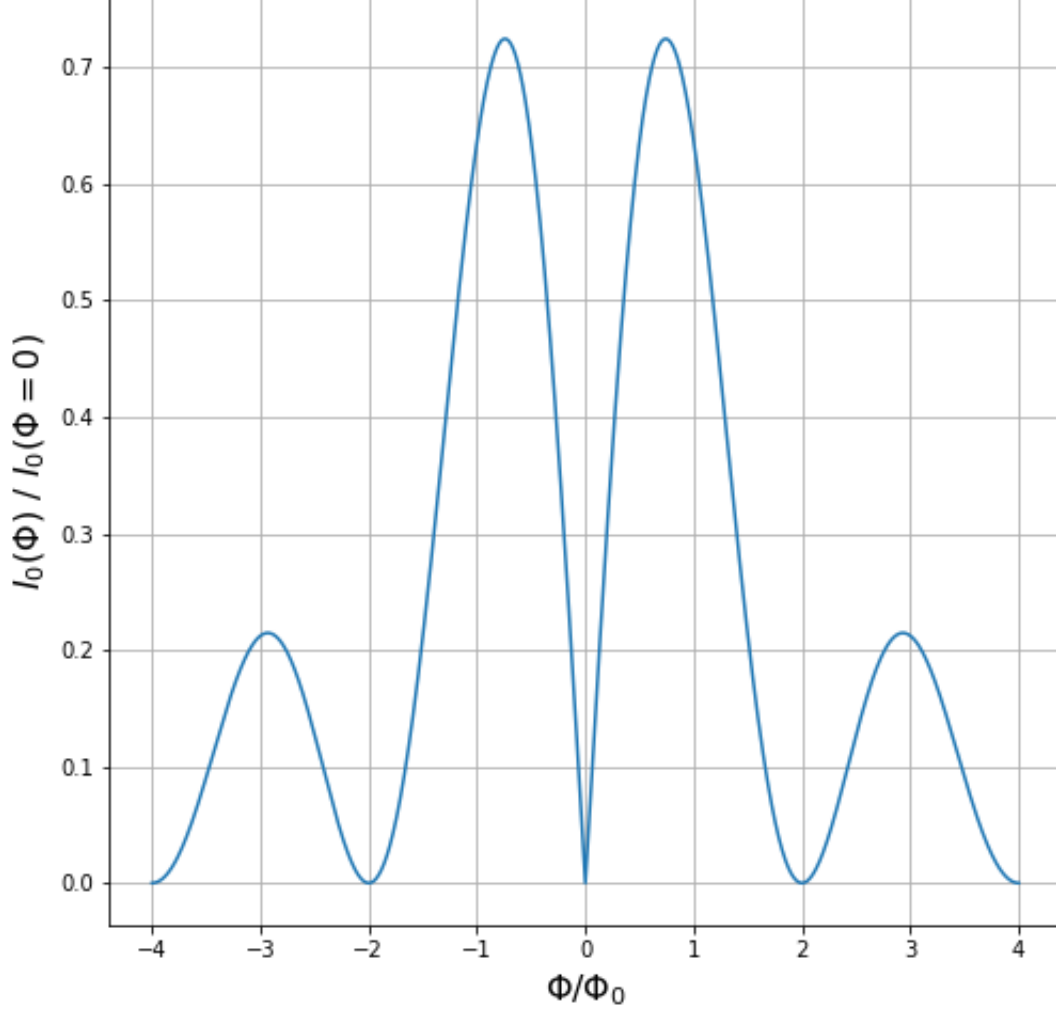
Figure 5.29: Magnetic diffraction pattern for a π-Josephson junction formed at a YBCO corner junction, as was investigated by Wollman et al. [97]. The unique aspects of this junction are the anisotropic multiband superconductivity, such that there will be a relative phase difference of π between the Josephson junction on the different edges. The primary consequences are a minimum of the critical current at B=0 and oscillations of the critical current over $2\Phi_0/\Phi$ as opposed to Φ_0/Φ for a typical junction. This could explain the roughly doubled scale of the magnetic oscillations in our outer junction (5 mT) vs our inner junction (2 mT).

Chapter 6

Conclusion and Outlook

In this thesis, I attempt to give the reader an understanding of the current state of research on FeTeSe, explain the unconventional Josephson effects we measured in a FeTeSe device, and (in the Appendix) provide sufficient technical details for the students who will inherit the metal deposition systems I managed.

We began by giving a brief overview of the basic phenomenon of superconductivity, followed by a review of the development and current state of research regarding the unconventional superconductor FeTeSe. This review was concerned with the development and improvement of the material system, the multiband effects in FeTeSe, and the topological superconductivity in FeTeSe. The topological superconductivity and the search for topological quantum computation are the primary drivers of research in this material system. After this, we provided some simple derivations of the Josephson equations, explained the emergence of Shapiro steps, and finally derived the Fraunhofer pattern that arises in the presence of an external magnetic field. Finally, we discussed the unusual Josephson effects measured in our devices. Particularly, these measurements suggested the importance of non-equilibrium effects such as phase slip lines and quasiparticle diffusion. These non-equilibrium effects are relevant for a broad range of superconducting devices, as quasiparticle poisoning is of primary concern for superconducting qubits.

Looking to the future of research on FeTeSe, there are two primary directions: 1) the focus on topological quantum computation and 2) the measurement of new and unique superconducting phenomena.

For the focus on the realization of topological quantum computation, considerable effort has been spent investigating and verifying the presence of Majorana bound states. However, as is the case for topological quantum computation more broadly, readout and manipulation of the quantum information encoded in the Majorana bound states remain the primary challenge. Whether new schemes for control of the Majorana bound states can be established will likely determine whether successful readout of the parity will be possible. Avenues focused on moving superconducting vortices are promising because the Majorana bound states are bound to the vortex cores. A speculative direction: It has been shown that a laser beam can move superconducting vortices due to the weakened superconductivity at the laser position. Based on this idea, a weak annular laser could define a racetrack for the vortex to move around. Small currents could be used to drive the vortex or vortices around this racetrack and exchange their positions for braiding operations.

The second research direction is more akin to my work, revealing the unusual superconducting phenomenon that can emerge in such a rich platform. My work, like that of many others, found novel and unusual effects using relatively standard investigation techniques. As this continues and new investigation techniques are developed, the tapestry of new phenomena discovered in FeTeSe will enrich the understanding of this unique material.

Appendix A

Appendix

A.1   Lock-in, DC, RF, and B-Field in a Dilution Refrigerator

Here, I will discuss the measurement setup I utilized to measure the Josephson junctions with a focus on a plain language approach that I hope will be beneficial for students unfamiliar with these methods.

A.1.1   Lock-in Measurements

I will now give a brief overview of Lock-in measurements, highlighting some of the advantages of this technique. I will avoid a detailed discussion of Lock-in amplifiers as these have been discussed extensively in a number of references. My preferred reference is chapter 8.8 of Introductory Electronics for Scientists and Engineers by Simpson[100].

Lock-in measurements are measurements of where voltage is applied at a low frequency (I typically use $\sim$13 Hz), and the low frequency response is measured. Lock-in measurements rely on a simple, commonly known mathematical expression,

$$\frac{1}{\tau} \int_0^T sin(\omega_1 t) sin(\omega_2 t) dt \approx 0, \quad \omega_1 \neq \omega_2 \tag{A.1}$$

for sufficiently long times τ. Where ω_1 is the internal reference frequency of the lock-in amplifier and ω_2 is the measured signal. When $\omega_1 = \omega_2$, there will be a DC component to the signal $(1/2)$ which is not averaged out with time. This is the signal we intended to measure, and in real measurements, the output is a differential measurement of the resistance $\frac{dV}{dI}$ (in real measurements τ will be finite, and therefore there can be contributions from other frequencies such as $\omega_2 = 2\omega_1$). Because this measurement is sensitive to phase (a $\pi/2$ phase shift would make the integral $\frac{1}{T} \int_0^T sin(\omega t)cos(\omega t)dt \approx 0$), there are typically two integration circuits out of phase by $\pi/2$ so the full phase information can be measured. This lock-in amplifier performs the multiplication and integration through analog or digital circuitry, depending on the lock-in amplifier. In our measurements, we typically utilized a Stanford Research SR860 or SR830 Digital Lock-in Amplifier [101]. The main advantage of Lock-in detection is excluding all frequencies but the intended frequency, which drastically improves the signal-to-noise ratio. This particularly helps attenuate some of the most common sources of noise such as $1/f$ noise (arising from accumulation of signal mixing at low frequencies $sin((\omega_1 - \omega_2)t)$), Johnson-Nyquist thermal noise (only partially attenuated due to the near constant power spectral density), 60 Hz noise (arising from AC power source also known as 'electrical hum'), and shot noise (though this is only significant in systems where the discrete nature of electric charge is relevant)[100].

A.1.2   Current-Bias Measurements

I will now give an overview of how to perform current bias measurements and highlight their advantages for measuring devices with small electrical resistance and, in particular, superconductors. The typical measurements scheme, which was historically used for nearly all measurements, is to apply a voltage to a device and measure the current through it. However, this can encounter some issues when the resistance of the device is small. Particularly, if the resistance of the device is smaller than, or on the order of the lines/metal

electrodes, then the applied voltage from the voltage source will not necessarily be the applied voltage to the device, as there will be significant voltage drops across this component. One way to solve this is to also measure the voltage across the device, using a four-probe scheme to exclude the resistance of the lines. However, this measurement scheme will result in I-V curves where neither axis has a uniform spacing, which can make post-processing difficult and lead to a parameter space with sparse data points. A clear example of this was in the landmark measurements by Shapiro et al. [63] which used a voltage-bias technique, as was the standard at the time A.1.
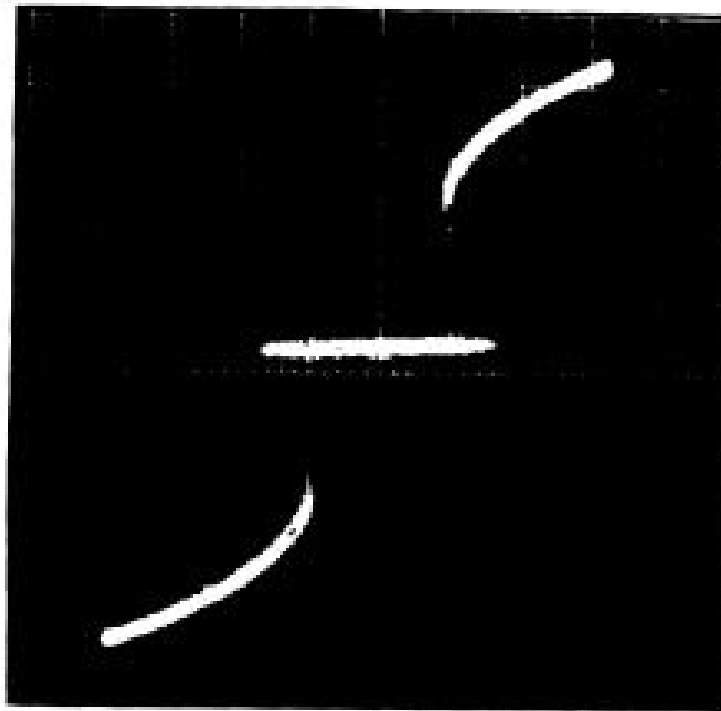
Figure A.1: A typical current-voltage curve, where current is shown on the x-axis and voltage is shown on the y-axis, adapted from Ref. [63].

A simple solution to this issue, which guarantees a well-controlled variable with uniform spacing, is the current-bias method. The current-bias method involves applying a current and measuring a voltage, which is achieved by using a large bias resistor in series with the voltage source (I used a 1 $M\Omega$ bias resistor in my measurements). This resistance which is much larger than the resistance of the device (less than 20 Ω in my devices) means

that even fluctuations in the resistance of the device will result in minimal changes in the overall current of the system A.2 on the order $\pm R_{Device}/R_{Bias}$ which for our device is less than a 0.1% variation.

$$V = I(R_{Bias} + R_{Device}) \approx I R_{Bias} \tag{A.2}$$

The current can therefore be swept in constant steps, and the voltage is measured across the device using a four-probe method, to exclude the voltage drop across the lines A.2. This is particularly useful in measuring the critical current of superconductors and Shapiro steps, where the extremely flat plateaus in the current-bias measurement would, in the voltage-bias measurement, appear as large fluctuations in the measured current due to the multi-valued nature of the function at these flat plateaus. A.3.

In order to perform these current bias measurements using a Lock-in, a DC current must be applied as well. This is done by connecting the DC voltage source (with a current-bias resistor) and a Lock-in (with a current-bias resistor) in parallel A.4.

A.1.3   Measurements in a dilution refrigerator

Performing current-bias measurements in a dilution refrigerator at mK temperatures requires consideration of the measurement lines to ensure they don't create an easy pathway for heating due to electrical and thermal transport. To thermalize the electrons for our current bias measurement, the wires are in contact with a piece of gold-plated copper at each of the plates of the dilution refrigerator. Further, in our Leiden Dilution refrigerator, we utilized a zigzag gold pattern on a Sapphire (AlO_2) substrate, taking advantage of the fact that Sapphire is a good thermal conductor and a good electrical insulator, so it can dissipate heat from the electrons without shunting the current. Further, the contributions from high-frequency noise can be mitigated by using low-pass filters (typical cutoff around 100 Hz) on these lines. Figure A.5 shows this setup schematically.
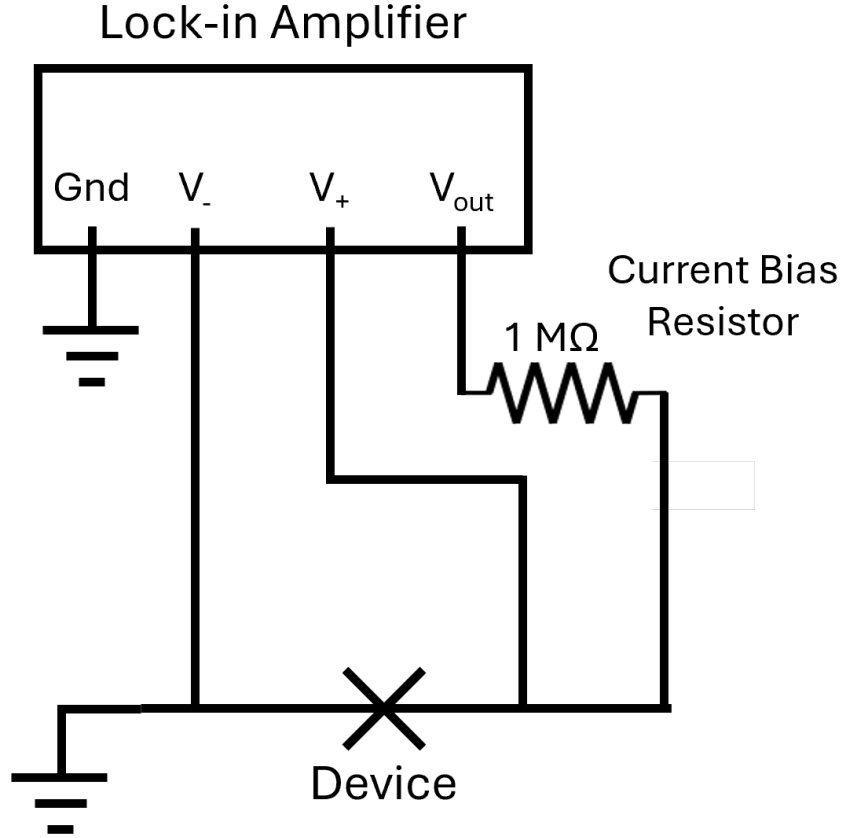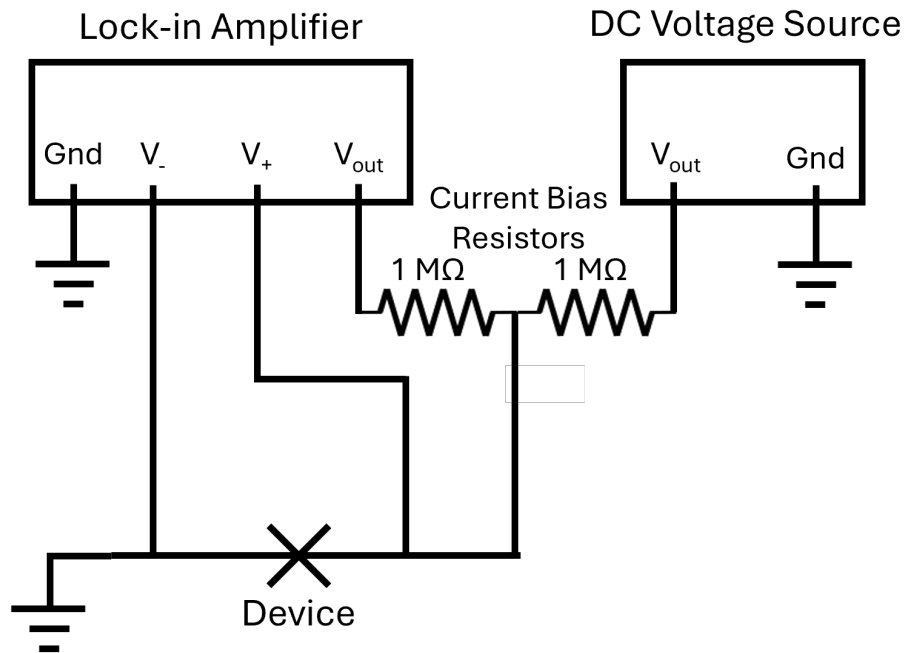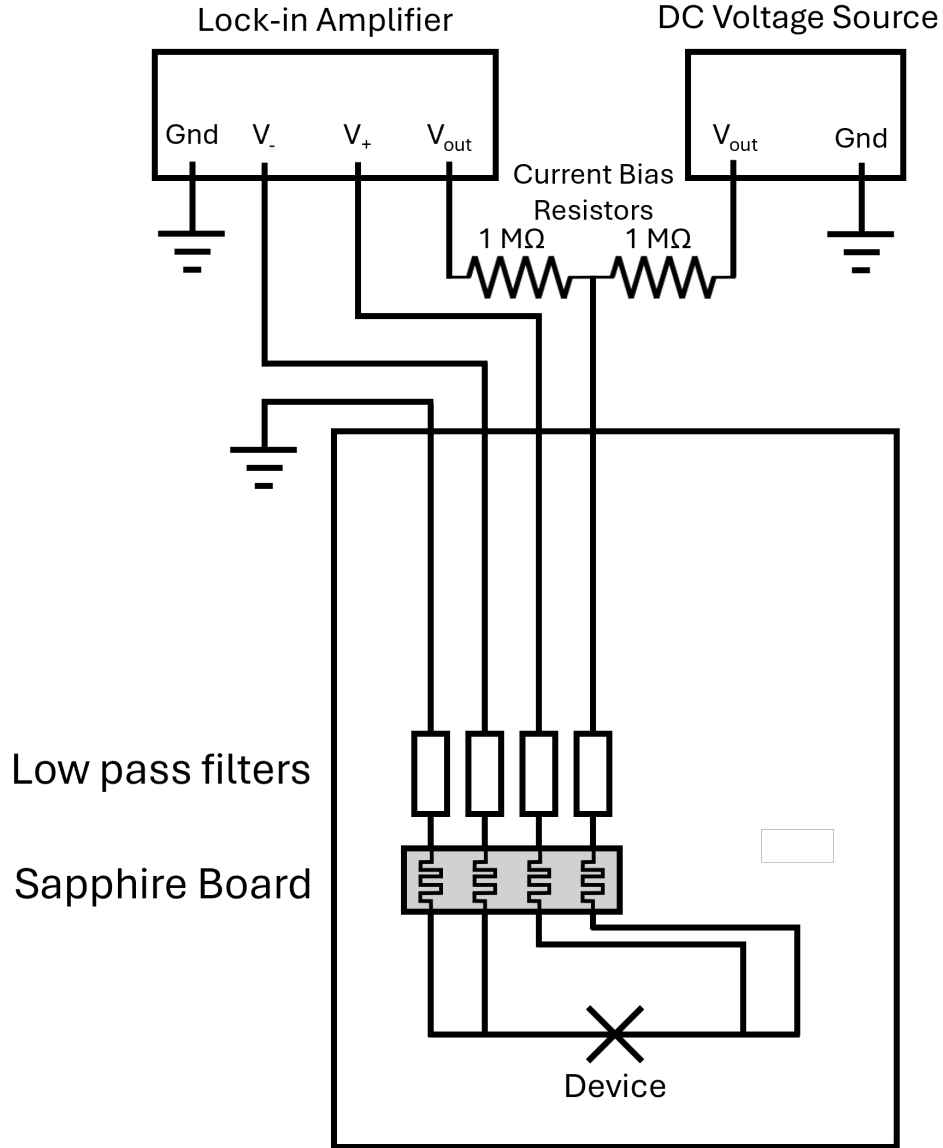
Figure A.2: Lock-in current-bias measurements utilizing a 1 MΩ resistor to set the current bias from the Lock-in voltage, resulting in the measurement of $\frac{dV}{dI}$. A Lock-in frequency of ~ 13 Hz is typically used.

In addition to measuring the I-V relation, we want to irradiate our sample with RF photons so that RF Josephson effects, such as Shapiro steps, can be measured. However, to achieve this, we clearly need to use other lines than the ones mentioned above, as the low-pass filters will filter out our RF signals, which are in the GHz range. For these measurements, we use SMA connectors (as is typical for RF electronics) to connect to 50 Ω impedance matched lines, so that there are no unwanted reflections of our signal. However, simply running a coaxial cable down to our sample is not sufficient for measurement, as this will be an ideal pathway for thermally excited voltages to cause heating in our sample. Therefore, attenuators can be attached to each plate of the dilution refrigerator, decreasing the overall signal at each stage but also decreasing thermal excitations from the higher temperature above plates as well. This significantly reduces the thermal energy transmitted
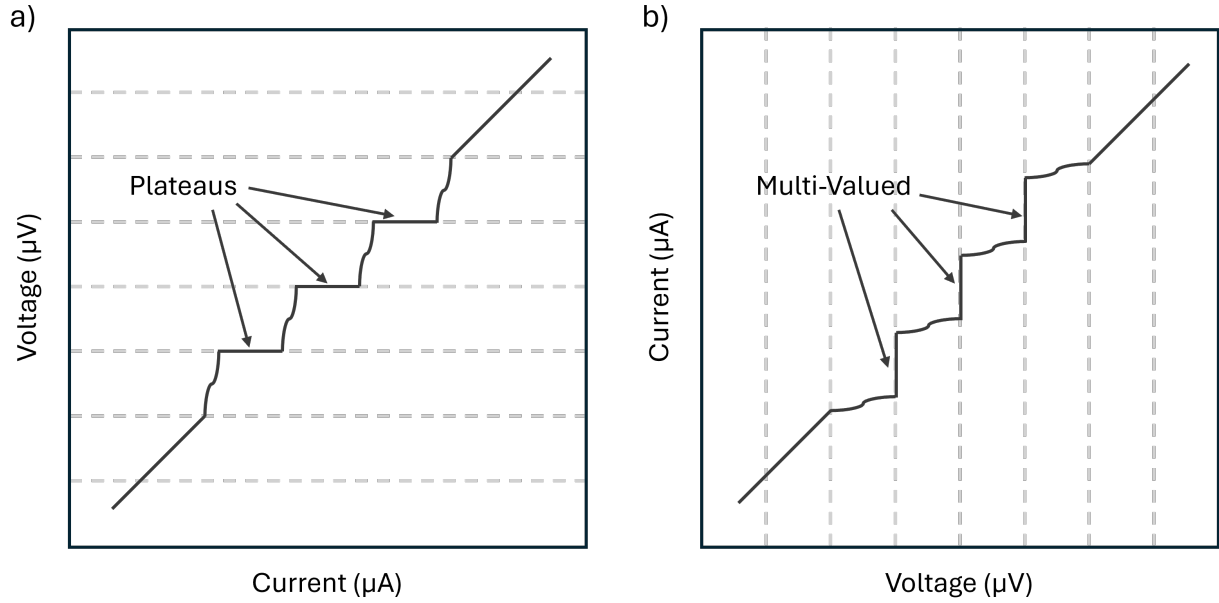
Figure A.3: Shapiro Steps plotted as V vs I and I vs V, showing that the current bias measurement (V vs I) results in a well defined single value function which is more easily measurable experimentally.

Figure A.4: Lock-in current-bias measurements utilizing a 1 MΩ resistor to set the current bias from the Lock-in voltage and the DC voltage source, resulting in the measurement of $\frac{dV}{dI}$ as a function of the DC current.

Figure A.5: Lock-in current-bias measurements utilizing a 1 MΩ resistor to set the current bias from the Lock-in voltage and the DC voltage source, resulting in the measurement of $\frac{dV}{dI}$ as a function of the DC current. Low-pass-filters and a sapphire board are used to thermalize the electrons.

down to the device. The attenuation of the signal is not an issue for our measurements, as we can simply increase the applied RF power from our RF generator to compensate for the loss from the attenuators. Unfortunately, there is one last issue to be solved; the attenuators present a short to ground, and therefore, the DC and Lock-in current will both be unintentionally shunted to ground. To remedy this, a 'DC block' can be used,

which is essentially a capacitor acting as a high-pass filter to block the flow of DC current. Fortunately, our low-pass filters will perform an analogous role for the RF signal, stopping it from traveling up the DC lines to our measurement equipment. Figure A.6 shows this setup schematically.
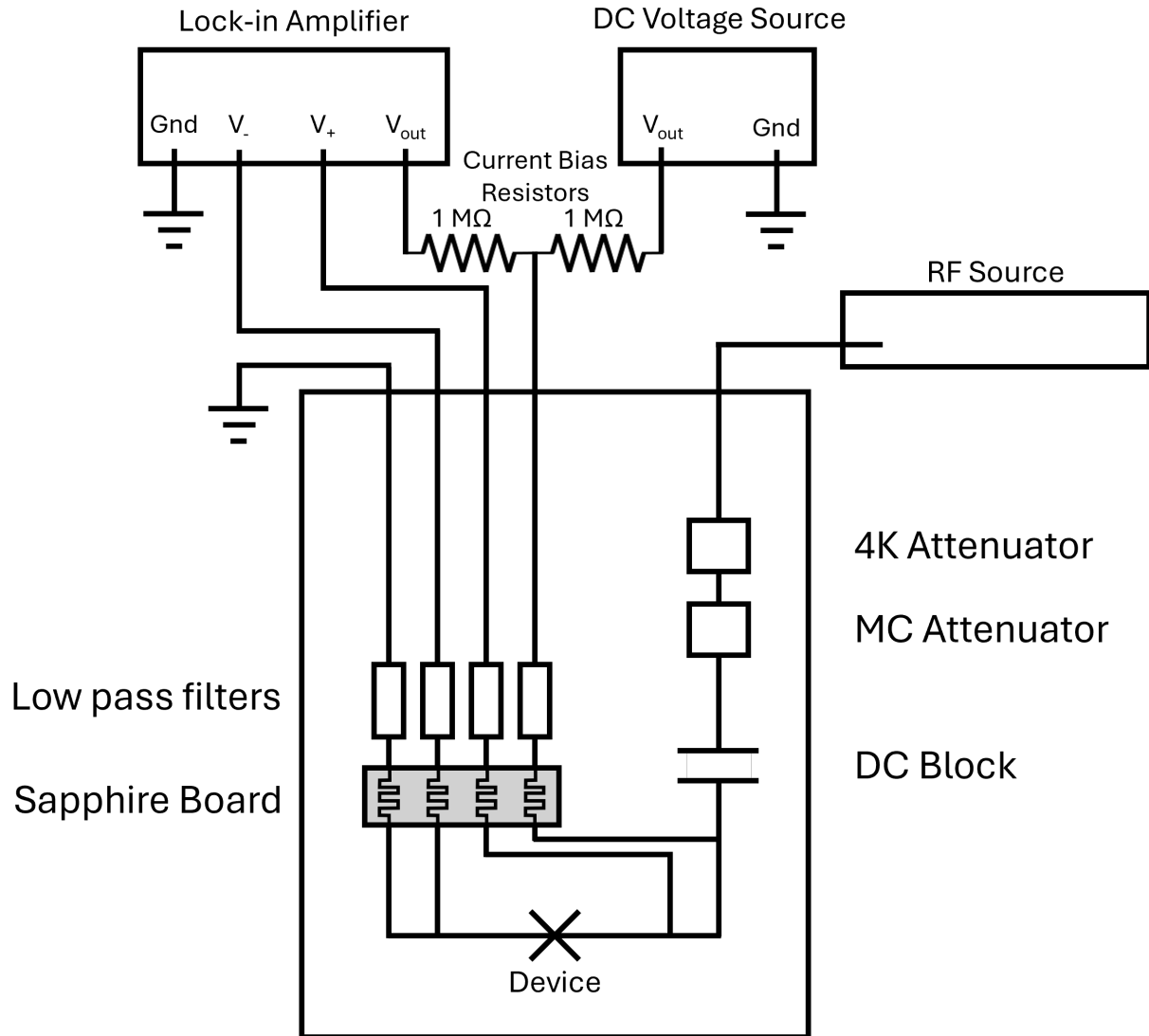
Figure A.6: Lock-in and DC current-bias measurements with the addition of a RF microwave source, resulting in the measurement of $\frac{dV}{dI}$ as a function of the DC current and RF irradiation (frequency and power). Low-pass-filters and a sapphire board are used to thermalize the electrons in the DC lines. RF attenuators are used to reduce the heating from the higher temperature plates through the RF lines. A DC block is used to stop the DC signal from being shunted to the attenuator grounds.

A.1.4 Magnetic Field and Superconducting Magnets

In order to measure Fraunhofer patterns in Josephson junctions, an external magnetic field is necessary. While there are many interesting and useful tips about using superconducting magnets properly, in new dilution refrigerators, this is mostly automated. Therefore, I will briefly touch on an intuitive picture that Rodney Snyder gave me when teaching me about superconducting magnets, which I think is useful for those who are unfamiliar. To understand acceptable ramp rates for superconducting magnets and why these ramp rates must be reduced at larger magnetic fields to avoid a quench, we must first think of power dissipation in the magnet. Power dissipation is simply $P = IV$, where for our supercon-ducting magnet $V = L\frac{dI}{dt}$. From this, we can see that our dissipated power is $P \propto I\frac{dI}{dt}$. Using the fact that we are measuring a solenoid where $B \propto I$, we can write this in terms of the magnetic field $P \propto B\frac{dB}{dt}$. Clearly, at higher magnetic fields, we should be careful to change the magnitude of the field more slowly. The acceptable rates are typically listed in the dilution refrigerator manual and are sometimes automatically limited by the control software.

A.2 Failed Devices

Below I will present a few failed devices which I believe are somewhat emblematic of the typical behavior seen in FeTeSe-based devices, which I hope will be of use to future students working on this material. In an attempt to make Josephson junctions using FeTeSe, a number of structures were fabricated. Graphene (Fig. A.7a) and Au (Fig. A.7b) weak links were attempted due to their long coherence lengths, however no Josephson effects could be realized, and the devices were very sensitive to destruction due to external currents or electrostatic discharge. To the best of my knowledge, to date, no one has fabricated a Josephson junction using FeTeSe with a weak link material successfully; all current studies use constrictions (Ref. [59]), vdW barrier (Ref. [61]), or a direct superconductor-superconductor

interface (this work). Despite this, with proper interfacial engineering, this could very likely be overcome, and I would not discourage anyone from attempting investigation in this direction.
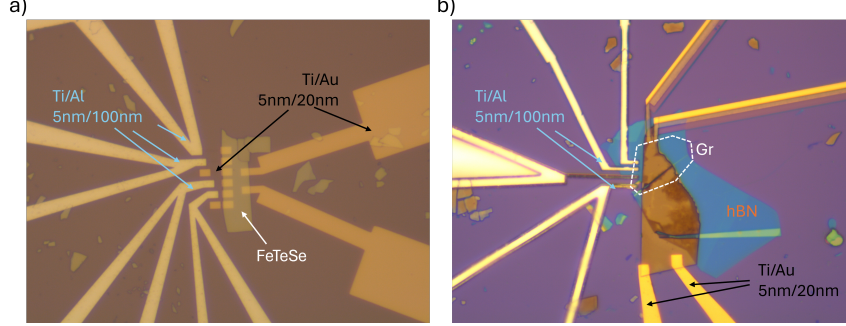
Figure A.7: a) An attempted FeTeSe-Au-Al Josephson junction. b) An attempted FeTeSe-Gr-Al Josephson junction.

I also fabricated multiple FeTeSe-FeTeSe devices; however, none of these devices reached a 0 resistance state at low temperature. Further, in one crossbar-shaped device (Ref. A.8a), even when only measuring the four-terminal resistance of one of the flakes, a finite resistance existed. Based on a number of FeTeSe flakes that were no longer superconducting when subject to stacking across an edge, strain-induced destruction of superconductivity seemed a likely mechanism. In an attempt to investigate this effect, I etched a trench in a Si/SiO_2 wafer and dropped a FeTeSe flake on top of the trench (Fig. A.8b). The idea was that by forming a capacitor between the FeTeSe and the conductive Si back gate, the electrostatic force would deform the FeTeSe, resulting in strain. Then, the resistance of the FeTeSe flake would be measured using a 4-probe method to determine if any changes were present. Unfortunately, there were no significant changes in the $\frac{dV}{dI}$ vs I curves when a ±32 V gate voltage was applied at 1.7 K (Fig. A.8c). If a future student were to recreate this experiment, it should be conducted closer to the critical temperature of FeTeSe so that the FeTeSe crystal would be more sensitive to environmental changes.
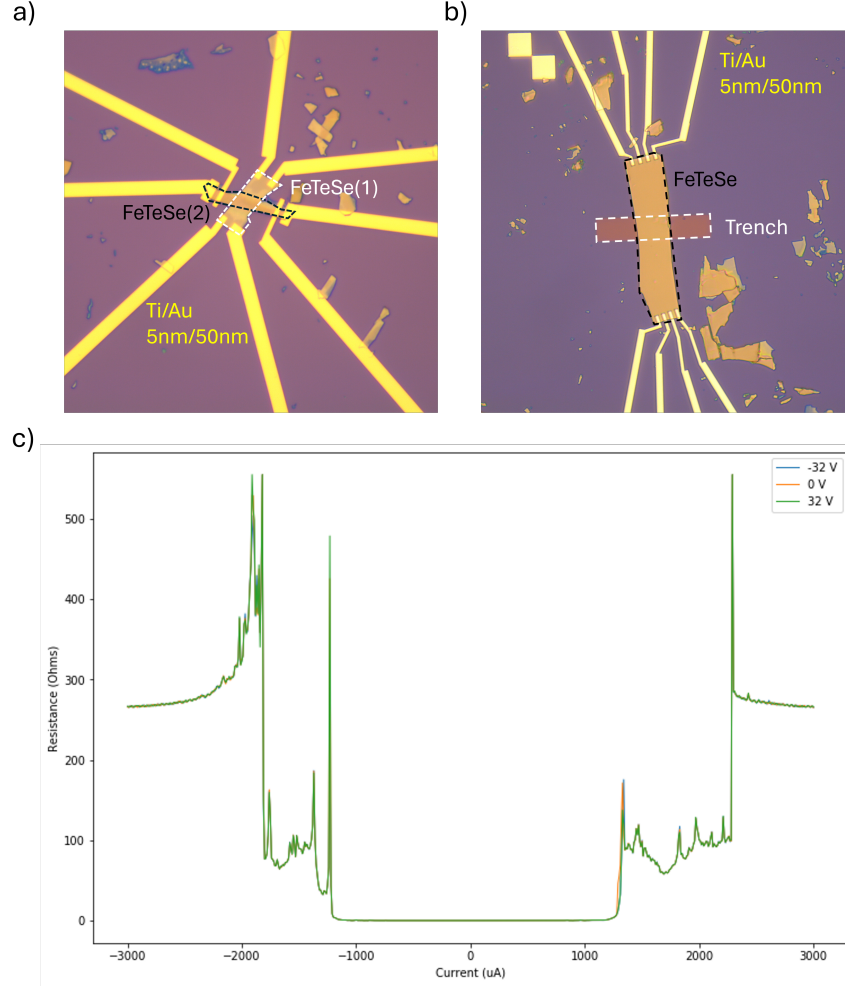
Figure A.8: a) An attempted FeTeSe-FeTeSe crossbar Josephson junction, which displayed no superconductivity in the top FeTeSe flake, potentially due to strain. b) A FeTeSe flake suspended over a SiO_2 trench, with the intent of applying strain through electrostatic gating. c) The resulting data from the strain device, showing no control effect at 1.7 K. If this experiment were to be repeated, the strain control near T_c should be easier to prove as a proof of concept.

A.3 Wire Bonding Tips and Tricks

Although wire bonding in high-volume industrial applications is automated and samples are fine-tuned for highly reliable bonding, researchers still rely on hand-controlled wire bonding to bond to varied samples, which are not finely tuned for completely reliable bonding. Due to this, wire bonding remains challenging and frustrating for many students struggling to connect their intended metals reliably. I have spent a significant amount of time wire

bonding for my own projects, as well as teaching a substantial number of students (in my own group and in other groups) who struggle with wire bonding and how to improve. I will not comprehensively cover all aspects of wire bonding (such as proper parameters for a given metal) as this is mostly covered in user manuals or basic training, but I will touch on some specific tips and tricks useful for making good connections in non-ideal conditions. My experience has been split between a wedge-type wire bonder and a ball-type wire bonder, and all of my tips apply to both.

Wire bond adhesion to uneven or non-clean surfaces is one of the major challenges students face when wire bonding. Typically, samples are adhered to a carrier using a polymer and, therefore, do not sit perfectly flat. This means that in the best-case scenario, only part of the wire is adhered to the pad. Furthermore, sample holders are often used multiple times and, for the sake of time, are not cleaned to the same standards as in industrial applications (such as plasma or laser cleaning). Additionally, devices are sometimes fabricated with atypical materials, resulting in relatively weak adhesion.

In order to increase the probability of a wire bond sticking, the minimum strain needs to be applied to the wire. Because the wire is being fed down the wire bonding tip nearly vertically but must effectively lay flat on the surface of the pad, moving the wire bonding tip only in the vertical axis will add stress to the connection with the pad. Therefore, in situations where bonding is difficult, a V-shaped descent/ascent will increase the likelihood of a bond sticking A.9. This needs to be done carefully, as the tip should never be dragged across the surface of the pad.

When wire bonds simply will not stick, no matter what is tried, there is a foolproof method to get them to stick; however, you do incur some risk of having to clean/rethread the wire-bonding tip. This method relies on the fact that when a bond fails, typically, some part of the wire does stick to the pad (particularly in the case of the first bond). Whether the surface is uneven, dirty, or not very adhesive, this leftover material has created an already adhered cushion of material that can be bonded toA.10. Sometimes this method
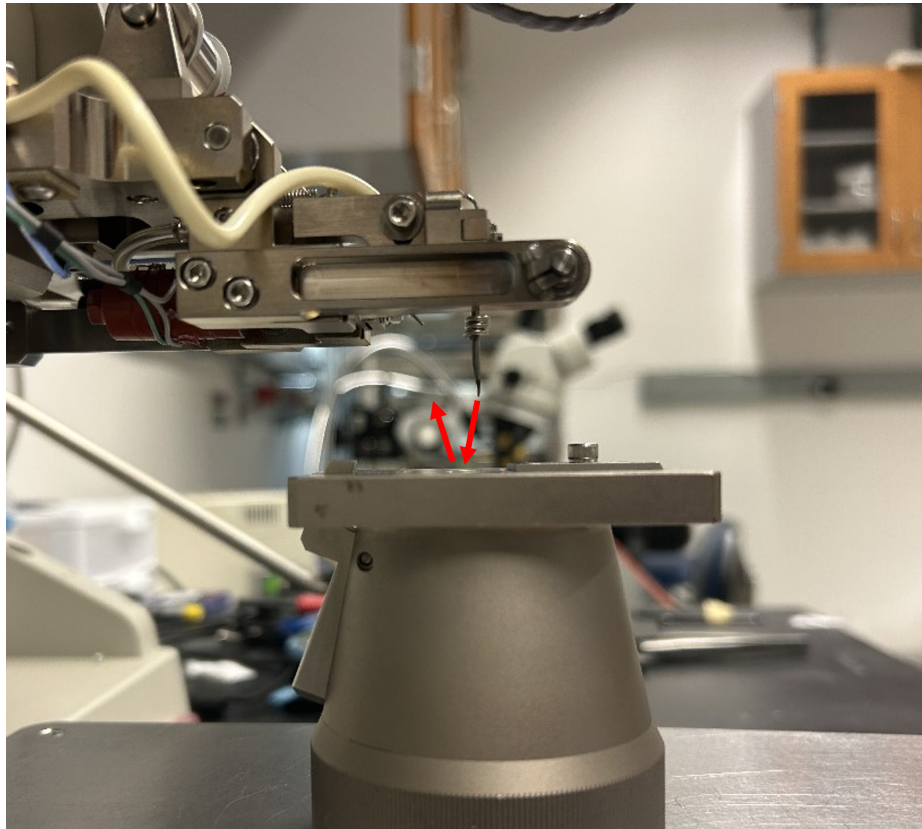
Figure A.9:   *Wirebonder V-shaped path of the tip.*

is not feasible, and if the operator of the wire bonder is not responsible for or capable of
cleaning/rethreading the wire bonder, this method should not be attempted.
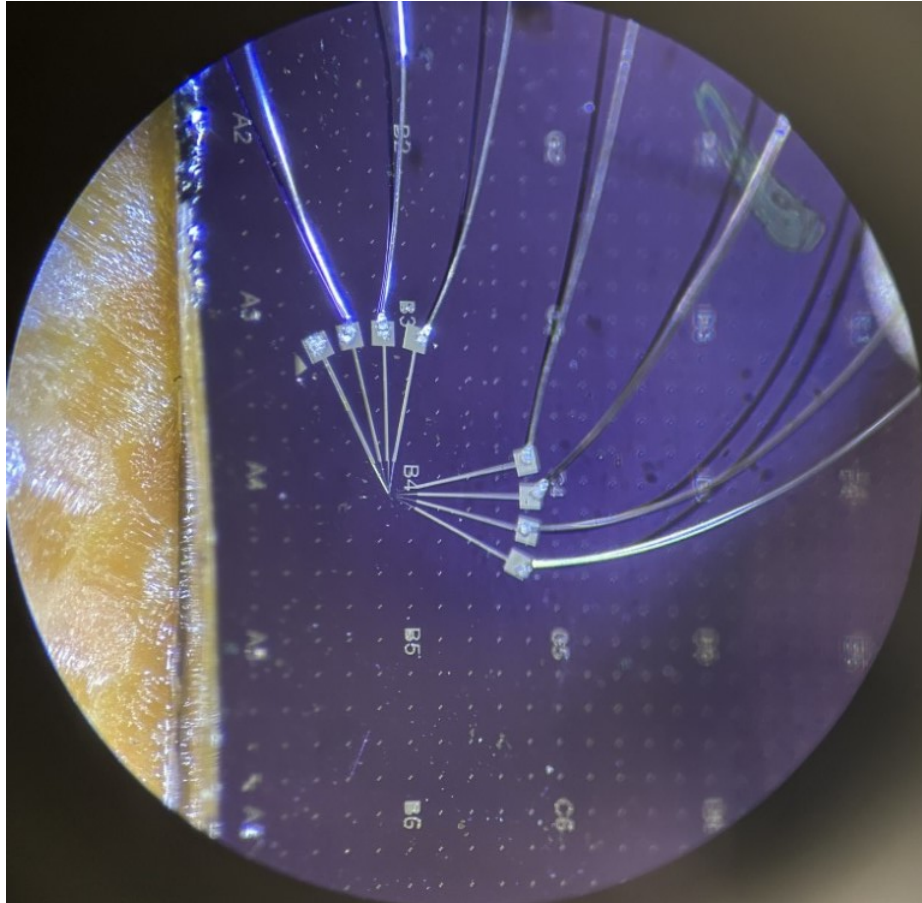
Figure A.10: *Wirebonder metal stuck to the bond pads which can be used for subsequent bonds.*

A.4   Data dump

Frequency of RF (GHz)	RF Power Range (dBm)	Magnetic Field Range (mT)	Figure
0.1	-75 to -15		A.12
0.2	-75 to -30		A.13
0.35	-75 to -25		A.14
0.4	-75 to -20		A.15
0.7	-50 to -12		A.16
0.8	-60 to -20		A.17
0.9	-60 to -10		A.18
1.2	-50 to -15		A.19
2.0	-55 to -22		A.20
3.0	-17.5 to 3.5		A.21
3.25	-12 to 5		A.22
3.45	-12 to 4		A.23
3.5	-20 to -1		A.24
3.7	-14 to 1		A.25
3.8	-14 to 1		A.26
3.9	-14 to 0		A.27
3.95	-15 to 2		A.28
4.0	-15 to 1		A.29
7.0	-9 to 4		A.30
0.5	-45	-2.5 to 2.5	A.31
0.8	-42.5	-2.5 to 2.5	A.32
3.55	-5	-2.5 to 2.5	A.33
3.55	-12 to 2	2	A.34
6.0	-10 to -2	10	A.35

Figure A.11:   A table of the parameters corresponding to the measurements displayed in the Data Dump Section. All data is from the same device measured in the main results section, and is taken over a current range of -6.6 μA to 6.6 μA.
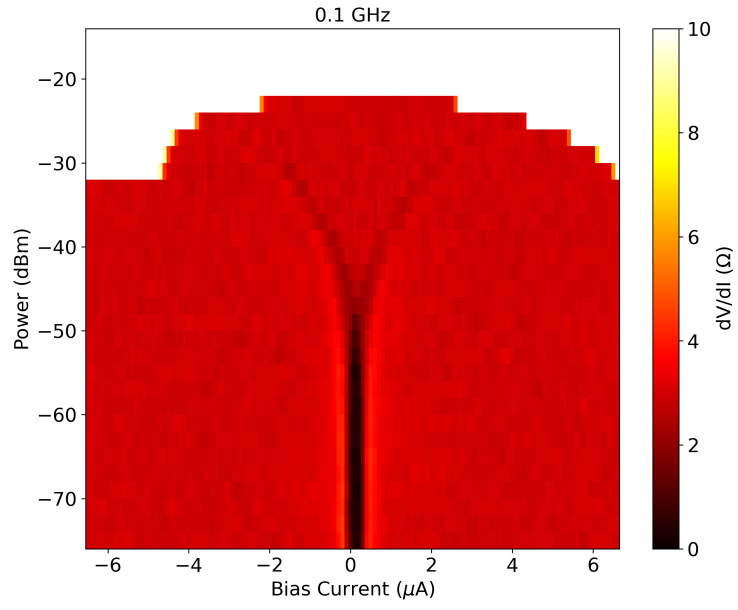
Figure A.12: $\frac{dV}{dI}$ vs I vs RF power at 100 MHz.
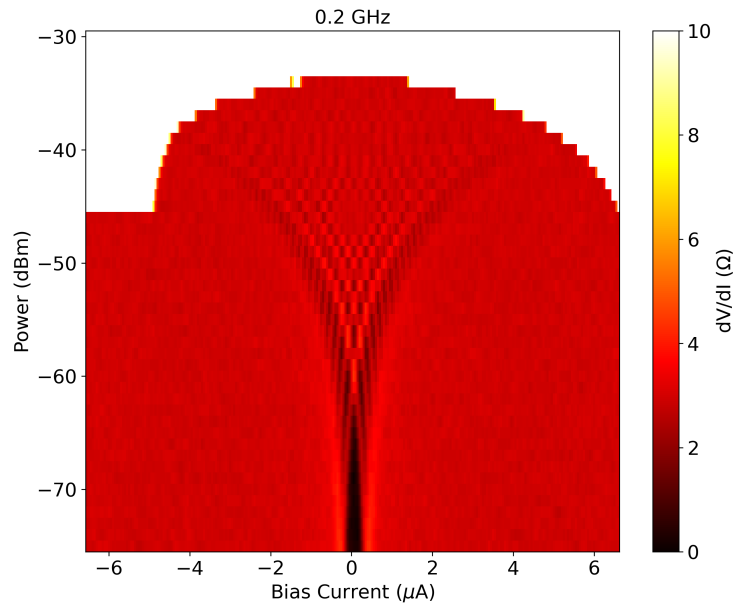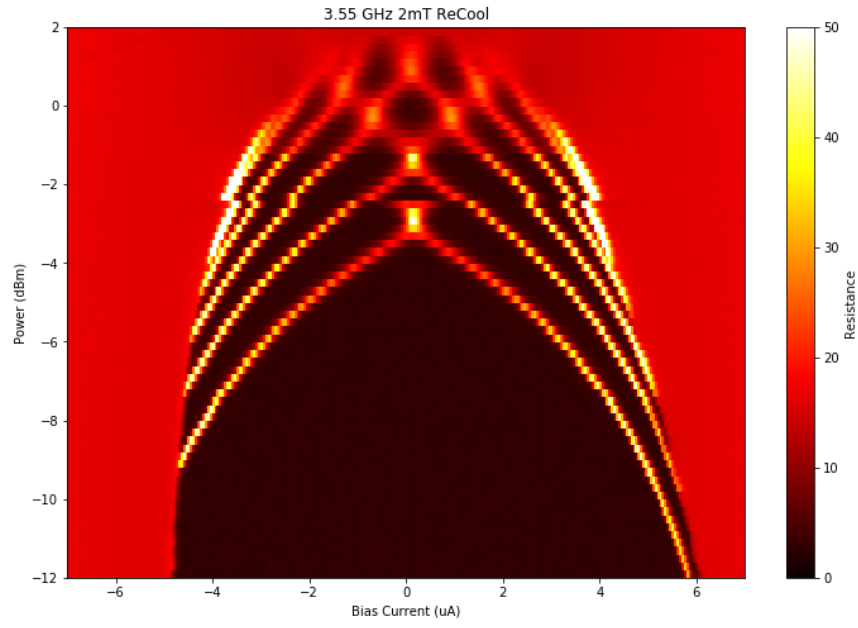

Figure A.13: $\frac{dV}{dI}$ vs I vs RF power at 200 MHz.
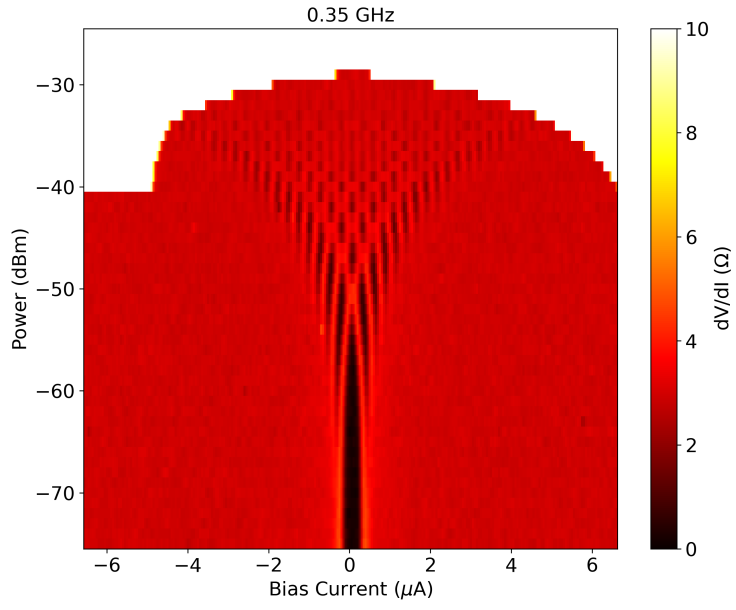
Figure A.14: $\frac{dV}{dI}$ vs I vs RF power at 350 MHz.
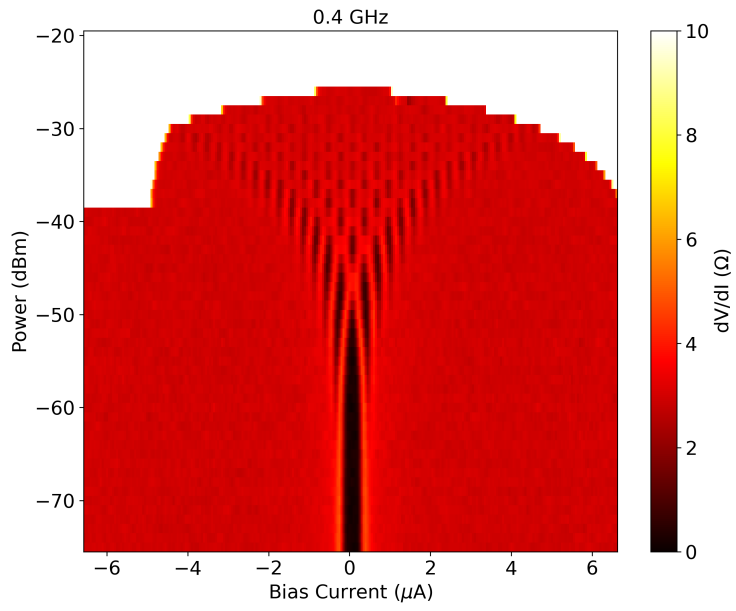
Figure A.15: $\frac{dV}{dI}$ vs I vs RF power at 400 MHz.
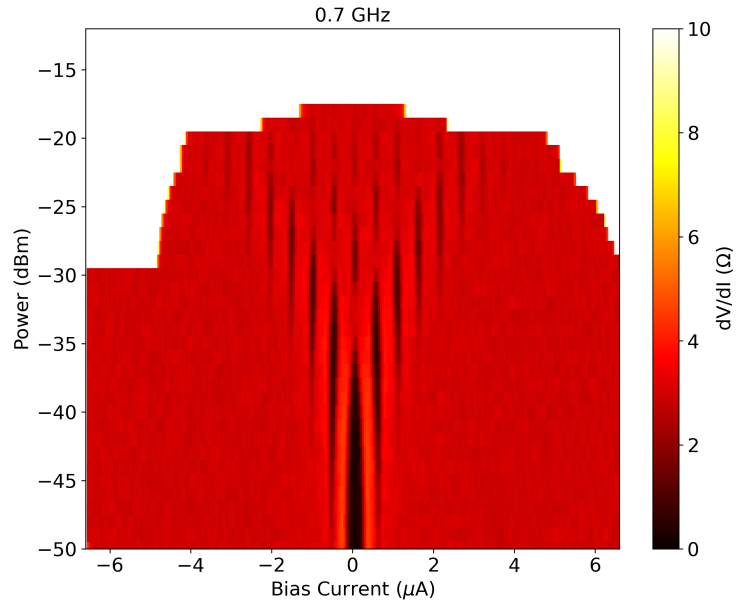
Figure A.16: $\frac{dV}{dI}$ vs I vs RF power at 700 MHz.
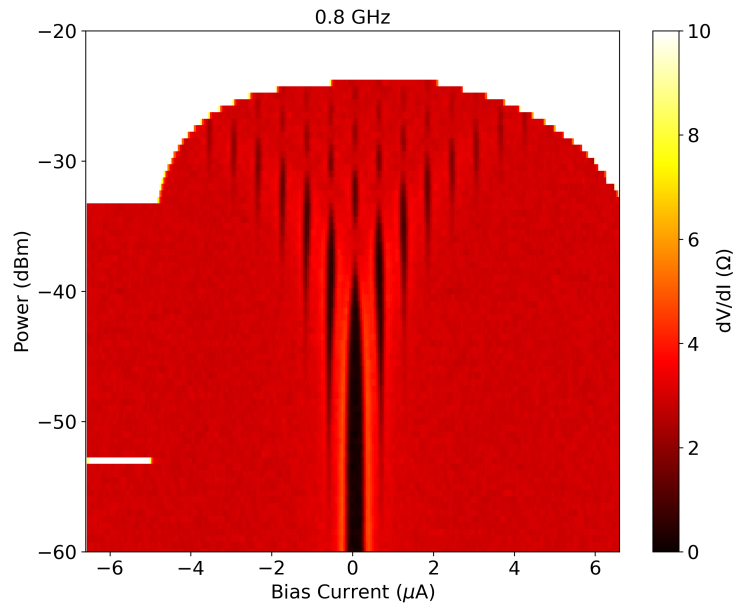
Figure A.17: $\frac{dV}{dI}$ vs I vs RF power at 800 MHz.
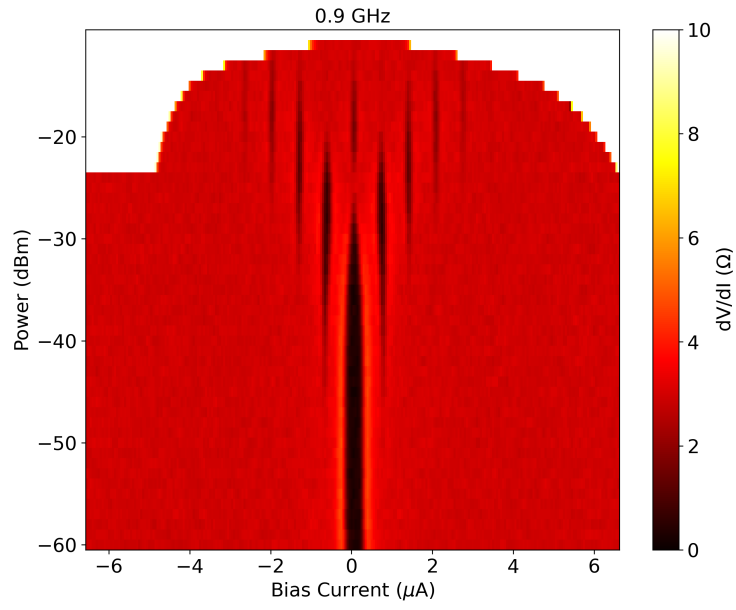
Figure A.18: $\frac{dV}{dI}$ vs I vs RF power at 900 MHz.
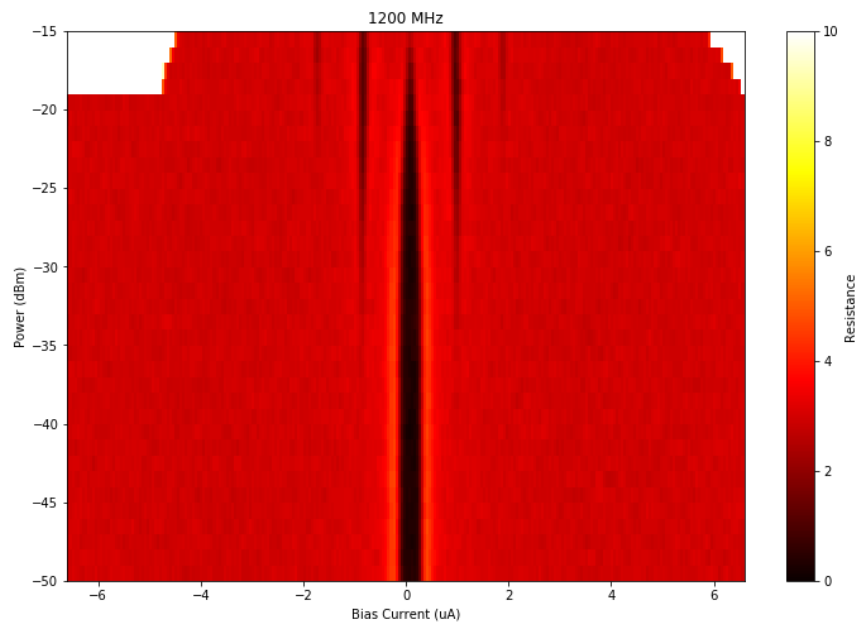
Figure A.19: $\frac{dV}{dI}$ vs I vs RF power at 1.2 GHz.

107
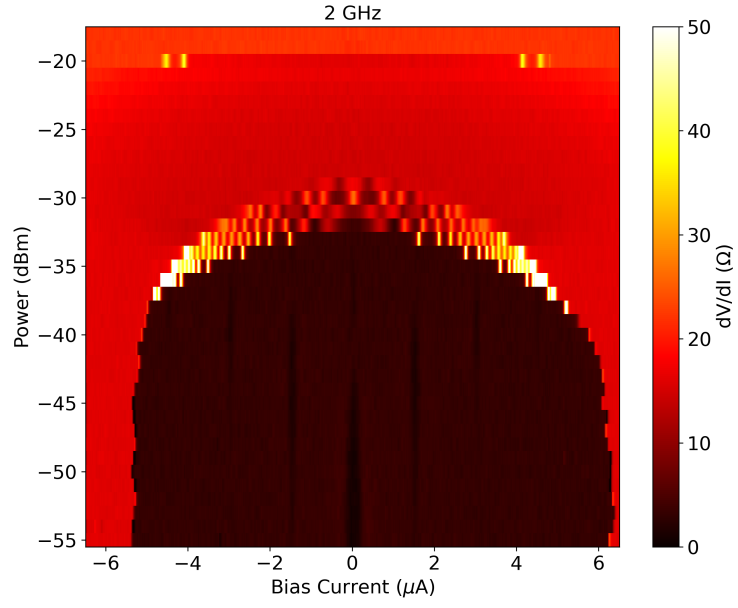
Figure A.20: $\frac{dV}{dI}$ vs I vs RF power at 2 GHz.
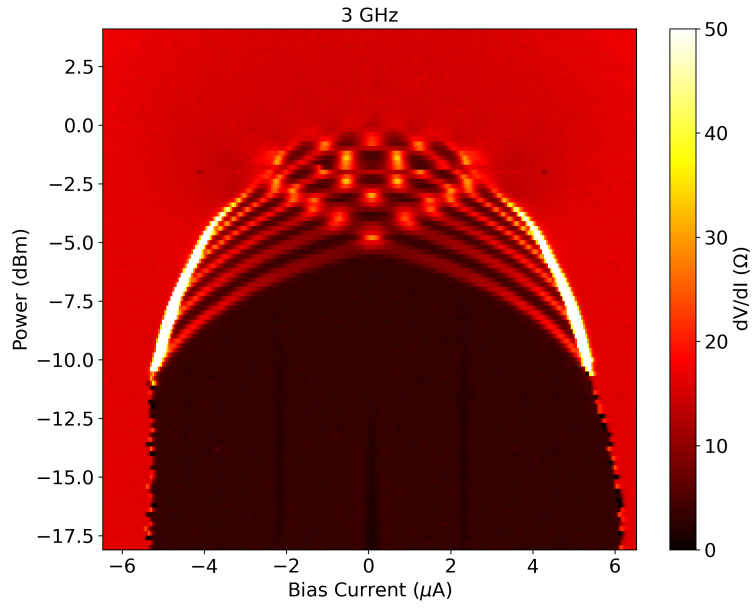
Figure A.21: $\frac{dV}{dI}$ vs I vs RF power at 3 GHz.
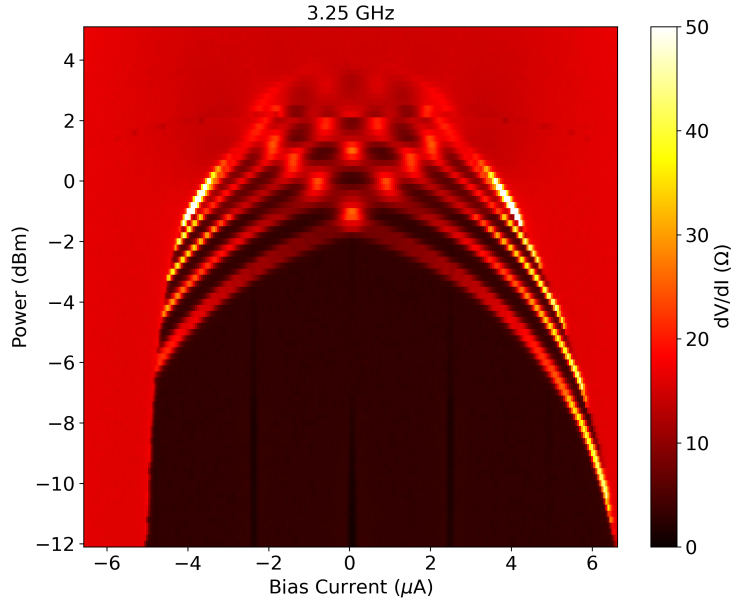
Figure A.22: $\frac{dV}{dI}$ vs I vs RF power at 3.25 GHz.
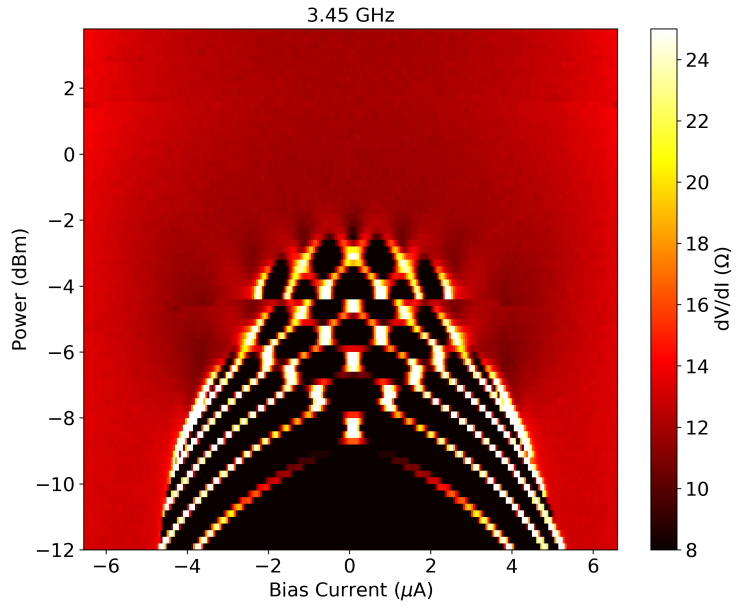
Figure A.23: $\frac{dV}{dI}$ vs I vs RF power at 3.45 GHz.
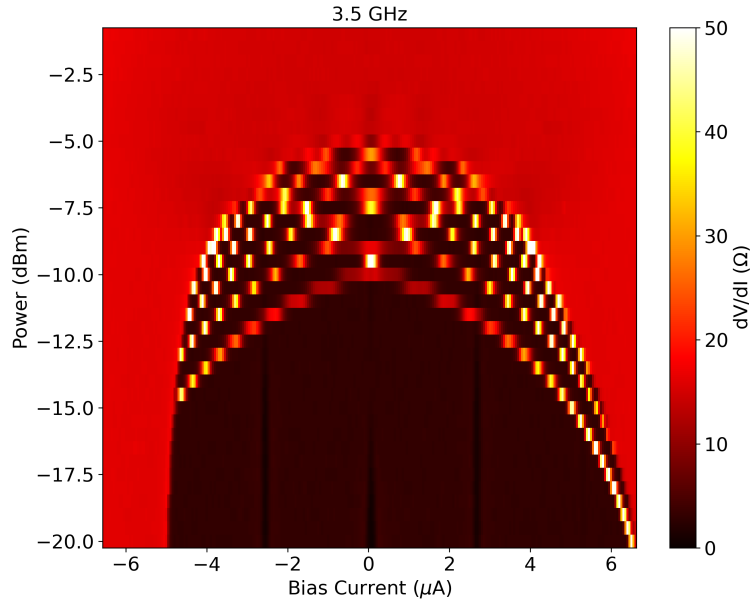
Figure A.24: $\frac{dV}{dI}$ vs I vs RF power at 3.5 GHz. In this map the jump shown in the main text is missing.
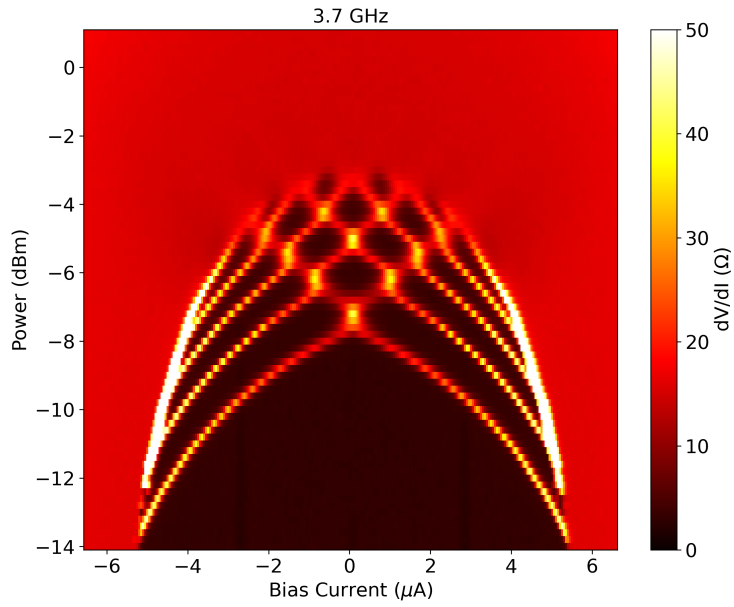
Figure A.25: $\frac{dV}{dI}$ vs I vs RF power at 3.7 GHz.
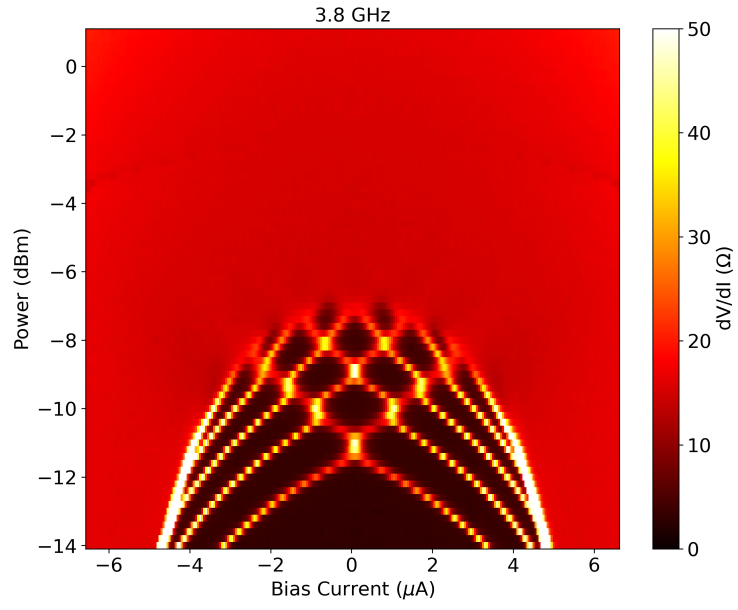
Figure A.26: $\frac{dV}{dI}$ vs I vs RF power at 3.8 GHz.
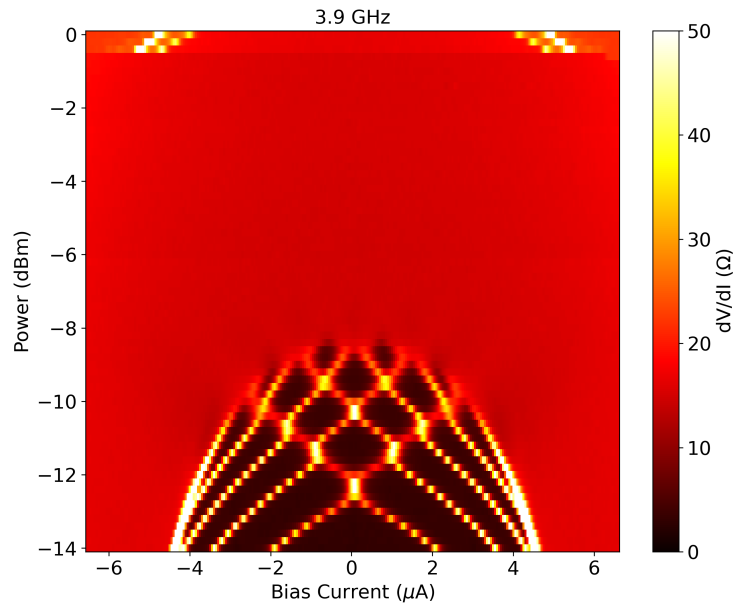
Figure A.27: $\frac{dV}{dI}$ vs I vs RF power at 3.9 GHz.
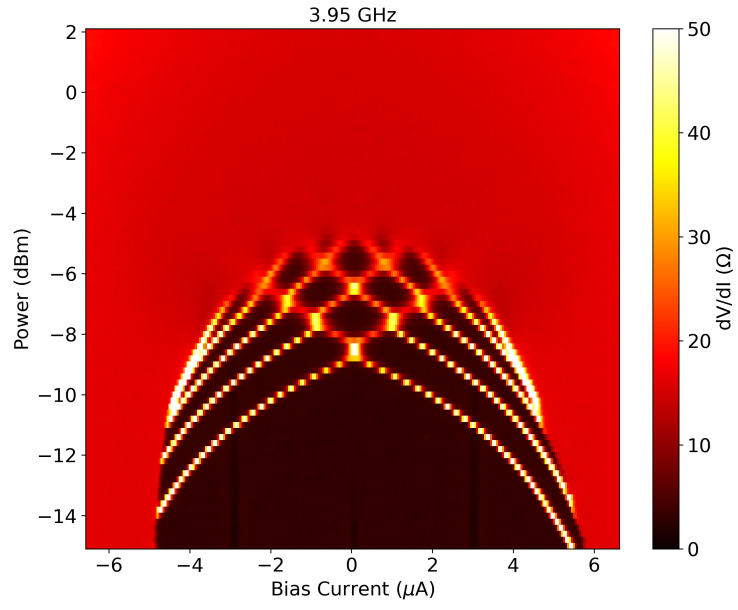
Figure A.28: $\frac{dV}{dI}$ vs I vs RF power at 3.95 GHz.
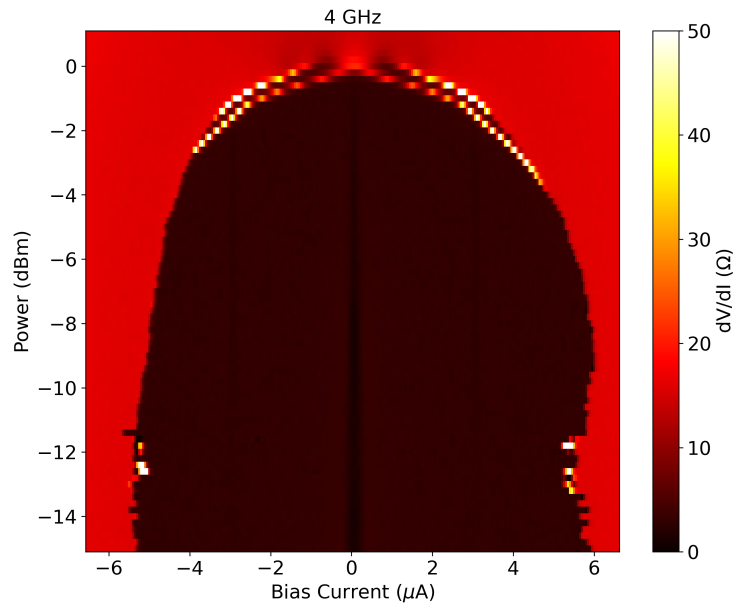
Figure A.29: $\frac{dV}{dI}$ vs I vs RF power at 4 GHz.
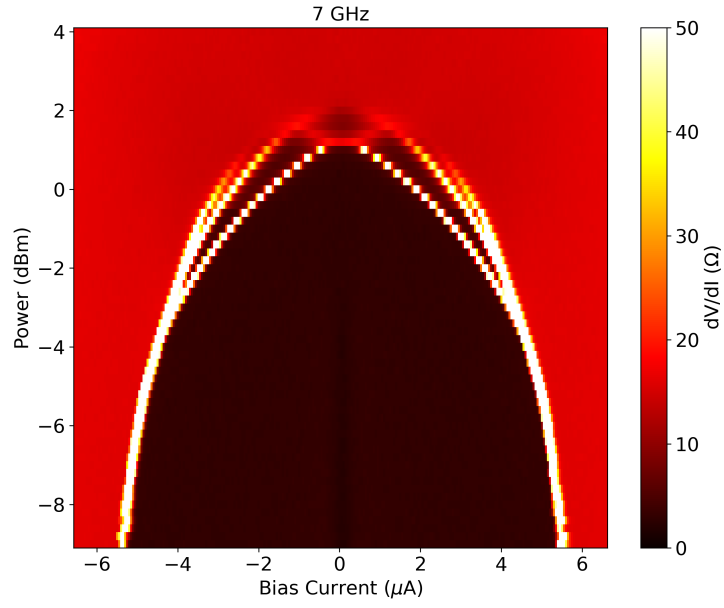
Figure A.30: $\frac{dV}{dI}$ vs I vs RF power at 7 GHz.
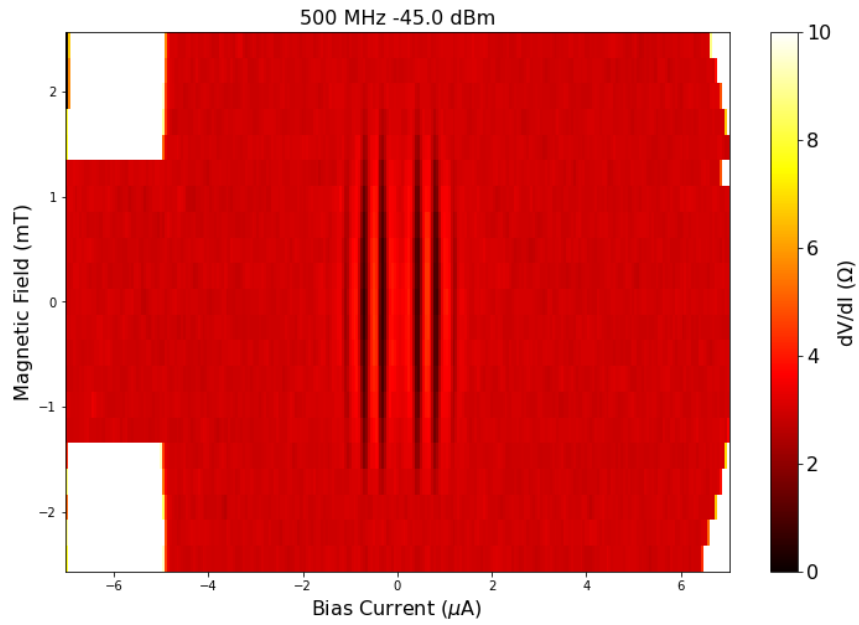
Figure A.31: $\frac{dV}{dI}$ vs I vs Magnetic Field at 500 MHz.

113
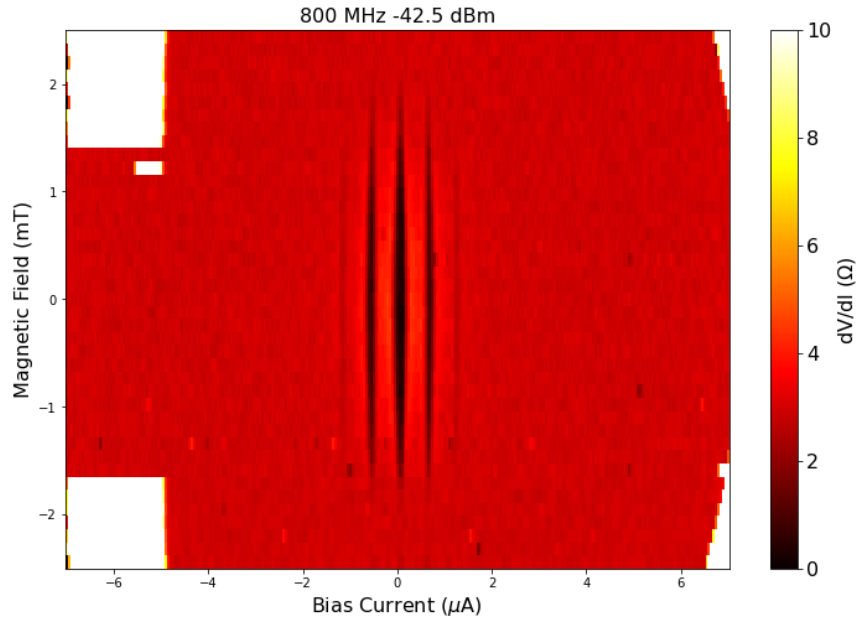
Figure A.32: $\frac{dV}{dI}$ vs I vs Magnetic Field at 800 MHz.
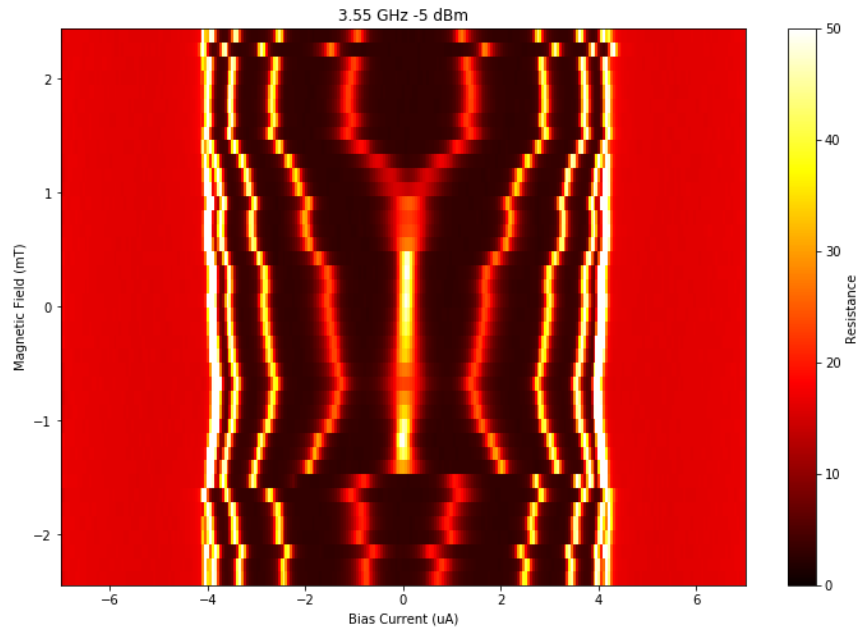
Figure A.33: $\frac{dV}{dI}$ vs I vs Magnetic Field at 3.55 GHz.

Figure A.34: $\frac{dV}{dI}$ vs I vs RF power at 3.55 GHz and 2 mT.
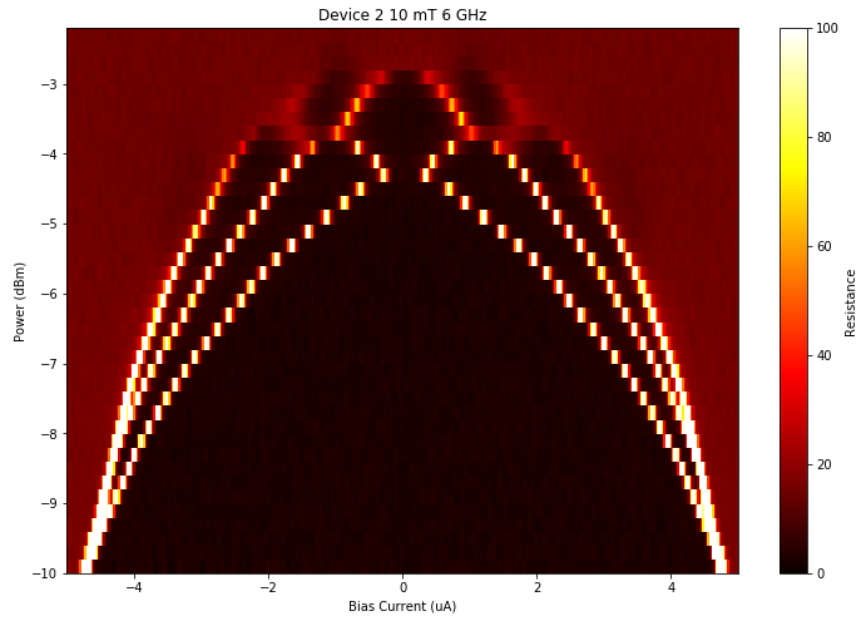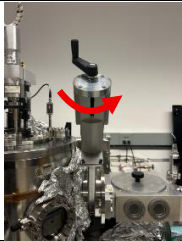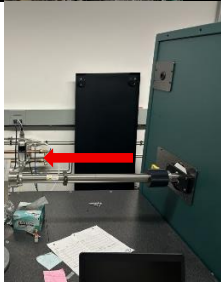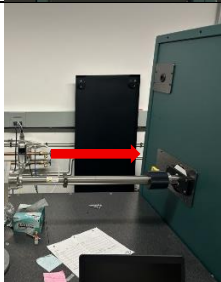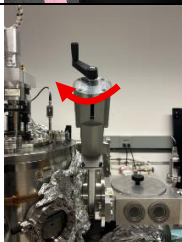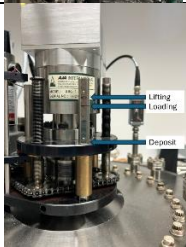
Figure A.35: $\frac{dV}{dI}$ vs I vs RF power at 6 GHz.

A.5 Depositions System SOPs

AJA Sputtering System

Loading a Sample

To begin, attach the sample to the holder using a carbon dot or a clamp.	
Vent the chamber by turning off the load lock pump.	
Once the turbo pump stops clicking, turn on the nitrogen gas.	
Load the sample; make sure the groove is facing towards the chamber.	
Turn the load lock vacuum pumps on.	

Once the pressure has reached the 10^{-7} mTorr range, open the load lock valve.	
Slide the loading arm into the chamber. Do not force it.	
Using the toggle stick below the computer, raise the mechanism from the Loading level to the Lifting level.	
Slide the loading arm out.	
Close the load lock valve.	
Lower the sample to the deposition height.	

Run the chosen program. Then reverse the steps to unload the sample. The steps are: raise the loading mechanism to the Lifting height, open the load lock valve, slide the arm in, lower the loading mechanism to the Loading height, slide the arm out, close the load lock gate valve, switch the pumps to LOAD LOCK, wait for the clicking to stop, open the nitrogen line, and unload the sample.	
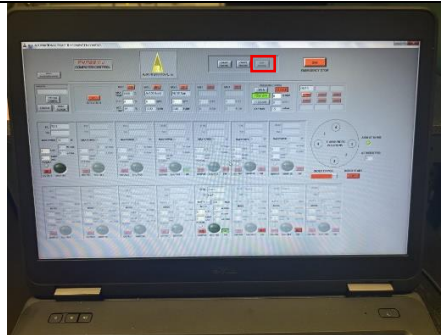
Running a Program

To run a program it is important that the cryo controller is in remote mode so that the computer can control the pressure in the chamber while the program is running. We will now show some examples of programs.

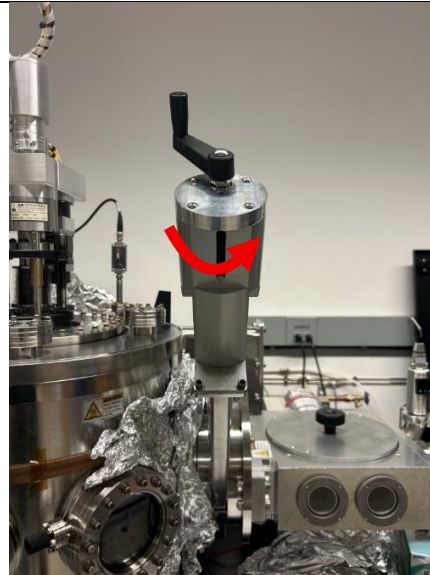|	
Each program is composed of individual layers, which can be customized.	
The initial layer for depositing a metal is a strike layer, which uses a 'high' pressure of 10 mTorr to light the plasma at a relatively low power of 60 W.	
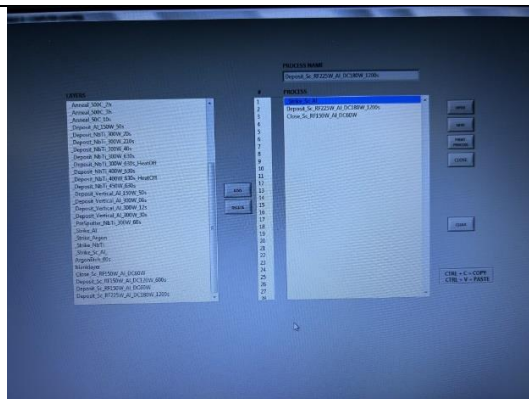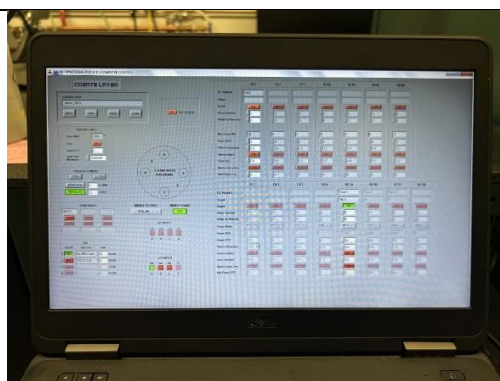
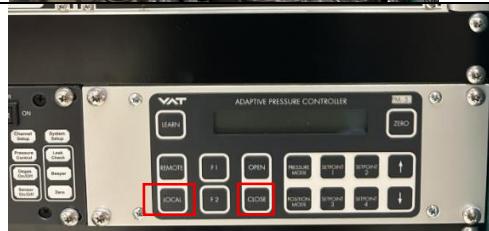|	
After this, a deposition layer can be defined, which uses the already lit plasma. A ramp up/down time of 210 seconds, a power of 300 W, and a pressure of 3 mTorr is typically used for the deposition of the metal. Shutter enable means the shutter will open after the ramp step. Coat time defines the time with the shutter open when the metal is deposited.	
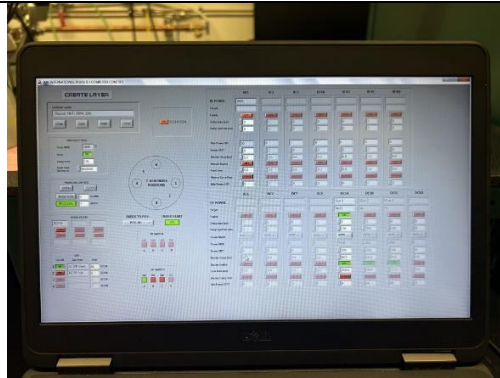
Exchanging a Target

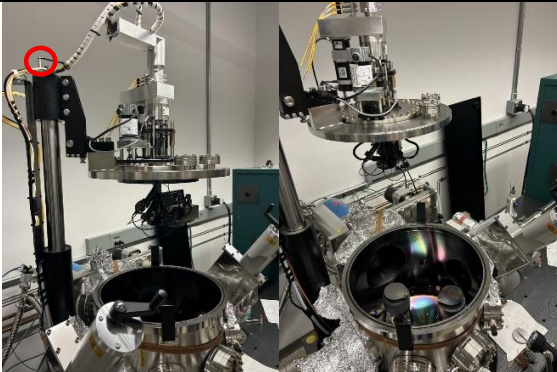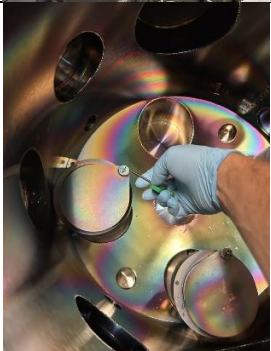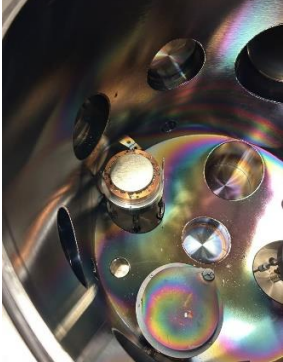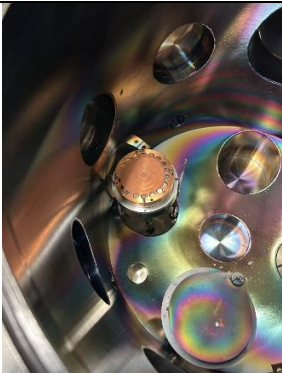|	
Venting the Chamber: The load lock should already be pumped. If not pump the load lock then open the load lock valve to the main chamber.	
Change the vacuum controller to local and close the cryopump.	
Turn off the load lock pump and wait for the turbo to stop clicking.	
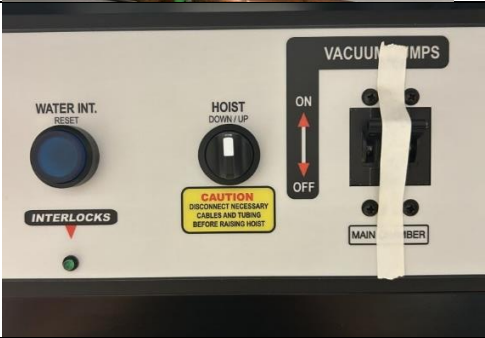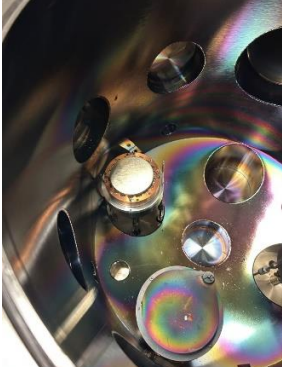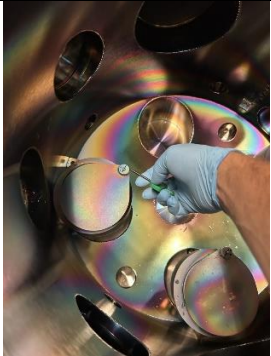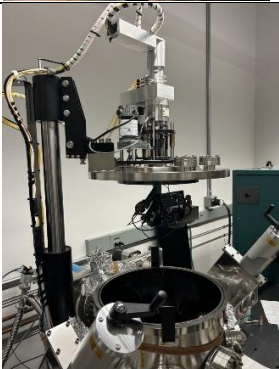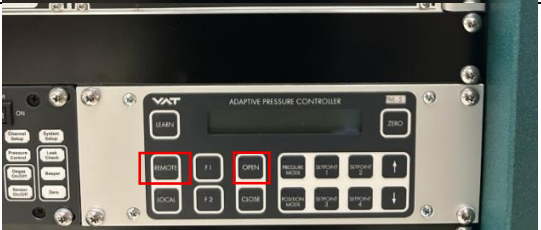
Open the nitrogen valve to vent the chamber.	
Turn the hoist in the up direction until the top of the chamber is at the maximum height.	
Pull the metal pin from the top of the hydraulic arm and rotate the top of the chamber out of the way.	
Remove the shutter by unscrewing the screw on the side.	

Unscrew the two screws clamping the chimney to the anode.		
Slide the anode off of the gun, it may take some wigging if the shutter arm is stuck.		
Partially unscrew the four screws holding the clamp down to the sputtering target. Rotate the clamp and lift it off the target.		
Remove the target.		

It is recommended to replace the copper mesh whenever loading a new target. Also vacuum away any metal flakes.	
Load the new target.	
Fasten the clamp on top of the target using the star pattern.	
Slide the anode and chimney in place and fasten the screws.	

Reattach the shutter, confirm that it rotates to the correct position by operating it manually from the PC.	
Return the chamber top to its original position, put the pin back in place, and close the chamber using the hoist controller.	
Pump the chamber using the load lock pumps.	
When the chamber is in the low 10^{-6} mTorr range, open the cryopump and close the load lock valve.	

Dual Sputtering

Dual sputtering can be achieved using 1 RF source and 1 DC source. The system only has 1 DC source that is switched between guns. If both are active in the same program, the DC portion will always run first. To run simultaneously, set the DC source's coat time to 0 and the RF source's coat time to the intended value. This also applies to lighting the plasma.	
After lighting the plasma, the deposition can be run with the same logic. It is important that both 'shutter enable' and 'shutter carry over' are on for the DC source, so the shutter does not close when the RF portion executes.	
The final program step simply closes the shutters.	
As far as aligning the two guns for dual sputtering. The angle of the gun can be adjusted by the black knob on the bottom of the gun.	
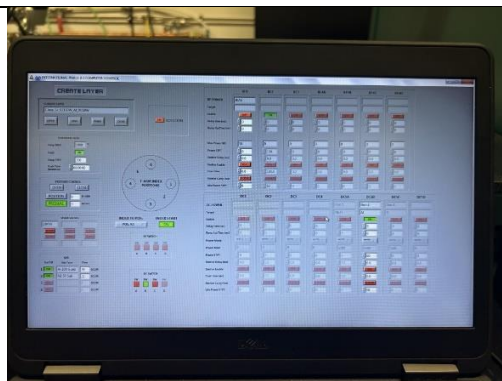
Annealing

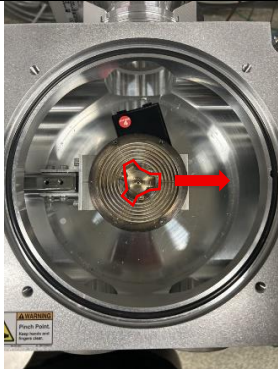Annealing programs are very simple and do not require an in depth description. Needless to say ramps steps can be included if there is a preferred rate of heating and cooling. One very important note: never run a deposition without the sample puck loaded in the chamber. This will coat the quarts window which separates the sample puck from the heater. If this becomes coated most of the radiative heat will be reflected and the heater will immediately turn off. If there is ever an issue with the temperature control, this is an easy thing to check.

Arcing Issues
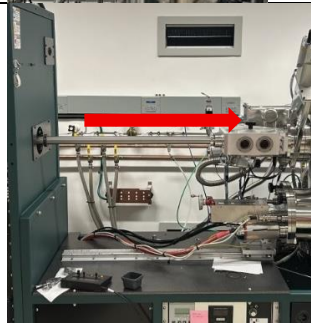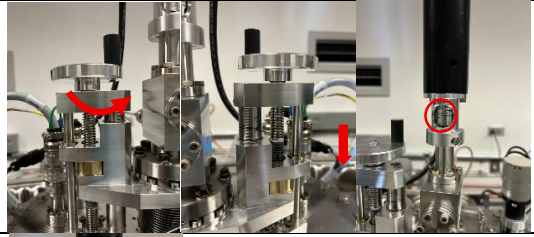
I spent a large number of hours trying to address the arcing issues in the sputtering system. Built up material on the anode and cathode was cleaned by bead blasting, RF sputtering was used to remove any oxide on the surface, and large portions of the gun were disassemble and cleaned to try to remove any metal flakes that could be causing the arcing. Ultimately a simple solution was found. `Conditioning' of the target was necessary, which involves using a very low power plasma of 60 W for many hours (typically more than 4 hours), and then slowly increasing the power and repeating the process. This effectively stops the arcing issues and is much wasier than any of the other methods listed above.
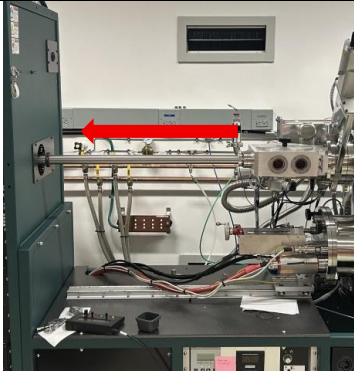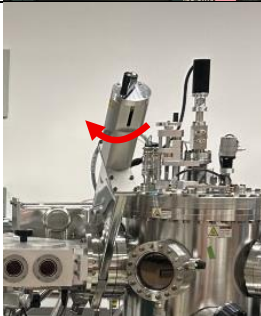
AJA Electron Beam Deposition System

Loading a Sample
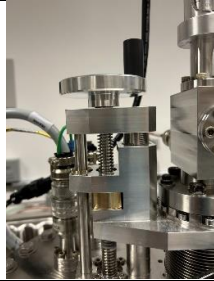
To begin, attach the sample to the holder using a carbon dot or a clamp.	
Vent the chamber by turning off the load lock pump.	
Once the turbo pump stops clicking, turn on the nitrogen gas.	
Load the sample; make sure one of the three grooves is facing into the chamber.	
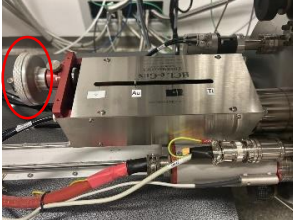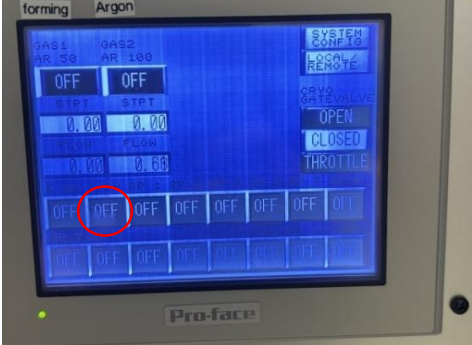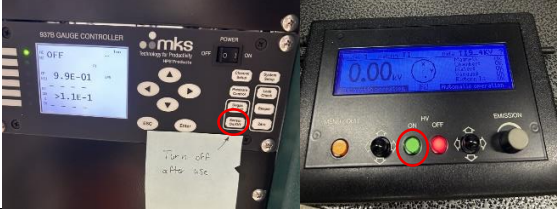
Turn the load lock vacuum pumps on.	
Once the pressure has reached the 10^{-7} mTorr range, open the load lock valve.	
Slide the loading arm into the chamber. Do not force it.	
Lower prongs into grooves of sample holder. Look through optical port to make sure they are aligned properly (they should be aligned when the circle crawn on the rotation control aligns with the circular opening)	
Rotate the rotation control rod until the prongs have been rotated underneath the lip of the grooves. A small amount of resistance will be felt at this point.	
Lift the sample back up to the 10 mark.	
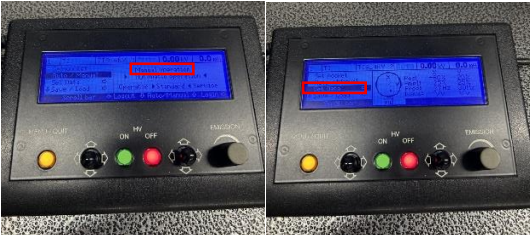
Slide the loading arm out.	
Close the load lock valve.	
Deposit metals. Then reverse the steps to unload the sample. The steps are: open the load lock valve, slide the arm in, lower the loading mechanism until the sample holder touches the loading arm, rotate the rotation controller to align the circle with the opening, lift the prongs up, slide the arm out, close the load lock gate valve, switch the pumps to LOAD LOCK, wait for the clicking to stop, open the nitrogen line, and unload the sample.	

Depositing Metals

Load the samples according to the method shown above. Deposition takes place at a height of 10, as marked on the loading mechanism.	
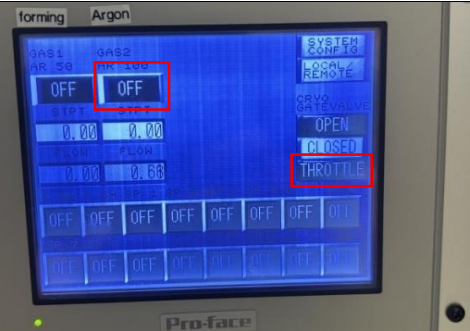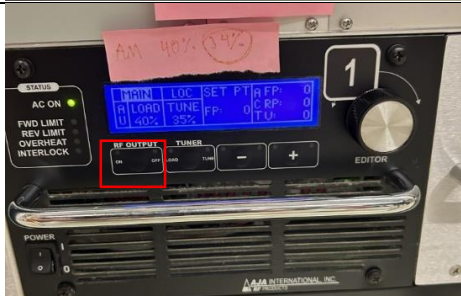
Move the prong to align with the intended metal by rotating the knob.	
Select the metal and the thickness in the control software. To do this select Process Menu (scroll to the intended metal) > Edit > Edit > (scroll to final thickness) Edit > Scroll to intended final thickness > To Main	
Make sure the shutter is closed. (ignore the cryo gate valve status shown in the picture, it should be open)	
Turn on the pressure sensor and the high voltage.	
Select start.	

Increase the emission until the beam is visible through the reflection off of the glass slide (see through the front optical port). Typically corresponding to 5%.	
Adjust the position as needed, manual mode is necessary here.	
Increase the emission until the desired rate is achieved. (2 A/s or higher for better liftoff)	
Zero the thickness and open the substrate shutter at the same time.	
When the desired thickness is reached turn off the substrate shutter. The power will ramp down automatically, if you had the controller in Automatic mode, otherwise ramp down the power by hand. Let the system cool for 5 mins.	
Unload or deposit other metals.	

Argon Etch

The chamber should be pumped with a sample loaded. The cryopump should be	
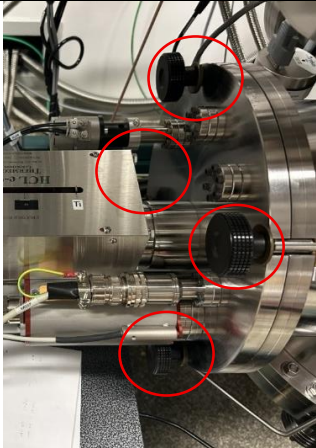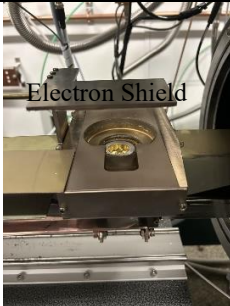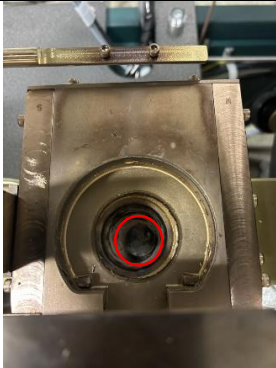
open. This is typically done as a precleaning step to ensure better electric contacts.	
Set the Argon flow to 45 SCCM. This results in a pressure of 30 mTorr.	
Open the Argon flow. Click throttle on the cryo controller.	
The forward power should be set to 50 W. Turn on the RF output. If there is an issue, check the load and tune values. Manually setting these to 40% an 34% should solve the issue.	
Decrease the flow rate to 4.5 SCCM. This corresponds to 3 mTorr.	
Wait the desired time. Between 5 s and 60 s is typical for making good contacts depending on whether some damage at the interface is harmful to the	
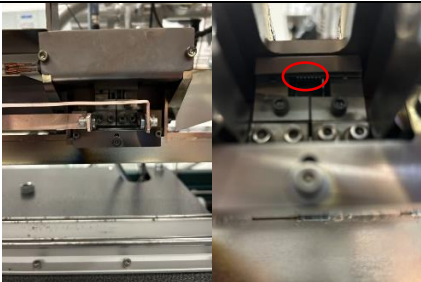
device. Longer runs can be used as etches, etch rates of 0.3-0.5 nm/min were seen for some 2D materials such as hBN. Etches longer than 15-20 mins hard baked the PMMA.	
Turn off the RF power.	
Turn off the gas flow.	
Open the cryo gatevalve.	

Misc. Accessible Through the Gun Port

Crucibles: To access the crucibles, first close the cryo gate valve, and vent the chamber through the load lock, as has been described previously in regard to the Sputtering system.	

Unscrew the four clamping knobs.	
Slide the crucible holder out. The crucible will be visible now. Above the crucible can be seen the electron shield installed by Rodney Snyder. It is meant to catch stray electrons from the electron beam that would hit the sample. This stray current can be measured through the electrodes for the Argon etch plasma.	
The gold crucible has a carbon spacer beneath it, which allows more of the energy of the electrons to be lost in the crucible. and therefore decreases the required power to melt the Au. This helps with liftoff.	
Before loading more gold a piranha etch of the gold pellets is necessary to ensure they are sufficiently clean and free of carbon contaminants. Be EXTREMELY careful when performing a piranha etch. This solution aggressively dissolves organics and is dangerous. If combined in the wrong order the solution will explode. Please refer to an external source for a safe and effective piranha etch procedure.	
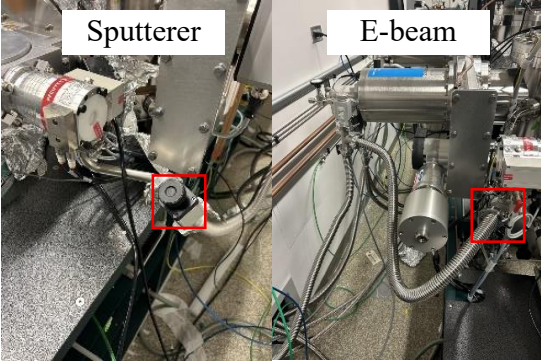
Filament: The filament can also be accessed by opening the chamber this way, and will occasionally need replacing. The filament can be seen here. AJA will provide technical notes on replacing the filament.	
Thickness Sensor: Additionally, the deposition rate monitor can be accessed this way, and is shown through the optical port. Additional sensors can be found in the holder.	
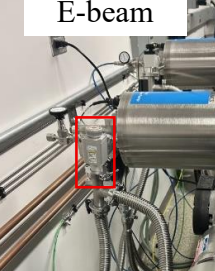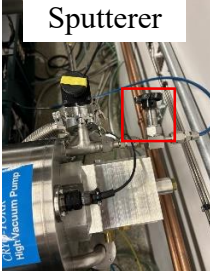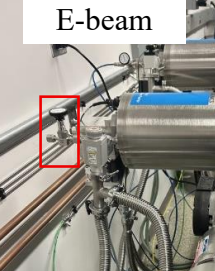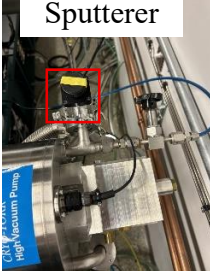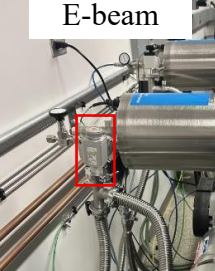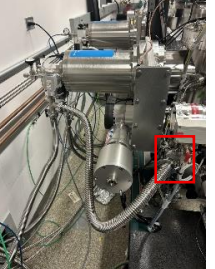
Pneumatics

During gas outages there can be an issue with the pneumatics used to control the gate valve for the e-beam deposition system. When this happens the pneumatics get stuck in an intermediate position between ON and OFF. Typical pressures cannot solve this issue. However, this issue can be relatively easily solved by increasing the pressure from the air coming from the wall temporarily until the pressure is sufficient to return the cryopump gate valve to normal operation. Afterward the pressure should be reduced again.
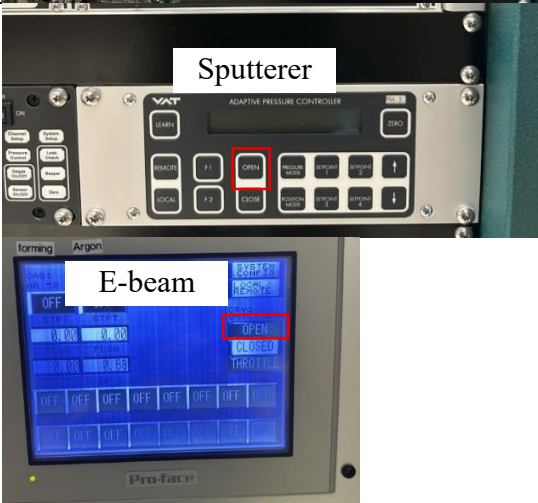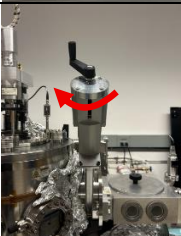
Both Systems

Regenerating the Cryopump

Close the gate valve to the cryopump, and turn off the cryopump. Wait for it to reach room temperature. (A few hours)	
Turn off the vacuum pumps for the load lock.	
Unplug the turbo pump cable from the back of the controller.	
Close the small valve connecting the roughing pump to the turbo pump and load lock.	

Turn on the roughing pump to pump the line.	
Slowly open the valve connecting the roughing pump to the cryopump until it is fully open. Wait for 10 mins.	Sputterer E-beam
Close the roughing pump valve and open the valve to the nitrogen line (move the nitrogen line if connected to the other cryopump). Once the over-pressure valve hisses, close the nitrogen line.	Sputterer E-beam
Slowly open the valve connecting the roughing pump to the cryopump until it is fully open. Wait for 10 mins.	Sputterer E-beam
Repeat the two steps above two times.	
Turn the cryopump back on.	
Reattach the roughing pump line to its original position, and open the small valve connecting the roughing pump to the turbo pump and load lock.	

Plug the power cable for the turbo pump back in.	
Use the load lock pump to pump the main chamber while the cryopump cools.	
Once cold head is at base temperature (12-15 K), open the cryopump gate valve.	Sputterer E-beam
Close the load-lock gate valve	

Bibliography

1. Tinkham, M. *Introduction to Superconductivity: Second Edition* ISBN: 9780486435039. `https://books.google.com/books?id=JOQoAwAAQBAJ` (Dover Publications, 2004).

2. Onnes, H. Further experiments with liquid helium. *Comm. Phys. Lab. Univ. Leiden* **2,** 120–124 (4 1911).

3. Meissner, W. & Ochsenfeld, R. Ein neuer Effekt bei Eintritt der Supraleitfähigkeit. *Naturwissenschaften* **21,** 787–788. ISSN: 1432-1904. `https://doi.org/10.1007/BF01504252` (44 1933).

4. Hsu, F.-C. *et al.* Superconductivity in the PbO-type structure α-FeSe. *Proceedings of the National Academy of Sciences* **105.** doi: 10.1073/pnas.0807325105, 14262–14264. `https://doi.org/10.1073/pnas.0807325105` (38 Sept. 2008).

5. Kamihara, Y., Watanabe, T., Hirano, M. & Hosono, H. Iron-Based Layered Superconductor La[O1-xFx]FeAs (x = 0.05-0.12) with Tc = 26 K. *Journal of the American Chemical Society* **130.** doi: 10.1021/ja800073m, 3296–3297. ISSN: 0002-7863. `https://doi.org/10.1021/ja800073m` (11 Mar. 2008).

6. Novoselov, K. S. *et al.* Electric Field Effect in Atomically Thin Carbon Films. *Science* **306.** doi: 10.1126/science.1102896, 666–669. `https://doi.org/10.1126/science.1102896` (5696 Oct. 2004).

7. Peierls, R. *Quelques propriétés typiques des corps solides* in *Annales de l'institut Henri Poincaré* **5** (1935), 177–222.

8. Landau, L. D. Zur Theorie der phasenumwandlungen II. *Phys. Z. Sowjetunion* **11,** 26–35 (545 1937).

9. Mermin, N. D. & Wagner, H. Absence of Ferromagnetism or Antiferromagnetism in One- or Two-Dimensional Isotropic Heisenberg Models. *Physical Review Letters* **17,** 1133–1136. `https://link.aps.org/doi/10.1103/PhysRevLett.17.1133` (22 Nov. 1966).

10. Böhmer, A. *et al.* Origin of the Tetragonal-to-Orthorhombic Phase Transition in FeSe: A Combined Thermodynamic and NMR Study of Nematicity. *Physical Review Letters* **114,** 27001. `https://link.aps.org/doi/10.1103/PhysRevLett.114.027001` (2 Jan. 2015).

11. Bao, W. *et al.* Tunable $(\delta\pi, \delta\pi)$-Type Antiferromagnetic Order in α-Fe(Te,Se) Superconductors. *Physical Review Letters* **102,** 247001. `https://link.aps.org/doi/10.1103/PhysRevLett.102.247001` (24 June 2009).

12. Chang, C.-C. *et al.* Superconductivity in PbO-type tetragonal FeSe nanoparticles. *Solid State Communications* **152,** 649–652. ISSN: 0038-1098. https://www.sciencedirect.com/science/article/pii/S0038109812000555 (8 2012).

13. Patel, U. *et al.* Growth and superconductivity of FeSex crystals. *Applied Physics Letters* **94,** 082508. ISSN: 0003-6951. https://doi.org/10.1063/1.3093838 (8 Feb. 2009).

14. Liu, T. J. *et al.* Charge-carrier localization induced by excess Fe in the superconductor $Fe_{1+y}Te_{1-x}Se_x$. *Physical Review B* **80,** 174509. https://link.aps.org/doi/10.1103/PhysRevB.80.174509 (17 Nov. 2009).

15. Fang, M. H. *et al.* Superconductivity close to magnetic instability in $\{Fe\}\{(\{\{Se\}\}_\{1\{-\}x\}\{\{Te$ *Physical Review B* **78,** 224503. https://link.aps.org/doi/10.1103/PhysRevB.78.224503 (22 Dec. 2008).

16. Yeh, K.-W. *et al.* Tellurium substitution effect on superconductivity of the α-phase iron selenide. *Europhysics Letters* **84,** 37002. ISSN: 0295-5075. https://dx.doi.org/10.1209/0295-5075/84/37002 (3 2008).

17. Liu, T. J. *et al.* From (π,0) magnetic order to superconductivity with (π,π) magnetic resonance in Fe1.02Te1-xSex. *Nature Materials* **9,** 718–720. ISSN: 1476-4660. https://doi.org/10.1038/nmat2800 (9 2010).

18. Zhuang, J. *et al.* Unabridged phase diagram for single-phased FeSexTe1-x thin films. *Scientific Reports* **4,** 7273. ISSN: 2045-2322. https://doi.org/10.1038/srep07273 (1 2014).

19. Sun, Y. *et al.* Dynamics and mechanism of oxygen annealing in Fe1+yTe0.6Se0.4 single crystal. *Scientific Reports* **4,** 4585. ISSN: 2045-2322. https://doi.org/10.1038/srep04585 (1 2014).

20. Hu, H. *et al.* Structure of the oxygen-annealed chalcogenide superconductor $Fe_{1.08}Te_{0.55}Se_{0.45}O_x$. *Physical Review B* **85,** 64504. https://link.aps.org/doi/10.1103/PhysRevB.85.064504 (6 Feb. 2012).

21. Kawasaki, Y. *et al.* Phase diagram and oxygen annealing effect of FeTe1-xSex iron-based superconductor. *Solid State Communications* **152,** 1135–1138. ISSN: 0038-1098. https://www.sciencedirect.com/science/article/pii/S0038109812001974 (13 2012).

22. Sun, Y., Taen, T., Tsuchiya, Y., Shi, Z. X. & Tamegai, T. Effects of annealing, acid and alcoholic beverages on Fe1+yTe0.6Se0.4. *Superconductor Science and Technology* **26,** 015015. ISSN: 0953-2048. https://dx.doi.org/10.1088/0953-2048/26/1/015015 (1 2013).

23. Medvedev, S. *et al.* Electronic and magnetic phase diagram of β-Fe1.01Se with superconductivity at 36.7 K under pressure. *Nature Materials* **8,** 630–633. ISSN: 1476-4660. https://doi.org/10.1038/nmat2491 (8 2009).

24. Margadonna, S. *et al.* Pressure evolution of the low-temperature crystal structure and bonding of the superconductor FeSe ($\{T\}_{\{}c\} = 37\{\}\{K\}$). *Physical Review B* **80,** 64506. https://link.aps.org/doi/10.1103/PhysRevB.80.064506 (6 Aug. 2009).

25. Wang, Q.-Y. *et al.* Interface-Induced High-Temperature Superconductivity in Single Unit-Cell FeSe Films on SrTiO 3. *Chinese Physics Letters* **29,** 037402. ISSN: 1741-3540. http://dx.doi.org/10.1088/0256-307X/29/3/037402 (Mar. 2012).

26. Peng, R. *et al.* Measurement of an Enhanced Superconducting Phase and a Pronounced Anisotropy of the Energy Gap of a Strained FeSe Single Layer in FeSe/Nb : $SrTiO_3$/$KTaO_3$ Heterostructures Using Photoemission Spectroscopy. *Physical Review Letters* **112,** 107001. https://link.aps.org/doi/10.1103/PhysRevLett.112.107001 (10 Mar. 2014).

27. Peng, R. *et al.* Tuning the band structure and superconductivity in single-layer FeSe by interface engineering. *Nature Communications* **5,** 5044. ISSN: 2041-1723. https://doi.org/10.1038/ncomms6044 (1 2014).

28. Tan, S. *et al.* Interface-induced superconductivity and strain-dependent spin density waves in FeSe/SrTiO3 thin films. *Nature Materials* **12,** 634–640. ISSN: 1476-4660. https://doi.org/10.1038/nmat3654 (7 2013).

29. He, S. *et al.* Phase diagram and electronic indication of high-temperature superconductivity at 65 K in single-layer FeSe films. *Nature Materials* **12,** 605–610. ISSN: 1476-4660. https://doi.org/10.1038/nmat3648 (7 2013).

30. Ge, J.-F. *et al.* Superconductivity above 100 K in single-layer FeSe films on doped SrTiO3. *Nature Materials* **14,** 285–289. ISSN: 1476-4660. https://doi.org/10.1038/nmat4153 (3 2015).

31. Song, Q. *et al.* Evidence of cooperative effect on the enhanced superconducting transition temperature at the FeSe/SrTiO3 interface. *Nature Communications* **10,** 758. ISSN: 2041-1723. https://doi.org/10.1038/s41467-019-08560-z (1 2019).

32. Hoffman, J. E. Sign Flips and Spin Fluctuations in Iron High-Tc Superconductors. *Science* **328.** doi: 10.1126/science.1188927, 441–443. https://doi.org/10.1126/science.1188927 (5977 Apr. 2010).

33. Mazin, I. I., Singh, D. J., Johannes, M. D. & Du, M. H. Unconventional Superconductivity with a Sign Reversal in the Order Parameter of $LaFeAsO_{1-x}F_x$. *Physical Review Letters* **101,** 57003. https://link.aps.org/doi/10.1103/PhysRevLett.101.057003 (5 July 2008).

34. Xia, Y. *et al.* Fermi Surface Topology and Low-Lying Quasiparticle Dynamics of Parent $Fe_{1+x}Te$/Se Superconductor. *Physical Review Letters* **103,** 37002. https://link.aps.org/doi/10.1103/PhysRevLett.103.037002 (3 July 2009).

35. Qiu, Y. *et al.* Spin Gap and Resonance at the Nesting Wave Vector in Superconducting $\{\{FeSe\}\}_{\{}0.4\}\{\{Te\}\}_{\{}0.6\}$. *Physical Review Letters* **103,** 67008. https://link.aps.org/doi/10.1103/PhysRevLett.103.067008 (6 Aug. 2009).

36. Binnig, G. & Rohrer, H. Scanning tunneling microscopy. *Surface Science* **126,** 236–244. ISSN: 0039-6028. https://www.sciencedirect.com/science/article/pii/003960288390716I (1 1983).

37. Hanaguri, T., Niitaka, S., Kuroki, K. & Takagi, H. Unconventional s-Wave Superconductivity in Fe(Se,Te). *Science* **328.** doi: 10.1126/science.1187399, 474–476. https://doi.org/10.1126/science.1187399 (5977 Apr. 2010).

38. Moore, J. E. The birth of topological insulators. *Nature* **464,** 194–198. ISSN: 1476-4687. https://doi.org/10.1038/nature08916 (7286 2010).

39. V. Klitzing, K., Dorda, G. & Pepper, M. New Method for High-Accuracy Determination of the Fine-Structure Constant Based on Quantized Hall Resistance. *Physical Review Letters* **45,** 494–497. https://link.aps.org/doi/10.1103/PhysRevLett.45.494 (6 Aug. 1980).

40. Haldane, F. D. M. Model for a Quantum Hall Effect without Landau Levels: Condensed-Matter Realization of the "Parity Anomaly". *Physical Review Letters* **61,** 2015–2018. https://link.aps.org/doi/10.1103/PhysRevLett.61.2015 (18 Oct. 1988).

41. König, M. *et al.* Quantum Spin Hall Insulator State in HgTe Quantum Wells. *Science* **318.** doi: 10.1126/science.1148047, 766–770. https://doi.org/10.1126/science.1148047 (5851 Nov. 2007).

42. Hsieh, D. *et al.* A topological Dirac insulator in a quantum spin Hall phase. *Nature* **452,** 970–974. ISSN: 1476-4687. https://doi.org/10.1038/nature06843 (7190 2008).

43. Hasan, M. Z. & Kane, C. L. Colloquium: Topological insulators. *Reviews of Modern Physics* **82,** 3045–3067. https://link.aps.org/doi/10.1103/RevModPhys.82.3045 (4 Nov. 2010).

44. Wang, Z. *et al.* Topological nature of the $FeSe_{0.5}Te_{0.5}$ superconductor. *Physical Review B* **92,** 115119. https://link.aps.org/doi/10.1103/PhysRevB.92.115119 (11 Sept. 2015).

45. Wilczek, F. Majorana returns. *Nature Physics* **5,** 614–618. ISSN: 1745-2481. https://doi.org/10.1038/nphys1380 (9 2009).

46. Read, N. & Green, D. Paired states of fermions in two dimensions with breaking of parity and time-reversal symmetries and the fractional quantum Hall effect. *Physical Review B* **61,** 10267–10297. https://link.aps.org/doi/10.1103/PhysRevB.61.10267 (15 Apr. 2000).

47. Fu, L. & Kane, C. L. Superconducting Proximity Effect and Majorana Fermions at the Surface of a Topological Insulator. *Physical Review Letters* **100,** 96407. https://link.aps.org/doi/10.1103/PhysRevLett.100.096407 (9 Mar. 2008).

48. Fu, L. & Kane, C. L. Josephson current and noise at a superconductor/quantum-spin-Hall-insulator/superconductor junction. *Physical Review B* **79,** 161408. https://link.aps.org/doi/10.1103/PhysRevB.79.161408 (16 Apr. 2009).

49. Nayak, C., Simon, S. H., Stern, A., Freedman, M. & Sarma, S. D. Non-Abelian anyons and topological quantum computation. *Reviews of Modern Physics* **80,** 1083–1159. https://link.aps.org/doi/10.1103/RevModPhys.80.1083 (3 Sept. 2008).

50. Zhang, P. *et al.* Observation of topological superconductivity on the surface of an iron-based superconductor. *Science* **360.** doi: 10.1126/science.aan4596, 182–186. https://doi.org/10.1126/science.aan4596 (6385 Apr. 2018).

51. Wang, D. *et al.* Evidence for Majorana bound states in an iron-based superconductor. *Science* **362.** doi: 10.1126/science.aao1797, 333–335. https://doi.org/10.1126/science.aao1797 (6412 Oct. 2018).

52. Caroli, C., Gennes, P. G. D. & Matricon, J. Bound Fermion states on a vortex line in a type II superconductor. *Physics Letters* **9,** 307–309. ISSN: 0031-9163. https://www.sciencedirect.com/science/article/pii/0031916364903750 (4 1964).

53. Kondo, J. Resistance Minimum in Dilute Magnetic Alloys. *Progress of Theoretical Physics* **32,** 37–49. ISSN: 0033-068X. https://doi.org/10.1143/PTP.32.37 (1 July 1964).

54. Chen, M. *et al.* Discrete energy levels of Caroli-de Gennes-Matricon states in quantum limit in FeTe0.55Se0.45. *Nature Communications* **9,** 970. ISSN: 2041-1723. https://doi.org/10.1038/s41467-018-03404-8 (1 2018).

55. Hess, H. F., Robinson, R. B., Dynes, R. C., Valles, J. M. & Waszczak, J. V. Scanning-Tunneling-Microscope Observation of the Abrikosov Flux Lattice and the Density of States near and inside a Fluxoid. *Physical Review Letters* **62,** 214–216. https://link.aps.org/doi/10.1103/PhysRevLett.62.214 (2 Jan. 1989).

56. Shen, L. Y. L. & Rowell, J. M. Zero-Bias Tunneling Anomalies—Temperature, Voltage, and Magnetic Field Dependence. *Physical Review* **165,** 566–577. https://link.aps.org/doi/10.1103/PhysRev.165.566 (2 Jan. 1968).

57. Zhang, R.-X., Cole, W. S. & Sarma, S. D. Helical Hinge Majorana Modes in Iron-Based Superconductors. *Physical Review Letters* **122,** 187001. https://link.aps.org/doi/10.1103/PhysRevLett.122.187001 (18 May 2019).

58. Gray, M. J. *et al.* Evidence for Helical Hinge Zero Modes in an Fe-Based Superconductor. *Nano Letters* **19.** doi: 10.1021/acs.nanolett.9b00844, 4890–4896. ISSN: 1530-6984. https://doi.org/10.1021/acs.nanolett.9b00844 (8 Aug. 2019).

59. Wu, C. H. *et al.* Transport properties in FeSe0.5Te0.5 nanobridges. *Applied Physics Letters* **102,** 222602. ISSN: 0003-6951. https://doi.org/10.1063/1.4809920 (22 June 2013).

60. Ambegaokar, V. & Baratoff, A. Tunneling Between Superconductors. *Physical Review Letters* **10,** 486–489. https://link.aps.org/doi/10.1103/PhysRevLett.10.486 (11 June 1963).

61. Qiu, G. *et al.* Emergent ferromagnetism with superconductivity in Fe(Te,Se) van der Waals Josephson junctions. *Nature Communications* **14,** 6691. ISSN: 2041-1723. https://doi.org/10.1038/s41467-023-42447-4 (1 2023).

62. Josephson, B. D. Possible new effects in superconductive tunnelling. *Physics Letters* **1,** 251–253. ISSN: 0031-9163. `https://www.sciencedirect.com/science/article/pii/0031916362913690` (7 1962).

63. Shapiro, S. Josephson Currents in Superconducting Tunneling: The Effect of Microwaves and Other Observations. *Physical Review Letters* **11,** 80–82. `https://link.aps.org/doi/10.1103/PhysRevLett.11.80` (2 July 1963).

64. Raes, B. *et al.* Fractional Shapiro steps in resistively shunted Josephson junctions as a fingerprint of a skewed current-phase relationship. *Physical Review B* **102,** 54507. `https://link.aps.org/doi/10.1103/PhysRevB.102.054507` (5 Aug. 2020).

65. Domínguez, F. *et al.* Josephson junction dynamics in the presence of $2\{\pi\}$- and $4\{\pi\}$-periodic supercurrents. *Physical Review B* **95,** 195430. `https://link.aps.org/doi/10.1103/PhysRevB.95.195430` (19 May 2017).

66. Picó-Cortés, J., Domínguez, F. & Platero, G. Signatures of a $4\{\pi\}$-periodic supercurrent in the voltage response of capacitively shunted topological Josephson junctions. *Physical Review B* **96,** 125438. `https://link.aps.org/doi/10.1103/PhysRevB.96.125438` (12 Sept. 2017).

67. Dartiailh, M. C. *et al.* Missing Shapiro steps in topologically trivial Josephson junction on InAs quantum well. *Nature Communications* **12,** 78. ISSN: 2041-1723. `https://doi.org/10.1038/s41467-020-20382-y` (1 2021).

68. McCumber, D. E. Effect of ac Impedance on dc Voltage-Current Characteristics of Superconductor Weak-Link Junctions. *Journal of Applied Physics* **39,** 3113–3118. ISSN: 0021-8979. `https://doi.org/10.1063/1.1656743` (7 June 1968).

69. Russer, P. Influence of Microwave Radiation on Current-Voltage Characteristic of Superconducting Weak Links. *Journal of Applied Physics* **43,** 2008–2010. ISSN: 0021-8979. `https://doi.org/10.1063/1.1661440` (4 Apr. 1972).

70. Lim, J. S., Choi, M. Y., Choi, J. & Kim, B. J. Dynamic transition and Shapiro-step melting in a frustrated Josephson-junction array. *Physical Review B* **69,** 220504. `https://link.aps.org/doi/10.1103/PhysRevB.69.220504` (22 June 2004).

71. Tekić, J., He, D. & Hu, B. Noise effects in the ac-driven Frenkel-Kontorova model. *Physical Review E* **79,** 36604. `https://link.aps.org/doi/10.1103/PhysRevE.79.036604` (3 Mar. 2009).

72. Mali, P. *et al.* Complexity of Shapiro steps. *Physical Review E* **101,** 32203. `https://link.aps.org/doi/10.1103/PhysRevE.101.032203` (3 Mar. 2020).

73. Stewart, W. C. Current-Voltage Chariacteristics of Josephson Junctions. *Applied Physics Letters* **12,** 277–280. ISSN: 0003-6951. `https://doi.org/10.1063/1.1651991` (8 Apr. 1968).

74. Chakravarty, S., Ingold, G.-L., Kivelson, S. & Zimanyi, G. Quantum statistical mechanics of an array of resistively shunted Josephson junctions. *Physical Review B* **37,** 3283–3294. `https://link.aps.org/doi/10.1103/PhysRevB.37.3283` (7 Mar. 1988).

75. Huang, Z. *et al.* The study of contact properties in edge-contacted graphene–aluminum Josephson junctions. *Applied Physics Letters* **121,** 243503. ISSN: 0003-6951. `https://doi.org/10.1063/5.0135034` (24 Dec. 2022).

76. Snyder, R. *et al.* Weak-link Josephson Junctions Made from Topological Crystalline Insulators. *Physical Review Letters* **121,** 97701. `https://link.aps.org/doi/10.1103/PhysRevLett.121.097701` (9 Aug. 2018).

77. Court, N. A., Ferguson, A. J. & Clark, R. G. Energy gap measurement of nanostructured aluminium thin films for single Cooper-pair devices. *Superconductor Science and Technology* **21,** 015013. ISSN: 0953-2048. `https://dx.doi.org/10.1088/0953-2048/21/01/015013` (1 2008).

78. Huebener, R. P. & Gallus, D. E. Current-Induced Intermediate State in Thin-Film Type-I Superconductors: Electrical Resistance and Noise. *Physical Review B* **7,** 4089–4099. `https://link.aps.org/doi/10.1103/PhysRevB.7.4089` (9 May 1973).

79. Skocpol, W. J., Beasley, M. R. & Tinkham, M. Phase-slip centers and nonequilibrium processes in superconducting tin microbridges. *Journal of Low Temperature Physics* **16,** 145–167. ISSN: 1573-7357. `https://doi.org/10.1007/BF00655865` (1 1974).

80. Andronov, A., Gordion, I., Kurin, V., Nefedov, I. & Shereshevskii, I. Kinematic vortices and phase slip lines in the dynamics of the resistive state of narrow superconductive thin film channels. *Physica C: Superconductivity* **213,** 193–199 (Aug. 1993).

81. Berdiyorov, G. R., Milošević, M. V. & Peeters, F. M. Kinematic vortex-antivortex lines in strongly driven superconducting stripes. *Physical Review B* **79,** 184506. `https://link.aps.org/doi/10.1103/PhysRevB.79.184506` (18 May 2009).

82. Berdiyorov, G. *et al.* Dynamics of current-driven phase-slip centers in superconducting strips. *Physical Review B* **90,** 54506. `https://link.aps.org/doi/10.1103/PhysRevB.90.054506` (5 Aug. 2014).

83. Stephen, M. J. & Bardeen, J. Viscosity of Type-II Superconductors. *Physical Review Letters* **14,** 112–113. `https://link.aps.org/doi/10.1103/PhysRevLett.14.112` (4 Jan. 1965).

84. Glazman, L. I. Vortex-induced transverse voltage in a film. *Soviet Journal Low Temperature Physics* **12,** 389–392. ISSN: 0360-0335. `https://doi.org/10.1063/10.0031533` (7 July 1986).

85. Sivakov, A. G. *et al.* Josephson Behavior of Phase-Slip Lines in Wide Superconducting Strips. *Physical Review Letters* **91,** 267001. `https://link.aps.org/doi/10.1103/PhysRevLett.91.267001` (26 Dec. 2003).

86. Tran, S., Sell, J. & Williams, J. R. Dynamical Josephson effects in NbSe$_2$. *Physical Review Research* **2,** 43204. `https://link.aps.org/doi/10.1103/PhysRevResearch.2.043204` (4 Nov. 2020).

87. Kadin, A. M., Skocpol, W. J. & Tinkham, M. Magnetic field dependence of relaxation times in nonequilibrium superconductors. *Journal of Low Temperature Physics* **33,** 481–503. ISSN: 1573-7357. `https://doi.org/10.1007/BF00115571` (5 1978).

88. Kuznetsov, V. I. & Trofimov, O. V. Critical temperatures and critical currents of wide and narrow quasi-one-dimensional superconducting aluminum structures in zero magnetic field. *Physica C: Superconductivity and its Applications* **595,** 1354030. ISSN: 0921-4534. https : / / www . sciencedirect . com / science / article / pii / S0921453422000181 (2022).

89. Zhang, C., Si, W. & Li, Q. Doubling the critical current density in superconducting FeSe0.5Te0.5 thin films by low temperature oxygen annealing. *Applied Physics Letters* **109,** 202601. ISSN: 0003-6951. https://doi.org/10.1063/1.4967879 (20 Nov. 2016).

90. Wyatt, A. F. G., Dmitriev, V. M., Moore, W. S. & Sheard, F. W. Microwave-Enhanced Critical Supercurrents in Constricted Tin Films. *Physical Review Letters* **16,** 1166–1169. https://link.aps.org/doi/10.1103/PhysRevLett.16.1166 (25 June 1966).

91. Anderson, P. W. & Dayem, A. H. Radio-Frequency Effects in Superconducting Thin Film Bridges. *Physical Review Letters* **13,** 195–197. https://link.aps.org/doi/10.1103/PhysRevLett.13.195 (6 Aug. 1964).

92. Loidl, M. *et al.* Quasiparticle diffusion over several mm in cryogenic detectors. *Nuclear Instruments and Methods in Physics Research Section A: Accelerators, Spectrometers, Detectors and Associated Equipment* **465,** 440–446. ISSN: 0168-9002. https://www.sciencedirect.com/science/article/pii/S0168900201006210 (2 2001).

93. López-Núñez, D. *et al. Magnetic penetration depth of Aluminum thin films* 2025. arXiv: 2311.14119 [cond-mat.supr-con]. https://arxiv.org/abs/2311.14119.

94. Kim, H. *et al.* London penetration depth and superfluid density of single-crystalline $Fe_{1+y}(Te_{1-x}Se_x)$ and $Fe_{1+y}(Te_{1-x}S_x)$. *Physical Review B* **81,** 180503. https://link.aps.org/doi/10.1103/PhysRevB.81.180503 (18 May 2010).

95. Si, W. *et al.* Grain boundary junctions of FeSe0.5Te0.5 thin films on SrTiO3 bicrystal substrates. *Applied Physics Letters* **106,** 032602. ISSN: 0003-6951. https://doi.org/10.1063/1.4906429 (3 Jan. 2015).

96. Ryazanov, V. V. *et al.* Coupling of Two Superconductors through a Ferromagnet: Evidence for a $\{\pi\}$ Junction. *Physical Review Letters* **86,** 2427–2430. https://link.aps.org/doi/10.1103/PhysRevLett.86.2427 (11 Mar. 2001).

97. Wollman, D. A., Harlingen, D. J. V., Giapintzakis, J. & Ginsberg, D. M. Evidence for $d_{x^2-y^2}$ Pairing from the Magnetic Field Modulation of $YBa_2Cu_3O_7$-Pb Josephson Junctions. *Physical Review Letters* **74.** YBCO edge contact pi junction, same figure from tinkham, 797–800. https://link.aps.org/doi/10.1103/PhysRevLett.74.797 (5 Jan. 1995).

98. Lin, Y. *et al.* Direct Observation of Quantum Anomalous Vortex in Fe(Se,Te). *Physical Review X* **13,** 11046. https://link.aps.org/doi/10.1103/PhysRevX.13.011046 (1 Mar. 2023).

99. Rashidi, A., Huynh, W., Guo, B., Ahadi, S. & Stemmer, S. Vortex-induced anomalies in the superconducting quantum interference patterns of topological insulator Josephson junctions. *npj Quantum Materials* **9,** 70. ISSN: 2397-4648. `https://doi.org/10.1038/s41535-024-00684-w` (1 2024).

100. Simpson, R. *Introductory Electronics for Scientists and Engineers* ISBN: 9780205038459. `https://books.google.com/books?id=qARTAAAAMAAJ` (Allyn and Bacon, 1974).

101. Systems, S. R. *SR860 500 kHz DSP Lock-in Amplifier* 2.11. Stanford Research Systems (1290-C Reamwood Avenue, Sunnyvale, California 94089, 2025). `https://www.thinksrs.com/downloads/pdfs/manuals/SR860m.pdf`.